

LITHIUM RECOVERY FROM DILUTED BRINES
BY MEANS OF A FLOW-THROUGH ELECTRODES
ELECTROCHEMICAL REACTOR

Vom Fachbereich Produktionstechnik

der

UNIVERSITÄT BREMEN

zur Erlangung des Grades
Doktor-Ingenieur
genehmigte

Dissertation

von

M. Sc. Maria Sofia Palagonia

Gutachter:
Prof. Fabio La Mantia
Prof. Simonetta Palmas (University of Cagliari)

Tag der mündlichen Prüfung: 28.06.2019

The more I see, the less I know for sure

John Lennon

*True happiness is to enjoy the present,
without anxious dependence upon the future,
not to amuse ourselves with either hopes or fears
but to rest satisfied with what we have,
which is sufficient, for he that is so wants nothing.*

*The greatest blessings of mankind are within us
and within our reach. A wise man is content with his lot,
whatever it may be, without wishing for what he has not.*

Lucius Annaeus Seneca

Acknowledgement

This PhD work would not have been possible without the support of many people, who contributed in different ways.

I am grateful to my supervisor Prof. Fabio La Mantia for giving me the opportunity to work in his research group and for the fruitful scientific discussions we had over the years; I also thank him for having exhorted me to give my best at work and to learn from my mistakes. I thank my colleague and friend Dorian Brogioli for his constant scientific support, the countless suggestions and the ideas developed together. Thank you also for your kindness and for the “good coffee” you offered me every day! Without Fabio and Dorian the development of this project would have not been possible.

I thank my colleagues Collins Erinwingbovo, Ghoncheh Kasiri, Dominique Koster, Amir Bani Hashemi, Kurt Neumeister and Miriam Gutjahr for their valuable support over the years. I thank Jenz Glenneberg for having performed the SEM images of my electrodes.

I am thankful to Prof. Francesco Di Quarto and Prof. Monica Santamaria for their support and encouragement when I decided to start the PhD and during the last three years. Thank you for being the first people to transmit me the love for research.

I thank Giorgia Zampardi for her company in the short but pleasant time she spent in the office, and for her precious advices and corrections of my English grammar!

I would like also to thank the people who have filled my life outside the working hours and have contributed to make special this experience in Bremen.

I am thankful to Mariela Tapia, because she remembered me what having a true friend means, for having listened to me and advised me, and (especially!) for having explored with me the cool and alternative part of Bremen. Thank you my friend!

I thank Chris Galanopoulos, Leonardo Maia and Anthon Ochoa Bique, for their friendship and their support. I will miss our lunches together, our nonsense conversations and laughs.

I thank Martina Eiden for her sincere friendship, for our dancing evenings and for bearing with my terrible German.

I am thankful to my friend Maria Isabel Velez for her sweetness and affection.

Un ringraziamento speciale va a Irene Facchinetti, che ha portato una ventata di simpatia, allegria e vitalità nell'ufficio e nel laboratorio, che mi ha fatto ricordare le proprietà benefiche delle uscite spontanee post-lavoro in buona compagnia e che ha cercato di coinvolgermi senza successo nelle meraviglie della musica latina. Grazie amica mia!

Grazie alle mie fantastiche amiche Giulia Leone, Camilla Mosele e Silvia Malagoli, che mi hanno fatto sentire a casa, seppur a tanti chilometri di distanza. La vostra amicizia significa tanto per me e la mia esperienza a Brema non sarebbe stata la stessa senza di voi.

Grazie a Francesco Di Franco e Andrea Zaffora per essere stati i primi colleghi di laboratorio (gli originali e insostituibili!) e per il loro costante affetto.

Grazie alla mia migliore amica Lisa Avarello per la sua costante presenza nella mia vita nonostante la lontananza fisica e per essere per me fonte di esempio e di ispirazione. Non ci sono parole che possano esprimere cosa la nostra amicizia significhi per me.

Ringrazio i miei genitori, Gaetana Cuccia e Aldo Palagonia, per essere stati ogni giorno presenti durante questi tre anni. Nonostante la distanza, non mi hanno mai fatto mancare il loro appoggio e il loro amore, che mi dimostrano di continuo in tutti i modi possibili. Grazie per le chiamate Skype ("Mi senti? Io ti sento! Ti sei bloccata! No, ora ti sei sbloccata!"), per i loro frequenti viaggi nella Germania del nord e per avermi insegnato a credere in me stessa.

Grazie a mia sorella Chiara Palagonia per le nostre lunghe telefonate a parlare di tutto o di niente, per il suo supporto e la sua pazienza durante i mesi di scrittura in cui le illustravo nel dettaglio le mie difficoltà, per la sua saggezza e i suoi consigli. Ti voglio bene amore mio!

Ma il ringraziamento più grande va senza dubbio al mio compagno di vita Calogero Giglia. Grazie per essermi stato accanto ogni giorno incondizionatamente, in ogni momento negli ultimi tre anni; per avermi incoraggiato, consigliato, supportato (e sopportato!), per il tuo modo di rendermi tutto più facile e leggero. Non sono sicura che avrei potuto portare a termine questo lavoro senza di te! É a te che dedico questa tesi.

Abstract

Lithium has become an important raw material in various sectors because of the continuously growing market of its derivative products, in particular of rechargeable batteries. Its demand is expected to grow hugely in the near future, due to the development and spread of hybrid and fully electric vehicles and of lithium-ion batteries for stationary energy storage [1, 2]. Currently, lithium is mainly extracted from brine by means of the lime-soda evaporation process, consisting in a solar evaporation to increase its initial concentration and other following chemical treatments to remove unwanted cations. This process has several disadvantages, such as the unreliability due to the weather conditions, the water consumption, the slowness, and the large amount of chemical wastage. Therefore, a more efficient, faster and environmental friendly lithium recovery technology is urgently needed.

In the last decade, many efforts have been done in order to find better alternatives for the extraction of lithium from brine. In particular, La Mantia et al. [3, 4, 5, 6, 7, 8, 9] have firstly introduced a new technique, known as electrochemical ion pumping. The electrochemical ion pumping technique consists in applying a current to extract lithium cations from brine, driving them in a lithium-selective electrode by means of the intercalation mechanism. The cations are then released in a recovery solution applying the current in the opposite direction. The lighter environmental impact and the higher speed of this technique compared to the lime-soda evaporation process make the electrochemical ion pumping a good alternative for the lithium production.

The other problem related to the production of lithium regards its global sources. The brine sources with a relative high lithium concentration to be exploited through the evaporation-based process are located mostly in South America. Together with the increase in the demand, the economic monopoly of lithium production is the reason of lithium increasing price. On this grounds, the diversification of the lithium supply will play an important role in the spread and competitiveness of lithium based technologies. The possibility to exploit other more diluted lithium sources (10-50 mg/l of lithium concentration), such as geothermal waters, brines produced in salt-works, waste waters from gas and oil extraction wells, is of worldwide interest.

The aim of this PhD thesis has been to design and test a suitable electrochemical reactor for the extraction of lithium through electrochemical ion pumping from diluted brines, down to a lithium concentration of 7 mg/l (1 mM). The extraction from low concentrated solution is challenging due to the mass transport limitations in the liquid phase that reduce the process efficiency. Therefore a flow-through electrodes reactor has been designed, in order to improve the mass transport by adding a convective flux of the electrolyte.

Firstly, a preliminary study of the thermodynamic behavior of the materials used in the reactor was carried out. Then the capturing process has been implemented and investigated at various conditions. The capture efficiency was tested at various lithium concentrations and flow rates, finding that the amount of captured lithium increases with the flow rate up to a maximum value that decreases with the concentrations. The efficiency at low concentrations has been optimized by improving the active material distribution on the electrode. Further investigations on the capturing process have been carried out at various currents. The results show that, by decreasing the current, the amount of captured lithium increases, while the flow rate to be applied reduces, thus sparing hydraulic energy.

A mathematical model has been developed to explain and support the experimental results. The model is based on a simplified description of the electrode porous distribution and it reproduces the experimental behavior at various flow rates, concentrations, porous distributions and currents. The results show that the model can be used to investigate the optimal process parameters and to size the cell components.

Finally the total process (capturing and release) has been performed. More than one litre of brine at 1 mM LiCl was treated, extracting lithium with a capturing yield of 60%. The lithium cations were released back in 5 ml of solution reaching a concentration of 100 mM (700 mg/l) and a purity of 94%, with a release efficiency of 75%.

The high achieved concentration and purity of the final solution demonstrate that the developed reactor can extract efficiently lithium from diluted brine and it represents a valid response to the envisaged lithium market demand.

Kurzfassung

Lithium ist aufgrund des kontinuierlich wachsenden Marktes für seine Derivatprodukte, insbesondere für wiederaufladbare Batterien, zu einem wichtigen Rohstoff in verschiedenen Bereichen geworden. Aufgrund der Entwicklung und Verbreitung von Hybrid- und Vollelektrofahrzeugen sowie von Lithium-Ionen-Batterien zur stationären Energiespeicherung, dürfte die Nachfrage in naher Zukunft massiv steigen [1, 2].

Derzeit wird Lithium hauptsächlich aus Sole durch das Kalksoda-Verdampfungsverfahren gewonnen, das aus einer solaren Verdampfung zur Erhöhung der Anfangskonzentration und weiteren chemischen Behandlungen zur Entfernung unerwünschter Kationen besteht. Dieses Verfahren hat mehrere Nachteile, wie die Unzuverlässigkeit aufgrund der Wetterbedingungen, den Wasserverbrauch, die Langsamkeit und die große Menge an Chemikalienverschwendung. Daher ist eine effizientere, schnellere und umweltfreundlichere Lithium-Rückgewinnungstechnologie dringend erforderlich.

In den letzten zehn Jahren wurden viele Anstrengungen unternommen, um bessere Alternativen für die Gewinnung von Lithium aus Sole zu finden. Insbesondere La Mantia et al. [3, 4, 5, 6, 7, 8, 9] haben zunächst eine neue Technik eingeführt, das so genannte elektrochemische Ionenpumpen. Die elektrochemische Ionenpumpentechnik besteht darin, einen Strom anzulegen, um Lithiumkationen aus der Sole zu extrahieren und sie mittels des Interkalationsmechanismus in einer lithiumselektiven Elektrode anzureichern. Die Kationen werden dann in einer Rückgewinnungslösung freigesetzt, wobei der Strom in die entgegengesetzte Richtung geleitet wird. Die geringere Umweltbelastung und die höhere Geschwindigkeit dieser Technik im Vergleich zum Kalksoda-Verdampfungsprozess machen das elektrochemische Ionenpumpen zu einer guten Alternative für die Lithiumherstellung.

Das andere Problem im Zusammenhang mit der Produktion von Lithium betrifft die globalen Quellen. Die Solequellen mit einer relativ hohen Lithiumkonzentration, die durch den verdampfungsbasierten Prozess genutzt werden sollen, befinden sich überwiegend in Südamerika. Das wirtschaftliche Monopol der Lithiumproduktion ist neben der steigenden Nachfrage der Grund für die Verteuerung von Lithium. Aus diesem Grund wird die Diversifizierung der Lithiumversorgung eine wichtige Rolle bei der Verbreitung und Wettbewerbsfähigkeit von lithiumbasierten Technologien spielen.

Die Möglichkeit andere verdünnte Lithiumquellen (10-50 mg/l Lithiumkonzentration) zu nutzen, wie geothermisches Wasser, in Salinen produzierte Sole, Abwässer aus Gas- und Ölgewinnungsbohrungen, ist weltweit von Interesse.

Ziel dieser Dissertation war es, einen geeigneten elektrochemischen Reaktor für die Extraktion von Lithium durch elektrochemisches Ionenpumpen aus verdünnten Solen bis zu einer Lithiumkonzentration von 7 mg/l (1 mM) zu entwickeln und zu testen.

Eine Herausforderung ist die Extraktion aus niedrig konzentrierter Lösung, da die Beschränkung des Massentransports in der Flüssigphase die Prozesseffizienz reduziert. Daher wurde ein Durchfluss-Elektrodenreaktor entworfen, um den Massentransport durch Zugabe eines konvektiven Stroms des Elektrolyten zu verbessern.

Zunächst wurde eine Vorstudie über das thermodynamische Verhalten der im Reaktor verwendeten Materialien durchgeführt.

Dann wurde der Einlagerungsprozess implementiert und unter verschiedenen Bedingungen untersucht. Die Einlagerungseffizienz wurde bei verschiedenen Lithiumkonzentrationen und -durchflussraten getestet und ergab, dass die Menge des eingeladerten Lithiums mit der Durchflussmenge bis zu einem Maximalwert zunimmt, der mit den Konzentrationen abnimmt. Der Wirkungsgrad bei niedrigen Konzentrationen wurde durch die Verbesserung der Verteilung des aktiven Materials auf der Elektrode optimiert.

Weitere Untersuchungen zum Einlagerungsprozess wurden bei verschiedenen Strömungen durchgeführt. Die Ergebnisse zeigen, dass durch die Verringerung des Stroms die Menge des eingeladerten Lithiums zunimmt, während die anzuwendende Durchflussmenge abnimmt und somit die hydraulische Energie gespart wird.

Zur Erklärung und Unterstützung der experimentellen Ergebnisse wurde ein mathematisches Modell entwickelt. Das Modell basiert auf einer vereinfachten Beschreibung der porösen Elektrodenverteilung und reproduziert das experimentelle Verhalten bei verschiedenen Durchflussraten, Konzentrationen, porösen Verteilungen und Strömungen. Die Ergebnisse zeigen, dass das Modell verwendet werden kann, um die optimalen Prozessparameter zu untersuchen und die Zellkomponenten zu dimensionieren.

Schließlich wurde der gesamte Prozess (Einlagerung und Auslagerung) durchgeführt. Mehr als ein Liter Sole bei 1 mM LiCl wurde behandelt und Lithium mit einer einlagerungsrate von 60% extrahiert. Die Lithium-Kationen wurden in 5 ml Lösung zurückgesetzt und erreichten eine Konzentration von 100 mM (700 mg/l) und eine Reinheit von 94% bei einer Freisetzungseffizienz von 75%.

Die hohe erreichte Konzentration und Reinheit der Endlösung zeigt, dass der entwickelte Reaktor Lithium effizient aus verdünnter Sole extrahieren kann und stellt eine gültige Antwort auf die geplante Nachfrage des Lithiummarktes dar.

Contents

1	Introduction	1
1.1	Current lithium sources and extraction	1
1.2	State of the art: technologies for lithium extraction	3
1.3	The electrochemical ion pumping techniques	5
1.4	The diversification of the lithium sources	12
1.5	Aim of the work	13
2	Theoretical Background	14
2.1	Electrochemical principles	15
2.2	Intercalation processes in a battery-like material	20
2.3	Electrochemical measurements	24
2.4	Type of electrochemical reactors	26
3	Experimental Section	31
3.1	Preparation of the electrodes	31
3.2	Design of the cell	32
3.2.1	Cell geometry to investigate the capturing step	33
3.2.2	Final reactor design	35
3.2.3	Other electrochemical cells	37
3.3	ICP-OES	37
4	Thermodynamics of Materials	38
4.1	Lithium capturing electrode - Lithium Manganese Oxide	38
4.1.1	Thermodynamic model	40
4.2	Lithium excluding electrode - Nickel Hexacyanoferrate	42
4.2.1	Intercalation in single-salt solutions	43
4.2.2	Thermodynamic model in single salt solution	46
4.2.3	Intercalation in mixed solutions	49
4.2.4	Model in a mixture of two cations	49

4.2.5	Conclusions	55
5	Capturing from Diluted Lithium Brine	57
5.1	Effect of the lithium ions concentration	57
5.2	Mathematical model of the reactor	65
5.2.1	Introduction	65
5.2.2	Hydrodynamic model	68
5.2.3	Mass and charge conservation equations	69
5.2.4	The sub-domains and the boundary conditions	72
5.2.5	Simulations	75
5.2.6	Simulations parameters	76
5.2.7	Analysis of the results	79
5.2.8	Effect of porous structure parameters	89
5.2.9	Conclusion	93
5.3	Effect of mass loading	95
5.4	Effect of current	100
5.5	Model results at various currents	104
5.5.1	Integration of the feeding tank in the model	104
5.5.2	Anaysis of results	105
5.6	Pumping energy	109
5.7	Effect of sodium concentration	113
5.8	Ohmic drops	115
6	The Complete Process	117
6.1	Analysis of the results	118
6.2	Electrical power estimation	124
6.3	Final pumping energy	127
7	Conclusions and Outlook	130
	Bibliography	132
	List of Abbreviations	141
	List of Symbols	142

Chapter 1

Introduction

1.1 Current lithium sources and extraction

As raw material, lithium has always been used for several applications in various production sectors, such as the ones of ceramics, glass materials, greases, aluminium and others. In the last twenty years, the global interest on lithium has raised for its use in green energy applications. Thanks to their high energy density and high voltage, lithium-ion batteries are indeed the most promising technology to substitute, at least partially, fossil fuels for powering the vehicles and to reduce the CO₂ global emissions.

Fig. 1.1 shows the market forecast of lithium demand for various applications. According to predictions, lithium demand will largely increase in future, up to 534 Ktons per year in 2025, which is almost twice the value in the current year. While demand of lithium from the Li-ion batteries traditional market (mainly for powering portable electronic devices) and for non-battery applications will remain approximately constant, the major contribution to the future increase of the lithium request is given by the electrical and hybrid vehicles industry. Indeed, lithium-ion batteries are one of the most suitable technology for powering electric transports, together with fuel cells [1]. Lithium-ion batteries may be also used on bigger scale to accumulate energy produced by renewable sources [2]. Growth of energy storage market will also partially contribute to the increase of lithium demand.

If the lithium demand trend will keep to increase and the production of lithium will not match the market demand, its price will continue to raise, making the lithium technologies less economically competitive. Right now, lithium is moderately cheap (16000\$ per ton of battery grade Li₂CO₃), even if its price has been already doubled in the last two years [11], and it will continue to increase in the next years, along with its demand [12].

Global sources of lithium are mainly divided into ores and brine. Vikström et al. [13]

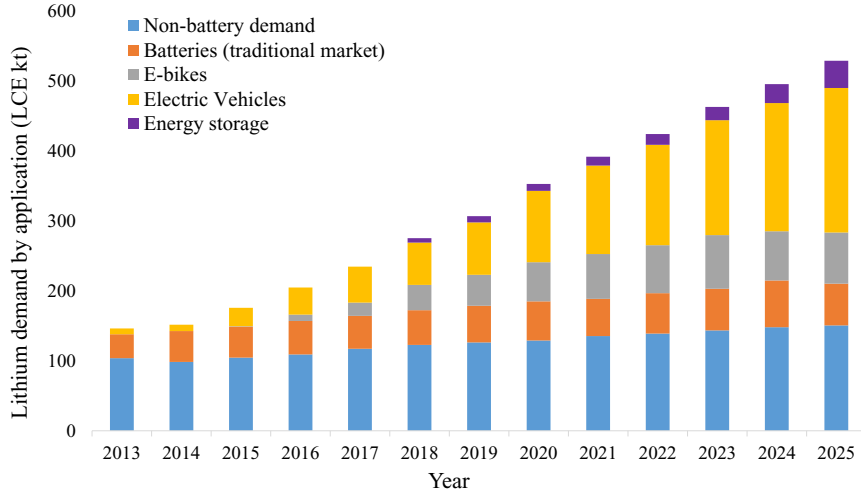


Figure 1.1: Forecast of market demand of lithium carbonate until to 2025, differentiated for each industrial use. The major contribution to its increase is given by the electromobility and energy storage. Adapted from [10].

in 2013 estimated lithium resources amounts from hard rocks and for brines, finding that the brine sources are approximately double of the estimated amount of minerals [13]. Moreover, considering only the amount of lithium needed for powering electric vehicles, it is forecast that in the next two decades the lithium demand will exceed twice to six times the capability of its mineral sources [14].

As reported by Flexer et al. [15], the extraction of lithium from hard rocks requires various hydrometallurgical steps: the ore crushing and heating, the cooling and milling into a fine powder, the mixing with sulphuric acid, and the roasting. Moreover, the powder has to be filtered in order to separate it from the waste, and magnesium and calcium are removed through precipitation. Finally, lithium carbonate is crystallized by adding soda ash, and it is then filtered and dried. Of course, the steps of this process may change depending on the given mineral and its composition. Such hydrometallurgical process is very used in the areas where mineral deposits are present (for example China and Australia that are currently lithium self-producers [16]), although its costs are twice than the ones of lithium extraction from brine.

The easiest and most economically competitive production is the extraction from brines. The term “brine” refers to a saline solution, where the salinity is much higher than sea water (170-330 g/L).

Lithium brines are mostly concentrated in a small region of South America, called “Lithium Triangle” which crosses the borders of Chile, Bolivia and Argentina [16], and it is estimated to have 80% of the world lithium brine resources [15]. There, lithium has a

concentration of circa 300 mg/l and other present cations are Na^+ (in highest amount), K^+ , Mg^{2+} and Ca^{2+} . The anion mostly present is Cl^- , with lower amounts of CO_3^{-2} , SO_4^{-2} and borates [15].

The relatively high concentration of lithium allows its extraction through an evaporation-based technology, called lime-soda evaporation process. This method consists of pumping brine from beneath the crust of the salt lake into a series of large open air shallow evaporation ponds. In this way, the brine concentration goes from 300 ppm to 5000 ppm, and some of the more abundant undesired cations precipitate at the same time. Chemical species that do not precipitate spontaneously must be removed with post chemical treatments, depending on the type and amount of the species. Most of the cations that remain after the evaporation step are magnesium and borates. Magnesium cations are removed through a precipitation step with lime, the borates are instead eliminated through a solvent extraction step. Finally, the Li_2CO_3 is precipitated by adding sodium carbonate [15, 17].

Although having low costs and high margin profits, the lime-soda evaporation process has many disadvantages. First of all, since it is based on solar evaporation, the process is very slow. The period of time between the pumping of brine and the lithium carbonate precipitation is about 1-2 years. Currently, the lithium global production capacity from brine is 120.5 Ktons/year [15], which, according to the predictions, will not be enough to cover the lithium market demand in the near future (see Fig. 1.1).

Secondly, its efficiency depends on highly unreliable factors, like weather conditions, such as rainfall and wind [18]. Furthermore, it delivers large waste products, due to the chemical treatments that follow the evaporation, and it is highly water consuming. Half a million litres of brine have to be evaporated per ton of Li_2CO_3 produced [15]. This problem is accentuated by the fact that these lakes are located in an area already affected by drought. To sum up, the attempt to move towards the use of green energies through lithium-ion batteries, thus decreasing the overall CO_2 emissions, risks to be hindered by a lithium production method that causes a severe environmental impact.

1.2 State of the art: technologies for lithium extraction

Many efforts have been made by researchers in order to find more sustainable ways to extract lithium. The precipitation of lithium from brines as aluminate has been one of the first investigated techniques [19, 20, 21]. The precipitation is achieved through addition of aluminium salts, after a pH adjustment of the brine. Although this process allows to recover 80% of lithium in solution, the final purity strongly depends on the Mg/Li ratio in

solution, and on the presence of other cationic species, since aluminium compounds show a not negligible affinity to other alkaline cations [?]. Moreover, after the precipitation step, lithium has to be separated from aluminum through liquid-liquid extraction [20], or dissolution in sulphuric acid [19]. Hence, the overall process requires large amount of chemicals: acid or bases to adjust the pH prior to precipitation, and large amount of sulphuric acid to further separate lithium from aluminum through dissolution.

Another studied technique to recover lithium from brine is adsorption. Among the most promising materials that can selectively adsorb lithium there are MnO_2 [22, 23], $\text{Li}_1 \cdot 6 \text{Mn}_1 \cdot 6 \text{O}_4$ [24], H_2TiO_3 [25, 26] and $\text{H}_{1.6}\text{Mn}_{1.6}\text{O}_4$ [27], which have a good rate of adsorption of lithium (circa 35 mg/g). Among these materials, the best are the manganese oxides-based ones due to their high selectivity and high capacity. Since they work as ion exchangers, the process needs a strong acidic solution, like HCl, as eluent to regenerate the material. The regeneration step involves the replacement of Li^+ ions by H^+ ions. Also in this case, high volumes of acids are needed to finally recover lithium cations.

Traditional liquid-liquid extraction of lithium from brines has been reported [28, 29, 30], with various organic solvents such as diethyl ether or alcohols. This technique is based on the higher solubility of the LiCl in organic matrix than NaCl and KCl, that allows the selective extraction of Li ions through absorption in organic solvents. The main problem of this technique is the low selectivity in presence of MgCl_2 , due to its similar solubility to LiCl in organic liquid. One way to increase the selectivity of the process is to modify the pH of brines or to add a coextracting agent to the organic solvent, even if the latter often leads to formation of unwanted third phases [28]. Moreover, doubts have been raised on the scalability of the process, due to the challenging selection of the equipment materials, which is subjected to a severe corrosion [15].

A new technology investigated in the recent years is the lithium extraction through membranes. Since the most problematic cation for the lithium separation is magnesium, which is normally present in high amount in lithium brines, various works have focused on the separation of lithium from magnesium through nanofiltration [31, 32]. Nanofiltration membranes have pore size of 1-10 nm and allow the passage of monovalent hydrated cations, blocking the hydrated divalent cations. The separation efficiency depends strongly on Mg/Li ratio and it works for values <20 . The membrane process needs to be further integrated with other technologies to separate other monovalent cations and normally it has high operational costs due to the fouling [31].

Selective membranes have been used also in electrochemical applications. As an example, the electrodialysis consists on applying an electric field in order to separate or to concentrate a salt, and exploiting the inverse flux of opposite charged ions using membranes that allow the selective passage of cations or anions only. Using a membrane selective to monovalent cations, a separation between Mg and Li ions can be obtained

through high applied voltage [33].

The presence of other cationic species than lithium has been always the main obstacle to the development of an alternative strategy for the lithium extraction from brines. The use of additional chemicals is almost always necessary, as well as various unitary operations to get the desired separation.

The challenge is to find an environmental friendly extraction technology that allows to selectively capture lithium, possibly in a one unitary operation. One step further in this direction has been achieved by Kanoh et al. in the 90s, who were the first to use a battery material to electrochemically capture lithium among other cations [34, 35]. They used spinel λ - MnO_2 , since it shows a high electrochemical selectivity towards lithium. Together with LiCoO_2 and LiFePO_4 , λ - MnO_2 is one of the most used materials in lithium-ion batteries. The Li^+ capturing is achieved through intercalation, the process on which the rechargeable batteries are based. The cell proposed by Kanoh et al. [34] works with λ - MnO_2 as a working electrode, that intercalates lithium from solution during its reduction, and a Pt-wire as a counter electrode. In this case, the counter reaction is oxygen generation, which leads to a variation of pH during the process and it has a slow kinetic. The idea to exploit the mechanism of intercalation found its final development in the 2010s with the invention of electrochemical ion pumping techniques.

1.3 The electrochemical ion pumping techniques

In 2012 Pasta et al. presented for the first time a battery-like technology for the extraction of lithium from brine, that belongs to the “electrochemical ion pumping techniques” group. This technique took inspiration from the work of Kanoh et al. [34], but in a revised way. Indeed, it is based on the previously developed “mixing entropy battery” [36] and “desalination battery” [4].

The mixing entropy battery is an electrochemical device, whose aim is to generate energy by exploiting two solutions at different concentrations. If a transfer of ions from a high concentrated solution to a low concentrated solution takes place, a loss of mixing free energy occurs, which can be converted in electric work, if performed close to the reversibility [37]. Briefly, the mixing entropy battery is based on a four-stage process, as shown in Fig. 1.2.

In the first step, an anion-capturing electrode and a cation-capturing electrode are in contact with a concentrated solution, for example sea water. Applying a current in the circuit in one direction, the ions that are in the solution are driven inside the electrodes. In the second step, the circuit is open and a diluted solution (for example river water) is flushed inside the reactor. During the third step, a current with opposite direction is applied and the ions are released in the diluted solution. In the fourth step, the

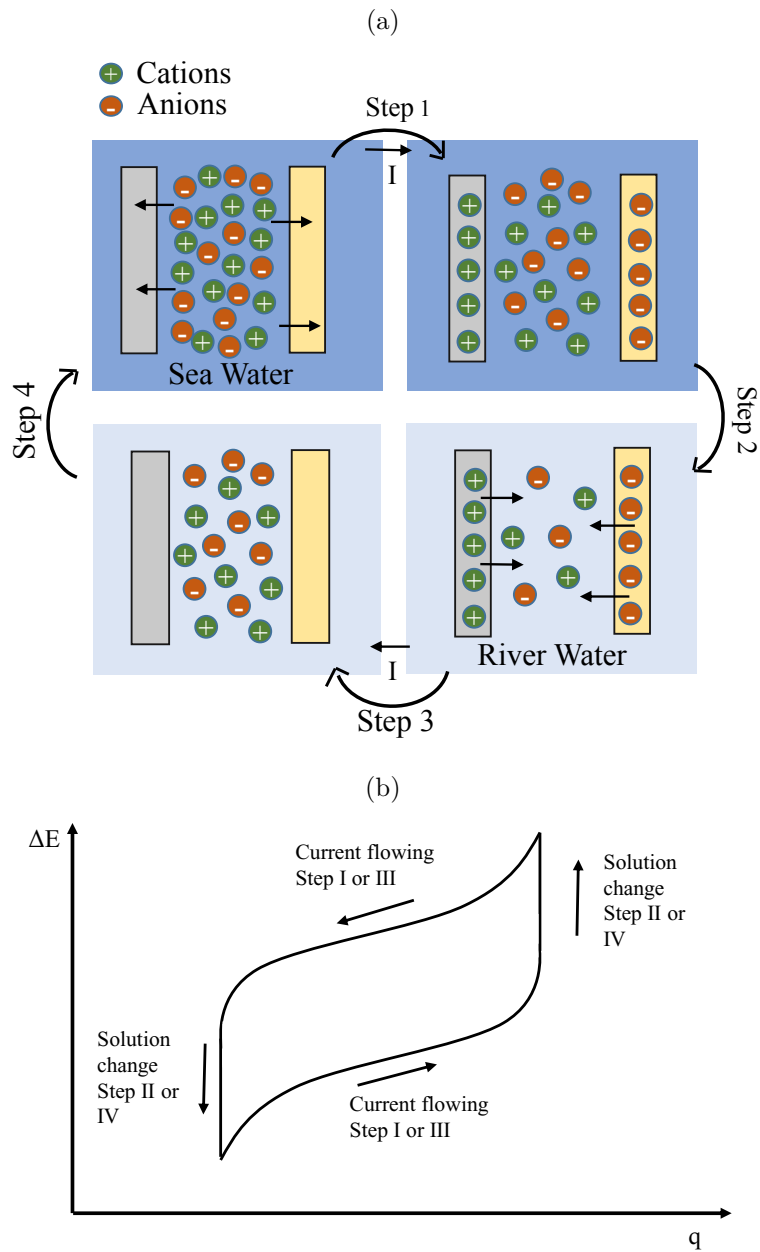


Figure 1.2: Scheme of the four stages of the mixing entropy battery (a). Typical cell voltage difference vs. charge (b). The integral between the charge and discharge curves is the extractable energy. Adapted from [36].

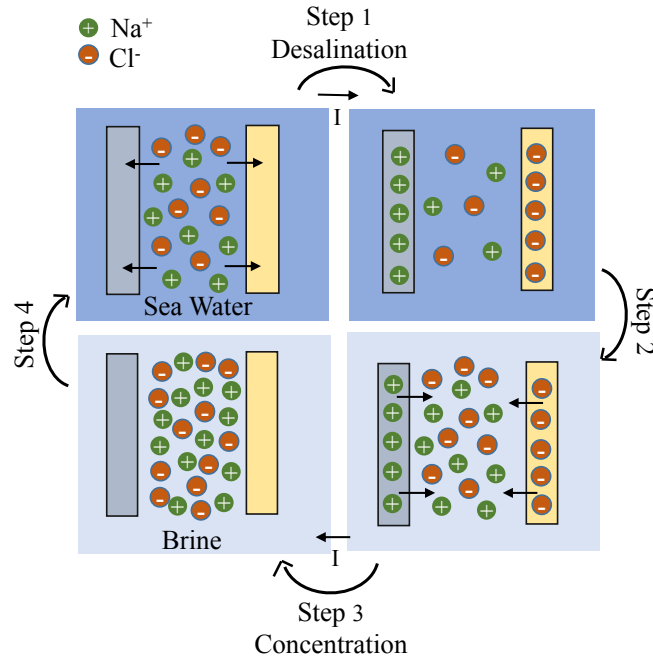


Figure 1.3: Scheme of the four stages of the desalination battery. Adapted from [4].

concentrated solution can be flushed again in the cell, and the cycle can start from the beginning.

During the application of current, the system acts as a battery, namely it produces energy, or as an electrolyzer, requiring energy. The spontaneous direction of the reaction depends on the nature of the electrodes that are used or, in other words, on the Gibbs free energy of the total reaction.

After a complete cycle, the system has produced energy because the step where the device acts as a battery (known as discharge, that may be the second or the fourth step) occurs at higher potential with respect to the other (charge). This difference of potential depends on the difference of concentration between the two solutions.

The cycle in voltage vs. charge plot (Fig. 1.2, (b)) must be counter-clockwise, so that the discharge step of the cell occurs always at higher potential with respect to the charge step [37]. The area included between the two curves is the total extractable energy of the process, which depends on the difference of free energy of the solutions between the starting and the ending point of the cycle and on the electrochemical losses related to the process.

Based on the “mixing entropy battery” concept, the “desalination battery” was developed. This is a technology aimed to desalinate water, transferring ions from a lower

concentrated solution (sea water) to a higher concentrated solution (brine). The term “battery” is indeed a misused name, because the system requires energy to run. The scheme of the process is reported in Fig. 1.3: in the first step cations and anions are captured from sea water and inserted into two different electrodes. During the second step another solution is flushed into the cell, and in the third step the release of ions takes place. At the end of the cycle, deionized water and brine are obtained. The cycle cell voltage vs. charge is the same as the one in Fig. 1.2, (b), but it occurs clock-wise, namely the charge takes place at higher potential than the discharge. The ions mostly present in sea water are sodium and chloride cations, therefore the electrodes are a sodium capturing electrode ($\text{Na}_2\text{Mn}_5\text{O}_{10}$) and silver, which reacts with Cl^- ions forming AgCl [4].

Based on this technique, Pasta et al. proposed a “desalination battery” to selectively extract lithium [3], transferring it from a lithium diluted brine to a concentrated one. Lithium iron phosphate, (LiFePO_4) an active material typically used in lithium-ion batteries, is employed as a lithium capturing electrode and Ag/AgCl as a chlorine capturing electrode. The reaction occurring in the system is the following:



The four stages of the process are the same as the ones described above, with the difference that this time the aim is to obtain a lithium concentrated solution. The scheme is represented in Fig. 1.4.

In the first step, iron in the FePO_4 is reduced from Fe(III) to Fe(II), and lithium cations are intercalated within the material lattice forming an olivine structure with the phosphate and the iron LiFePO_4 (LFP), while the silver is oxidized forming AgCl . In the second step a recovery solution initially free of lithium is flushed into the cell. In the third step LFP is oxidized releasing lithium in solution and AgCl is reduced back to Ag releasing chloride ions. In the fourth step lithium brine is flushed again in the cell and the cycle can start over.

This method leads to very high purity of lithium with respect to other cations (99.88%), starting from a solution containing K^+ , Mg^{2+} and Na^+ [5]. It is much more efficient in term of required energy than the LMO/Pt system presented previously by Kanoh [34, 35], in which during the lithium insertion, oxygen evolution takes place at the Pt electrode, leading to high energy consumption.

However, the use of Ag as an ion-capturing electrode is costly, and the formation of AgCl during the first step is the highest energy-consuming step of the process [4].

Therefore, various studies have been focused on finding an alternative to Ag . Missoni et al. [9] have substituted Ag with polypyrrole, a polymer that shows an anion-exchange behavior, if properly doped. They investigated its stability in aqueous solution and the energy efficiency of the system, revealing that polypyrrole is a good alternative to Ag for

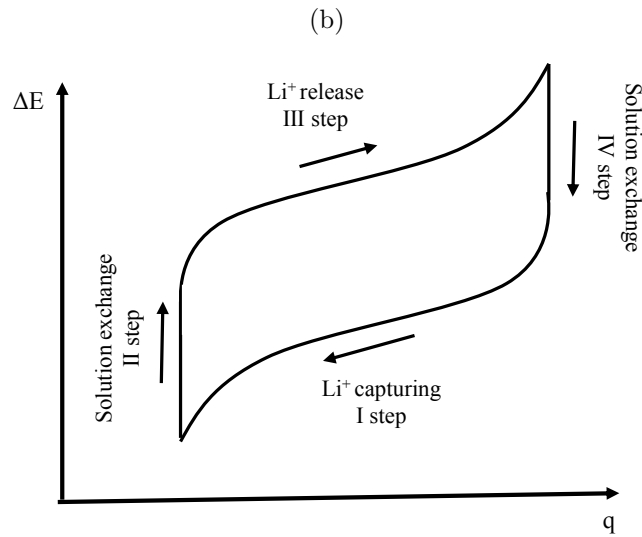
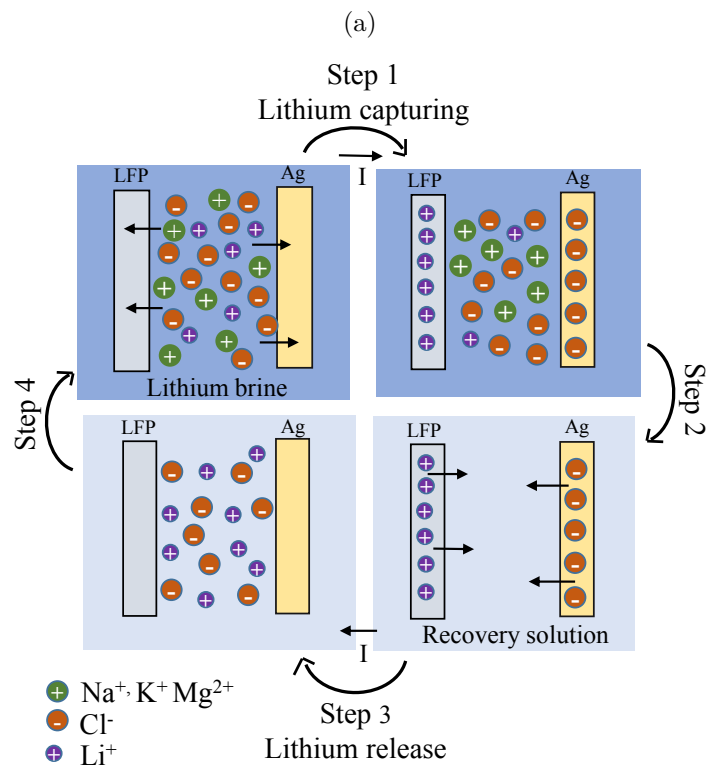


Figure 1.4: Scheme of the four stages of lithium recovery through salt capturing (a) and cell potential vs. charge (b). Adapted from [5].

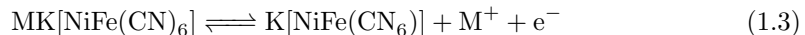
lithium recovery through salt-capturing.

Nickel Hexacyanoferrate (NiHCF) has been proposed as an efficient alternative material for substituting the Ag. It belongs to the open-framework materials family having Prussian Blue-like crystal structure. Such materials are under current development as candidates for the positive electrodes in Na- and K-ion batteries [38]. Their production method is inexpensive and they show a very good capacity retention, long cycle life and fast kinetics [39, 40]. NiHCF has an “open structure” with large interstitial sites, where alkaline cations can be hosted and transferred with fast kinetics. Details on the structure and thermodynamic behavior of NiHCF are discussed in Section 4.2.

NiHCF has been employed in lithium recovery from brines, as a lithium excluding electrode. Indeed, it shows a high affinity with sodium and potassium, compared to lithium [7]. The use of NiHCF leads to a different process scheme: during the lithium capturing (I step), which corresponds to the reduction of LFP, NiHCF is oxidized, releasing cationic species in brine. During the lithium release step (III step), NiHCF captures cations from recovery solution. This mechanism has been named selective-ion-exchange, since lithium is exchanged with the other cations present in the recovery solution. Hence, during the recovery step, the lithium concentration is increased and the concentrations of other cations is decreased in the solution. This allows the achievement of a good lithium purity, even when the starting solution is a recovery solution enriched with other species, like NaCl or KCl, such as brines. The scheme of the technique is represented in Fig. 1.5.

This technology has been tested using a solution with the same composition of the Salar of Atacama as a starting brine [7]. Salar of Atacama is one of the lakes present in the “Lithium Triangle” in South America (40 mM LiCl, 786 mM NaCl, 100 mM KCl, 70 mM MgCl₂). Hereafter this solution will be called “simil-Atacama” solution for simplicity sake. In only one cycle the recovery solution is enriched up to 92 mM LiCl concentration. Lithium purity achieved in one cycle is instead relatively low (11-75%, depending on the recovery solution used) due to the presence of other cations. The purity can be increased by making more cycles, performing further the exchange of lithium in the recovery solution.

Due to the low capacity retention of LiFePO₄ in aqueous environment [6], this material has been substituted by LiMn₂O₄ (LMO). LMO structure has tetrahedral sites where Li⁺ cations are hosted during the reduction of manganese (details on structure and intercalation of Li⁺ in LMO are reported in Section 4.1). Therefore, the semi-reactions occurring are:



LMO shows a very good selectivity against K⁺, Na⁺, Mg²⁺ and it has really good

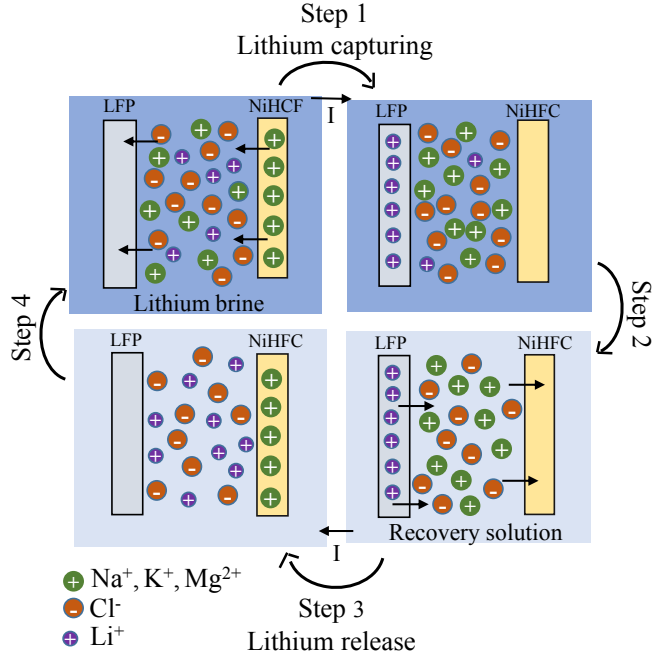


Figure 1.5: Scheme of the four stages of lithium recovery through selective ion exchange. Adapted from [7].

stability upon cycles in brine: after a capacity drop of 20% in the first cycles, it remains constant around 100 mAh/g, which is only slightly lower than the LMO capacity in aqueous battery [6].

The higher rate of lithium production is an advantage of electrochemical ion pumping techniques respect to conventional evaporation processes. An hypothetical reactor working at 0.5 mA/cm^2 , having the same volume of the evaporation tanks filled from Salar of Atacama, would extract in 8 days the amount of lithium currently extracted in one year [41]. This would give a significant contribution to lithium production, considering its predicted increasing demand.

Until now, research on lithium extraction by means of electrochemical ion pumping has focused mostly on the technique development, in order to find the best materials to obtain good lithium selectivities, reaching a high final concentration and purity and investigating the reaction efficiency. No research has been directed to the development of suitable cell geometries to run the process. Lithium enriched solution volumes are still relatively small ($350 \mu\text{L}$) and the process has been carried out in two electrochemical cells, one for the step of capturing, and another for the release [5, 6, 7, 42]. The electrodes were mechanically moved from a cell to the other between the two steps. This operation complicates the scalability of the process for industrial application. The design of a reactor

where both steps can be performed is fundamental to make this technology competitive in the industrial market, as well as the increase of volume of the final solution.

1.4 The diversification of the lithium sources

As illustrated so far, the development of lithium extraction by means of electrochemical ion pumping has focused on solutions similar to the brines available in South America, which have a relatively high concentration of lithium chloride (250-300 mg/l).

Nevertheless, the diversification of the lithium supplies may be a step forward to the global lithium production increase and to the further development and spread of technologies based on lithium ion batteries. Indeed, while USA and China are currently lithium self-producers, Europe is a net lithium importer [16]. The only net exporters of lithium carbonate are Argentina, Bolivia and Chile, that are reach of brine sources. Together with the increasing demand, the economic monopoly of lithium production is the main reason of lithium price soaring. Therefore, the opportunity to employ other and more diluted sources of lithium, situated in various parts of the world, could be of worldwide interest. Such sources are relatively widespread, and include geothermal waters, brines produced in salt-works (10-50 mg/l of lithium concentration), waste waters from gas and oil extraction wells.

Extraction of lithium from diluted brine has been widely investigated [17], as it may be a fundamental step towards the future extraction of lithium from seawater (170 $\mu\text{g/l}$), considering that the oceans, with their estimated-amount of $2 \cdot 10^6$ Mtons of lithium, could be an unlimited lithium source in the future [13].

The main problem of extraction from diluted brine is obviously low concentration of lithium that makes the capturing step quite inefficient. High amount of other alkali metals and additional species in solution make the process even more challenging.

Ion-exchange by resins are employed in semi-industrial scale in United States for lithium extraction from salt lakes [43], and precipitation through alumina salts have been investigated for the extraction from thermal waters in Japan [44, 45] and from the Dead Sea in Israel [19, 21]. Concentration of lithium in these brines is circa 10 mg/l. These processes reach good yields (circa 90-95% [21, 45]) through prior modification of brine pH, if no competitive metals or other disturbing species are present in solution. Hence upstream processes like precipitations or chemical treatments are necessary for brine modification, as well as downstream processes to separate lithium from the active material after the capturing [15].

The use of electrochemical ion pumping for extraction of lithium from diluted brine is attractive for the insertion mechanism in the active material, that involves only electrons as a reactant, and it does not require the use of other chemicals for the final separation.

The final product is a pure and concentrated LiCl solution, which is easily converted in Li_2CO_3 (the final product to be sold in the market), through precipitation with Na_2CO_3 .

1.5 Aim of the work

The aim of this PhD thesis is to develop a prototype of electrochemical reactor for the extraction of lithium from diluted brine sources by means of electrochemical ion pumping.

The materials selected for the process are LiMn_2O_4 as lithium capturing electrode and NiHCF as lithium excluding electrode, because of their several advantages already discussed in Sect. 1.3.

The basic point is the design of a suitable geometry, aimed at reaching high capturing efficiencies, which is the weak point of the extraction from diluted brine. The other purposes are performing the entire process (capture and release) in the same cell and obtaining higher volume of LiCl concentrated solution than in previous works.

The thesis is structured as follows: after a brief summary of the scientific background (Chapter 2), the experimental equipment and measurements employed are described (Chapter 3). A study of the thermodynamic behavior of the selected materials during intercalation (LiMn_2O_4 and NiHCF) is reported (Chapter 4). Chapter 5 is dedicated to the study of the capturing step of the process. The capture efficiency is studied by changing some process parameters (brine concentration, electrodes mass loading, current, electrolyte flow rate), in order to find the best working conditions of the reactor. A mathematical model of the capturing is developed to support and explain the experimental results. Modelling the reactor behavior is very important from an engineering point of view, since it gives a method to size the process components (electrodes, volume of solution, volume of cell) and to choose the best parameters.

Finally, Chapter 6 includes the results of the entire process (both capturing and release steps), an estimation of the electric energy required by the process, and a rough analysis of its economic sustainability.

Chapter 2

Theoretical Background

Electrochemical processes have been used for decades in many industrial branches, such as production or refinement of metals (like aluminium, copper, etc.), production of gaseous elements such as hydrogen or chlorine, synthesis of chemicals, deposition of metal and so on.

The electrochemical reactions are heterogeneous processes and they show many similarities with catalytic reactions. A typical electrochemical process consists of different steps, both chemical (e.g the adsorption) and physical (e.g the transport of the ions and the transfer of the electrons).

A scheme of a typical electrochemical reactor is shown in Fig. 2.1.

The main components are two solid electron-conductive phases, called electrodes, where the semi-reactions occurs (particularly, oxidation at the anode and reduction at the cathode) and an ion-conductive phase, the electrolyte, that separates the two electrodes, which contains the reactants and the products. Membranes or separators may be present between the two electrodes, for example when the species produced at one electrode are consumed at the counter electrode, or when mixing of products has to be prevented.

An electrochemical reactor can be either used to deliver electric energy from different sources (for example from thermal or chemical ones), and in this case it is known as “battery”, or to supply chemical products. In this latter case, it is called “electrolyzer” and it works through the application of a current from an external source.

In some cases the reactor or cell can work in both the directions, as in the case of a rechargeable battery or an electrochemical ion pumping, where the reactions occur spontaneously in one direction generating energy (the so-called “battery discharge” step), and non-spontaneously in the other direction (the “battery charge” step) requiring energy. Indeed the rechargeable or secondary batteries are also considered as “accumulators” of energy, because once charged they can store the electrical energy under the form of

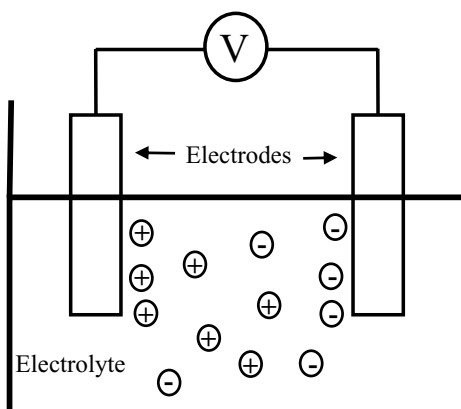


Figure 2.1: Scheme of an electrochemical cell.



Figure 2.2: Galvani representation of an electrochemical cell

chemical energy.

The next Section briefly presents the working mechanism of an electrochemical process.

2.1 Electrochemical principles

An electrochemical reactor is a galvanic cell consisting of several phases in contact. An example of galvanic cell is shown in Fig. 2.2. Among the present phases, there are always two solid electron-conductive phases (α and α'), the electrodes (β and β') and an ion-conductive phase, the electrolyte (ϵ).

At open circuit an electrochemical equilibrium is established at each interface between two different phases. In this case, the electrical species, electron or ion, that can exist in both phases in contact, are not subjected to any net transport from a phase to another: the electrochemical potentials of the species $\tilde{\mu}_i$ in the two phases are equal.

$$\tilde{\mu}_i^\alpha = \tilde{\mu}_i^{\beta}. \quad (2.1)$$

The index i indicates the species and the Greek letters the phases in contact. From Eq. 2.1, the difference of potential at the interface can be evaluated, which corresponds to the transport electric work of the species across the interface.

The difference of potential between the two phases is established by an electric field that is created across the interface. This is due to the orientation of the solvent molecules

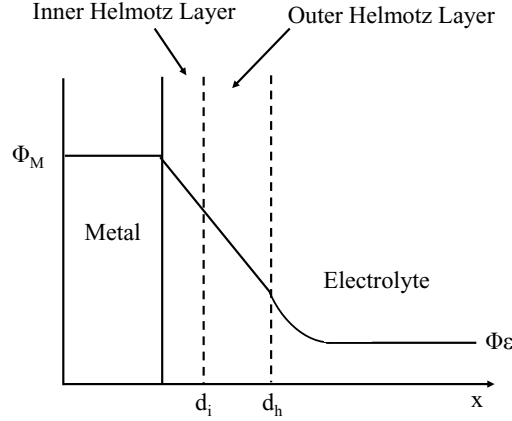


Figure 2.3: Potential profile along the distance at the solid liquid interface according to the Stern model.

or to a previous exchange of ions that pass from a phase to the other upon contact, before achieving the equilibrium.

In a solid/liquid interface, the ions have a distribution in the liquid, that is well described by the Stern model.

According to the Stern model, who has combined together two previous models (the “Helmholtz model” and the “Gouy-Chapman model” [46]), two main regions can be distinguished near the interface, the “compact double layer” (CDL) and the “diffuse double layer” (DDL), where the ions are differently distributed.

The compact double layer, or outer Helmholtz plane (OHP), is a region where the electrostatic forces between the charged metal and the ions prevail on the thermal agitation of the solution. The OHP is the plane formed by the center of the solvated ions nearest to the interface. In this region, the metal and the ions can be assumed to be two parallel planes, and their capacitance is well described by the capacitance of a parallel plate condensator:

$$C_{cdl} = \frac{\epsilon_r \epsilon_0}{d_H} \quad (2.2)$$

where ϵ_r is the medium relative permittivity, ϵ_0 is the dielectric constant of the vacuum, and d_H is the distance between the two plates, called “Helmholtz distance”. In this region, the potential drop is linear.

Within the OHP, it may be present also the inner Helmholtz plane (IHP), formed by the ions that have lost their solvation shell and that have adsorbed chemically or physically on the electrode surface.

The diffuse double layer is the region adjacent to the compact double layer farther

from the interface, where the electric forces generated by the charged electrode are weaker than the thermal agitation of the solution. Therefore the ions are more dispersed in the solution, forming the so-called “diffuse double layer”, in which the potential drops exponentially. A scheme of the potential distribution near the interface is shown in Fig. 2.3.

The total potential difference of the galvanic cell at the equilibrium, called “open circuit voltage” ($E_{eq}^{B'B}$), can be read through a voltmeter at the terminal clamps, and it can be evaluated from the sum of the transport electric works at each interface. The anode is the electrode where the reaction of oxidation occurs producing electrons, the cathode is the electrode where the reduction reaction occurs, consuming electrons. In this way, the electrons move from the anode to the cathode through an external circuit, producing the current. $E_{eq}^{B'B}$ is defined for convention as the difference between the potential of the cathode and the potential of the anode, $V_C - V_A$.

$E_{eq}^{B'B}$ is linked to the ΔG of the global reaction of the galvanic cell:

$$E_{eq}^{B'B} = -\frac{\Delta G}{RT} \quad (2.3)$$

where R is the gas constant and T is the temperature.

If the ΔG of the reaction is negative, ($V_C > V_A$), the electrons go from a point at low potential to a point at high potential, and the reaction occurs spontaneously. In this case the electrochemical cell works as a battery. If ΔG is instead positive, ($V_C < V_A$), the electrons go in the opposite direction and an external work must be performed on the cell for the reaction to occur.

The potential of an electrode can not be measured as an absolute property, but always with respect to the potential of another electrode. By performing a measurement with only two electrodes, the measured potential is the total cell potential difference. In order to study the potential of a single interface, a third auxiliary electrode is needed, called reference electrode. A reference electrode is an ideal-non-polarizable electrode, i.e. an electrode whose potential does not change appreciably if a current flows through it.

The use of reference electrode is very common in electrochemistry, the usual configuration of the electrochemical cell is in Fig. 2.4. While the current flows mainly between the working and the counter electrode (anode and cathode), the potential registered or controlled by the potentiostat is the difference between the potential of the working electrode and the reference electrode. The working electrode can be chosen arbitrarily, depending on which potential electrode has to be controlled or which electrode is studied.

When the current is circulating in the external circuit, the cell voltage differs from

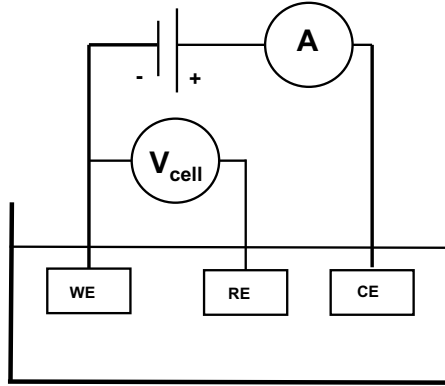


Figure 2.4: Schematic representation of an electrochemical cell with reference electrode.

the open circuit voltage. This difference is due to the overpotentials of the process. In particular, it will be equal to:

$$E^{B'B} = E_{eq}^{B'B} + \eta_C + \eta_A + \eta_\Omega \quad (2.4)$$

η_C and η_A are the overpotentials of the reduction and oxidation semi-reactions respectively. η_Ω is instead the overpotential due to the Ohmic drops, linked to the electric resistance of the solution. This quantity follows the Ohm law, as follows:

$$\eta_\Omega = R_l I \quad (2.5)$$

where I is the applied current, and R_l is the electrical resistance of the electrolyte.

The overpotential of the semi-reaction can be distinguished in two main contributes: the overpotential due the charge transport, and the overpotential due to the mass transport.

The charge transfer overpotential is due to the transport of charged species through the solid/liquid interface. The equation that expresses the relationship between the density current i and the electrode overpotential η_{ct} is the well-known Butler-Volmer:

$$i = i_0 \left(e^{\frac{\alpha n F}{RT} \eta_{ct}} - e^{-\frac{n F (1-\alpha)}{RT} \eta_{ct}} \right) \quad (2.6)$$

where i_0 is the exchange current density, α is the symmetry barrier coefficient, n is the number of the electrons involved and F is the Faraday constant.

The mass transfer overpotential is due to the depletion of the reactant concentration near the interface. This phenomenon slows down the reaction rate, and a higher overpotential is necessary to maintain the same current density. If the mass transport is the rate determining step of the entire process, the mass transfer overpotential η_{mt} is equal

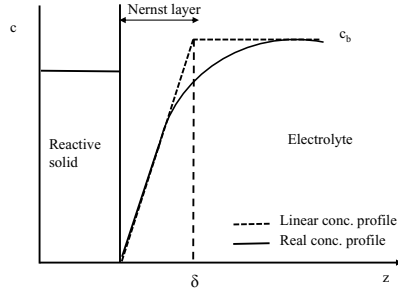


Figure 2.5: Representation of the concentration profile at the liquid solid interface during the reaction and of the Nernst limit layer approximation.

to:

$$\eta_{mt} = \frac{RT}{F} \log\left(1 - \frac{I}{I_l}\right) \quad (2.7)$$

I_l , called “diffusion limiting current”, is the current correspondent to the maximum diffusion flux of the species from the bulk to the interface, when the reactant concentration at the interface is equal to 0. It represents the maximum current that the system can reach. It is defined as:

$$I_l = \frac{nFC_i^b D_i A_e}{\delta} \quad (2.8)$$

where n is the number of electrons involved in the reaction, C_i^b is the bulk concentration of reactant in solution, D_i is the diffusion coefficient of the reactant in the solution, A_e is the electrode area and δ is the thickness of the so-called “Nernst diffusion layer”. If the concentration profile near the interface is approximated with a linear profile (see Fig. 2.5), the Nernst diffusion layer is the distance between the interface and the point where the reactant concentration is equal to its bulk concentration.

There are other types of overpotentials, specific for different systems. For example, in the case of a metal deposition, there is a special overpotential due to the incorporation of the adsorbed atoms in the crystal lattice of the metal.

The amount of oxidized or reduced species during the electrochemical reaction linearly depends on the charge Q passed into the system by means of the well-known Faraday law:

$$m_i = nFQ \quad (2.9)$$

where m_i is the amount of moles of reduced or oxidized species and n is the number of electrons involved in the reaction.

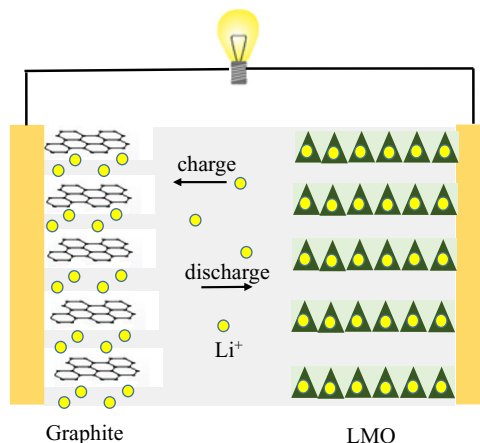


Figure 2.6: Schematic representation of Li^+ insertion in graphite and of intercalation in LMO in a classic lithium-ion battery.

2.2 Intercalation processes in a battery-like material

The intercalation is the main working mechanism of rechargeable batteries. In the 70's, the first lithium-ion battery has been invented based on the insertion of Li^+ in a hosting structure, which is used as electrode.

The intercalation mechanism consists on the electrochemical reduction of the electrode, which involves the movement of a cation from the solution inside the solid structure, where it is hosted. Contrary, during the oxidation, the cation is driven out from the solid to the liquid. A schematic representation of lithium ion battery is reported in Fig. 2.6.

If the solid has a bi-dimensional structure (planes), like graphite, then the mechanism is known as insertion. If the structure is three-dimensional (cube, tetragons), it is known as intercalation. The intercalation is intrinsically a reversible process, that makes the battery rechargeable.

A distinction between single phase intercalation and two-phases intercalation exists. In the two-phases intercalation, the solid structure changes its phase during the cation intercalation, and the phase arrangement depends on the amount of cation intercalated. An example of a two-phases material is the LiMn_2O_4 . Intercalation in LMO is further discussed in Sect. 4.1.

If the solid material has a selectivity towards a certain cation species, one cationic species from the solution is mainly intercalated. The selectivity can derive from the size of the crystal lattice where the cation is hosted. For example $\lambda\text{-MnO}_2$, which is a spinel type manganese oxide, can host cations in the tetrahedral sites, during the reduction of

manganese. Due to the narrowness of these sites, only small or completely dehydrated cations can be inserted. That is the reason why λ -MnO₂ shows a high selectivity towards lithium among alkaline, alkaline-earth and transition metal ions [47].

If the material has no selectivity towards a cationic species, different cationic species from the solution can be intercalated, if present. This is what happen for example with Prussian blue materials [48].

In this Section, the ideal thermodynamic model of intercalation typically presented in literature (see e.g. Ref. [49]) is summarized, for a single cationic species intercalated in the host structure.

At the solid liquid interface, the electrochemical potentials of the transported species (the cation) is valid at equilibrium [46]:

$$\tilde{\mu}_{A^+}^S = \tilde{\mu}_{A^+}^L \quad (2.10)$$

The intercalation reaction is symbolically represented as:



where O represents the oxidized state of the material, namely the empty active site, R represents the reduced state, namely the occupied site by the cation, e⁻ is the electron and A⁺ is the intercalated cation.

The equilibrium can be further expressed through the electrochemical potentials of the charged species $\tilde{\mu}_i$ and the chemical potentials of the neutral species μ_i in the solid participating to the reaction:

$$\tilde{\mu}_{A^+}^S = \mu_R - \mu_O - \tilde{\mu}_e \quad (2.12)$$

Combining Eqs. 2.10 and 2.12 and developing the expression of the electrochemical potentials, the following expression is obtained:

$$\Delta\phi_H - \frac{\mu_e}{F} = \frac{\mu_{A^+}^L - \mu_R + \mu_O}{F} \quad (2.13)$$

where $\Delta\phi_H$ is the difference of the inner potentials (or Galvani potentials) between the solid phase and the liquid phase. The left term of Eq. 2.13 is the measurable potential of the electrode E with respect to a reference electrode.

Eq. 2.13 can be further developed, defining the chemical potential of the redox species:

$$\mu_R = \mu_R^0 + RT \ln a_R \quad (2.14)$$

$$\mu_O = \mu_O^0 + RT \ln a_O, \quad (2.15)$$

where a_R and a_O are the activities of the reduced and the oxidized species. μ_i^0 indicates the standard chemical potentials of the species i , which are constant terms.

Substituting Eqs. 2.14 and 2.15 in Eq. 2.13 and developing the chemical potential of the cation in the liquid, assuming that the electrolyte is an ideal solution, the well-known Nernst equation is obtained:

$$E = E_A^0 + \frac{RT}{F} \ln \frac{C_A}{C_0} + \frac{RT}{F} \ln \frac{a_O}{a_R} \quad (2.16)$$

where E_A^0 is the standard potential of the intercalation reaction and it is defined as:

$$E_A^0 = \frac{\mu_A^0 - \mu_R^0 + \mu_O^0}{F}, \quad (2.17)$$

C_A is the concentration of the cation in the solution and C_0 is a reference concentration, typically 1 M. The equilibrium potential depends on the cation concentration in the liquid and on activities of redox species in the solid.

If C_A keeps constant with the potential, namely the amount of intercalated cations is negligible respect to the amount of cations in solution, the term $\frac{RT}{F} \ln \frac{C_A}{C_0}$ can be incorporated in E^0 and the equation can be written as:

$$E = E_A^{0'} + \frac{RT}{F} \ln \frac{a_O}{a_R} \quad (2.18)$$

For expressing the activities of the reduced and oxidized species, a model was developed by McCargar et al. [49], in which the interface potential has been related to the Gibbs mixing energy of the two species.

Indeed, McCargar modelled the solid structure as a mixture between the two species (O and R), namely as a network of single cells (the interstitial sites) that can be free or occupied by the cation [49]. The molar free energy mixing for a general solution is defined as:

$$\Delta G_m = \Delta H_m - T\Delta S_m = (1-x)RT \ln a_O + xRT \ln a_R, \quad (2.19)$$

where ΔH_m is the molar enthalpy of mixing and it represents the heat that is evolved or adsorbed during the mixing, in our case during the intercalation. ΔS_m is the molar entropy of mixing, x is the molar fraction of the reduced species and $1-x$ is the molar fraction of the oxidized specie.

Making the derivative of Eq. 2.19 with respect to x , and considering the thermodynamic property of a mixture of two components, expressed by the Gibbs-Duhem equation,

$$xRT d \ln(a_R) + (1-x)RT d \ln(a_O) = 0, \quad (2.20)$$

the follow expression can be obtained:

$$\frac{\partial \Delta G_m}{\partial x} = RT \ln \frac{a_O}{a_R}, \quad (2.21)$$

Comparing this last equation with Eq. 2.18, one obtains:

$$\frac{\partial \Delta G_m}{\partial x} = RT \ln \frac{a_O}{a_R} = F \Delta E, \quad (2.22)$$

where $\Delta E = E - E_A^{0'}$.

Therefore, integrating the equilibrium potential respect to the fraction of charge, one can extrapolate the Gibbs mixing energy of the “solid solution”.

The ΔG_m is conventionally divided in two contributes, the ideal mixing energy ΔG_{id} and the excess mixing energy G_{exc} . If the solution is ideal, namely the species are randomly mixed in the lattice and no interaction between the cells of the lattice is assumed to take place, ΔG_m is equal to the Gibbs mixing energy of a mixture of ideal gases and the activities of the species are equal to their molar fraction:

$$\Delta G_{id} = x_1 RT \ln x_1 + x_2 RT \ln x_2, \quad (2.23)$$

In this case, through Eq. 2.22, the intercalation potential becomes:

$$E = E_A^{0'} + \frac{RT}{F} \ln \frac{1-x}{x} \quad (2.24)$$

The G_{exc} is defined as the difference between the mixing energy of an ideal solution and the mixing energy of a real solution and it takes into account the non-ideality of the system (interaction between particles, change of the volume during the mixing, non-randomly distribution). This contribution can be included in the expression of the potential:

$$E = E_A^{0'} + \frac{RT}{F} \ln \frac{1-x}{x} + \frac{1}{F} \frac{\partial G_{exc}}{\partial x} \quad (2.25)$$

The last term of this equation can be renamed as “excess potential” and can be related to the activity coefficients of the species, γ_O and γ_R :

$$\frac{\partial G_{exc}}{\partial x} = RT \ln \frac{\gamma_O}{\gamma_R} \quad (2.26)$$

γ_O and γ_R are function of x . The expression of the potential can be therefore remodulated as:

$$E = E_A^{0'} + \frac{RT}{F} \ln \frac{1-x}{x} + \frac{RT}{F} \ln \frac{\gamma_O}{\gamma_R} \quad (2.27)$$

Comparing this last equation with Eq. 2.18, one can conclude that the activities of the species in the lattice can be simply defined as the product of the molar fraction and the activity coefficient of the species i .

If the concentration in the liquid changes appreciably during the reaction as it occurs in electrochemical ion pumping for lithium recovery, another term must be taken into account. In this case the potential expression becomes:

$$E = E_A^0 + \frac{RT}{F} \ln \frac{1-x}{x} + \frac{RT}{F} \ln \frac{\gamma_O}{\gamma_R} + \frac{RT}{F} \ln \frac{C_A + \frac{Q}{VF}}{C_0} \quad (2.28)$$

where Q is the total charge passed in the system and may be positive or negative, depending if reduction or oxidation has occurred, and V is the volume of the solution.

2.3 Electrochemical measurements

The electrochemical measurements performed during this PhD work were the Galvanostatic Cyclings with Potential Limitations (GCPL). They consist in applying a constant current to the electrochemical cell and measuring the working electrode (WE) potential or the cell voltage. When the WE reaches a certain potential, the current direction is switched and the opposite reaction occurs. The WE potential is expressed as a function of the charge flow Q evaluated as the integral of the current over time.

This technique is frequently used to investigate batteries [50, 51] and other electrochemical processes such as ion pumping for water deionization and recovery of salt [3, 4, 36], since it simulates the real working mechanism at constant current.

Currents applied in GCPL are often expressed in C-rate, where 1 C rate is the current needed to fully (dis)charge the electrode in one hour. An example of GCPL of NiHCF in K_2SO_4 is represented in Fig. 2.7. In the x-axis the reported value of x is defined as Q normalized by Q_{max} , the maximum value of charge that the electrode can store.

During the reduction of iron in NiHCF structure, a cation is intercalated in the interstitial sites to keep the electro-neutrality of the crystal. If the process occurs near the equilibrium condition, it continues until the sites are not completely filled (when the fraction of charge x is equal to 1). The difference between the oxidation and the reduction branches is due to the overpotentials of the process, which is never at equilibrium.

Deriving the charge Q with respect to the potential gained from GCPL, the “differential charge” is obtained, which represents the “capacitance” of the material and it is expressed in Farad or mAh V^{-1} . Physically the differential charge represents the amount of charge that can be stored in the electrode upon a small variation of its potential. A high differential charge means that the voltage is fairly stable upon long discharging. Since

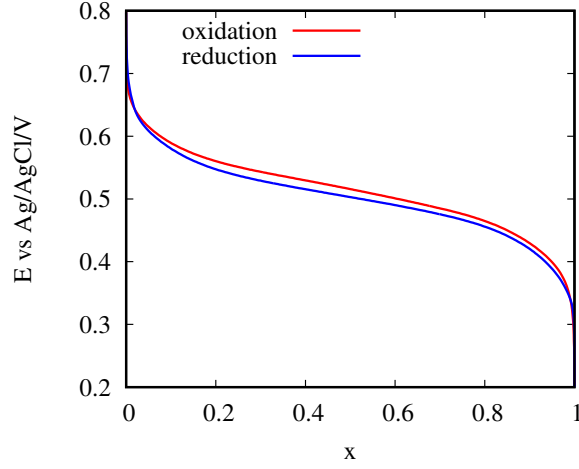


Figure 2.7: Galvanostatic cycling of NiHCF in 0.5 M of K_2SO_4 vs. normalized charge by experimental Q_{max} at 1 C-rate (fraction of charge x).

this quantity does not depend on the electrode mass, it can be normalized as follows:

$$dC = \frac{1}{Q_{max}} \frac{RT}{F} \frac{\partial Q}{\partial E}, \quad (2.29)$$

where Q_{max} is the maximum charge than can be stored in the electrode. The curve dC plotted vs. potential gives many information about the process. dC extracted from the galvanostatic curve of Fig. 2.7 is reported in Fig. 2.8 (green curve). Normally, for one-phase intercalation, dC curve is bell-shaped. The position of its peak along the E -axis corresponds to the potential of the inflection point of E vs. Q curve and it represents the potential at which mostly the intercalation occurs. The curve shapes are representative of the thermodynamic and kinetic parameters of the process.

dC curves obtained for intercalation systems are comparable to the classic Cyclic Voltammetry curve. Cyclic Voltammetry measurement consists into sweeping the potential in time and recording the current circulating in the system. For an intercalation system the two techniques give the same result at the equilibrium. This is easily demonstrable defining a “normalized current” extractable from the CV curve:

$$i = I \frac{RT}{FQ_{max}S} \quad (2.30)$$

where S is the scan rate of the CV and I is the recorded current. Substituting the definition of I and S , one obtains:

$$i = \frac{dQ}{dt} \frac{RT}{FQ_{max}} \frac{dE}{dt} \quad (2.31)$$

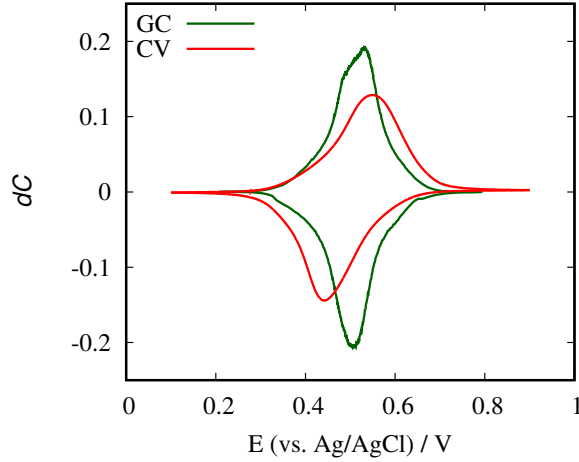


Figure 2.8: dC vs. potential E extracted from the GC and from the CV measurement in 0.5 M K_2SO_4 . The GC was performed at 1C rate, the CV at 1 mV/s.

And finally:

$$i = \frac{dQ}{dE} \frac{RT}{FQ_{max}} \quad (2.32)$$

which is equal to the definition of dC given in Eq. 2.29.

The two techniques are compared in experimental conditions in Fig. 2.8.

The curves have similar shape although they do not overlap due to the presence of overpotentials, which modify the curve shapes differently in the two cases. In both cases overpotentials translate in various effects on the shape. An advantage of dC curve respect to CV measurement is the effect of the Ohmic drop of the solution $R_l I$ on the curve shape. In the dC curve this effect shifts the curve along anodic or cathodic potentials (depending on the sign of the current), without modifying its shape, as the current is constant. On the contrary in CV measurement, this effect causes a deformation of the curves, which cannot be distinguished from the effect of other overpotentials.

2.4 Type of electrochemical reactors

There are many configurations of electrochemical reactors, different for electrode type, electrodes movement, electrolyte flow and so on. Like the chemical processes, also the electrochemical processes can be distinguished in batch and continuous operation.

The batch processes are performed in a close system where the electrodes are immersed, without any in-out flow of the electrolyte (Fig. 2.9).

The reactant concentration decreases with the time of the operation. The mixing rate is comparable to the rate of the chemical conversion, so that the concentration

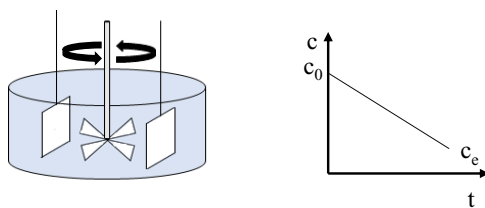


Figure 2.9: Schematic representation of a batch reactor (left) and of the reactor concentration trend with time (right) [52].

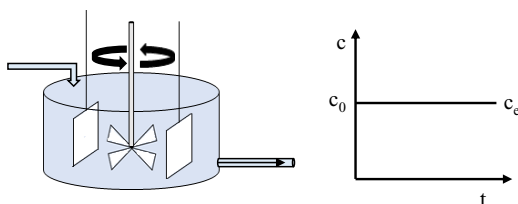


Figure 2.10: Schematic representation of a CSTR reactor (left) and of the reactor concentration trend with time (right) [52].

is kept uniform inside the volume. The processes performed in batch are for example electrowinning of noble metals, electrosynthesis of precious organic compounds or other processes with a small quantity of product. Continuous operations are instead “large” processes, such as water and chloroalkali electrolysis or metal electrowinning (for example zinc, magnesium, aluminium). Continuous operation can be performed in two kinds of reactor: the continuous stirred tank reactor (CSTR) and in plug flow reactor (PFR). In the CSTR the process occurs in a stirred tank, which is fed by a fresh electrolyte, while a flow of depleted electrolyte leaves the tank, so that the amount of volume does not change with the time (see Fig 2.10). The reactor concentration is the outer concentration, because the reactor is assumed to be well-mixed. For this reason, a reaction in the CSTR occurs always at the lowest reactant concentration and that may be a disadvantage for the kinetic of the reaction, which can easily reach the diffusion limiting current [52].

In the PFR (Fig. 2.11), the reaction occurs while the electrolyte is continuously pumped inside the reactor ideally with a constant velocity across the cross section of the channel. The reaction occurs in all the length of the reactor and a profile reactant concentration is formed between the fluid inlet and the outlet.

Typically, if the current is smaller than limiting current I_l , the concentration profile is linear with the space, while if the applied current is higher than I_l , the concentration

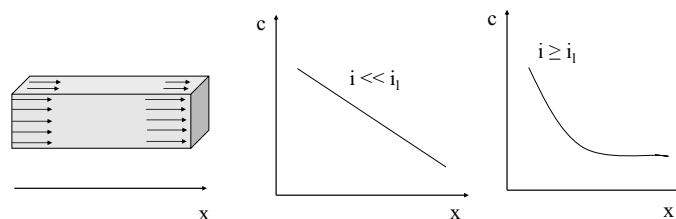


Figure 2.11: Scheme of a plug flow reactor (a) and of two concentration profiles on the reactor length. In the first case the trend is linear (b), in the second case the trend is exponential, due to the mass transport overpotential.

decades exponentially [52].

The PFR is divided in other two main groups of reactors: the reactor with fixed bed and with fluidized bed. The main difference between these two configurations is the movement of electrodes. In the fixed bed reactor the electrodes are static, while in the fluidized bed the electrodes can be metal or carbon particles that are crossed and moved by the flow. The choice of one configuration with respect to the other depends on the reaction that must be performed and on the solid active materials.

An electrochemical reactor can work with two kinds of electrodes: the flat massive electrode (two-dimensions electrode) and the porous electrode (three-dimensions electrode). Usually the second are preferred because they provide a much higher contact area. This can be essential in reactions that need low current density, for example process with a very low reactant concentration (e.g. recovery of metal from solution).

In this case, thanks to the large contact area, given by the presence of the pores, it is possible to run these processes with a usual nominal current density of 0.1-1 A/cm², although the real current density is much lower (1 mA/cm² or even less) [52].

The porous electrodes are usually classified based on the diameter of their particles. A fairly good classification has been given by Koryta and Dvorák [52]:

- The nanoporous electrodes ($1 \text{ nm} > d_p > 10 \text{ nm}$), which constitutes a microporous electrode structure (pores dimensions 0.1-1 μm). This kind of electrodes is typical for the catalysts of the fuel cells, to create a three-phase contact.
- Microporous electrode ($d_p > 0.1 \mu\text{m}$), with diameter macropores of 1-100 μm , having a thickness of the order of several millimetres. These electrodes are typical for the batteries.

- Packed bed electrodes (meshes, cloth, foams) and fluidized bed electrodes (metal or carbon particles), which are composed of particles with diameters from millimetres to centimeters. These electrodes are usually used for the electrochemical conversion of species at low concentration or for desalination and/or purification processes through metal-ion removal [53, 54]. Such electrodes beds measure centimetres to fractions of meters in thickness or bed depth respectively.

In the packed and fluidized bed reactor a convective flow is applied, pumping the electrolyte inside the reactor, in order to favour the mass transfer to the electrodes.

In this case, another classification based on the direction of the flow exists. Indeed, the packed bed reactor, can be divided in flow-by and flow-through electrodes reactor. The scheme of the two configurations is shown in Fig. 2.12 (a) and (b). The main difference regards the current and the electrolyte flow directions: in the case of panel (a) (flow-by), they are perpendicular to each other, in the case of panel (b) (flow-through), they are parallel [55]. Of course these two main categories can be rearranged in many derived configurations, that may be an hybrid between the two types. For example in the configuration reported in Fig 2.12 (c), the flow passes through the cathode, but parallel to the anode and it is perpendicular to the current direction.

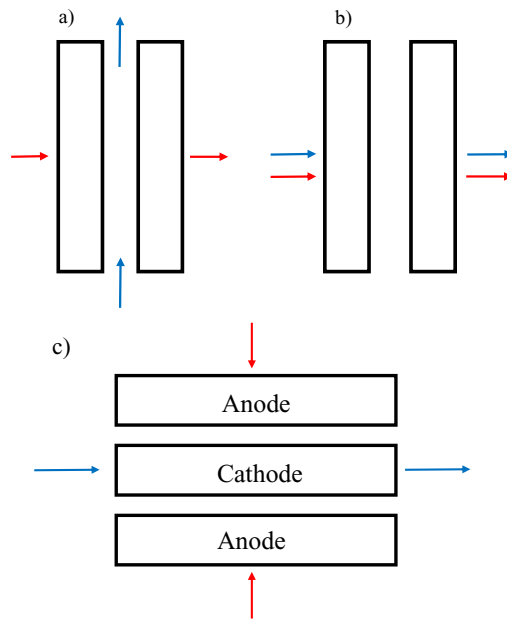


Figure 2.12: Various schemes of packed bed reactor: flow by electrodes (a), flow-through electrodes (b) and a hybrid configuration (c). The rectangles represent the electrodes, the space between them represents the separator or the gap. The black arrows indicate the flow direction, the red arrows indicate the current direction.

Chapter 3

Experimental Section

This chapter is dedicated to the description of the experimental equipment. Since the main experimental goal has been to develop a suitable cell geometry for the extraction of lithium from diluted brine, this Chapter reports in details the cells design and the electrodes descriptions.

3.1 Preparation of the electrodes

As already discussed in Chapter 1, the materials selected for the process are LMO and NiHCF. Both of them are initially in form of nanopowder, composed by particles with a diameter of 20 nm, that form agglomerates up to 100 nm. Since the LMO powder is produced commercially, a battery grade LMO powder provided by the MTI (Richmond, USA) was used, so that the process could be tested with an industrially made material already present in the market.

NiHCF nanopowder was instead synthesized by a co-precipitation method, as reported in literature [7]. The synthesis method consists on the following steps. Firstly, 120 ml of 0.05 M solution of $\text{Ni}(\text{NO}_3)_2 \cdot 6\text{H}_2\text{O}$ (Sigma-Aldrich) and 120 ml of 0.05 M solution $\text{K}_3\text{Fe}(\text{CN})_6$ at 0.05 M (Sigma-Aldrich) are simultaneously and dropwise added to 60 ml water while stirring constantly. This process is carried out at a constant temperature of 70°C. Immediately a brown precipitate is formed. After that, the material is sonicated for 30 min at 70°C and the suspension is allowed to rest overnight. After removing of the liquid part, the precipitate is centrifuged, washed with distilled water and dried at 60°C.

As discussed in Sect. 2.4, the most effective electrodes type for the extraction from diluted sources are packed bed electrodes. The active materials must be therefore arranged to form the “packed bed”. Hence, the powders were used to prepare a viscous slurry to be painted on a suitable conductive substrate, namely carbon cloth. Carbon cloth is

composed by carbon fibers interwoven with each other, forming macropores of 25-50 μm diameter. The carbon cloth thickness is about 400 μm . In addition to its porosity, carbon cloth is a suitable material for packed-bed reactor thanks to its compressibility, which allows to press the electrodes against each other, minimizing the bed length and the space between the electrodes.

The slurry consists of the active material, C65 carbon black (Timcal, specific surface area 62 m^2/g), polyvinylidene difluoride (Solef S5130, Solvay), and graphite (Timcal SFG6) with 80:9:9:2 wt. % for the NiHCF slurry and 80:10:10:0 wt. % for LMO respectively [7]. The carbon and the graphite increase the conductivity of the active material, while the polyvinylidene difluoride works as a binder within the components. The powder was dispersed in the N-methyl-pyrrolidone (NMP) and mixed thoroughly for 30 min at 4000 rpm by using an ultra-turrax disperser. The electrodes were prepared by hand painting the slurry on carbon cloth and subsequently dried at 60°C to evaporate the NMP.

NMP volume was tuned to modify viscosity and size of agglomerated particles. Specifically, the slurry becomes denser and viscous by decreasing the NMP volume, and the size of the agglomerated particles is bigger after drying. These particles occupy smaller volume of carbon cloth, forming a lower compact layer on fibers and leaving empty big pores of carbon cloth, thus decreasing pressure drops. This expedient was used to decrease the pressure drop on NiHCF electrode, which shows the highest drop (see Sect. 5.6). NMP volumes of 3.6 or 1.8 μl were used per milligram of slurry.

Details on the sizes and shapes of electrodes are discussed in the following paragraphs, since they depend on the cell geometry.

LMO and NiHCF electrodes were electrochemically prepared before the use. LMO electrodes were galvanostatically cycled one time in a “similar-Atacama” solution in order to measure their specific charge, and then completely oxidized. NiHCF electrodes were instead cycled one time in 1 M NaCl and then reduced.

In addition to LMO and NiHCF electrodes, silver was used as reference electrode, in form of slurry or metallic wire. The Ag powder (supplied by MTI) was mixed to form the slurry with the same procedure used for LMO.

3.2 Design of the cell

As already mentioned, ion capture from diluted sources should be conducted in a cell where advection flow is present, in order to increase ionic transport. Based on this, the best cell configuration has to be chosen. Generally, the flow-through electrodes (FTE) is preferred to the flow-by electrodes (FBE) design for two main reasons. The first is that the FTE configuration allows to have a better compactness of the cell. Indeed, on

contrary to FBE, the space between anode and cathode is not the main flow channel for the electrolyte. This allows to decrease the distance between electrodes, reducing the Ohmic drops and the cell volume [53].

The other main advantage is more related to the system physics. In the FBE configuration, advective flow is parallel to the electrode surface. This allows to bring always fresh electrolyte inside the cell, but it does not have a strong effect inside the electrodes pores, where the transport occurs mostly through diffusion and migration. Instead in the FTE configuration, the fluid is pumped inside the material pores. This provides fresh reactant along the total thickness of the electrode and it creates a more intimate contact between the flow and active material.

Moreover, packed bed reactors with flow-through electrodes configuration have been historically developed and studied for removal of diluted metals from industrial stream [56, 57, 58, 59, 60]. More recently, this technology has been applied also for water desalination through capacitive deionization [61, 62, 63].

On this grounds, the flow-through electrodes cell was selected as the most suitable for the process.

In next paragraphs two cells used for developing and investigating the process are described. The first geometry has been designed to perform the capturing step, investigating the capture efficiency at various parameters. The second one has been used to carry out the total process (both capture and release).

3.2.1 Cell geometry to investigate the capturing step

The first cell design is shown in Fig. 3.1. The cell was composed by a plastic rounded shell, where the electrodes were located, and by a cover that allows the cell closure and the pressing of the electrodes together, as shown in Fig. 3.1. The carbon cloths were cut into 4.5 cm-diameter discs, painted with the active material only in the center, for a diameter of circa 12 mm. An insulating varnish (Lacomit, Plano GmbH) was applied on the unpainted part to avoid the occurrence of side reactions. The electrolyte flowed from the bottom to the top, through two funnel-shaped holes, located in correspondence of the active area of the electrode. In this way the flow should ideally pass only across this area. Two titanium frits were put on the inlet and outlet holes to press the stack of electrodes and separators and to make the flow more homogeneous on the active area.

The electrodes were put in the cell one on the top of the other, separated by filter paper 130 μm thick. Two types of electrodes arrangements were used. The first was a four-electrode set-up: Ag/AgCl electrode used as RE on the bottom, then the LMO electrode (WE), the NiHCF electrode (CE), and finally a second Ag/AgCl on the top, as shown in Fig. 3.1.

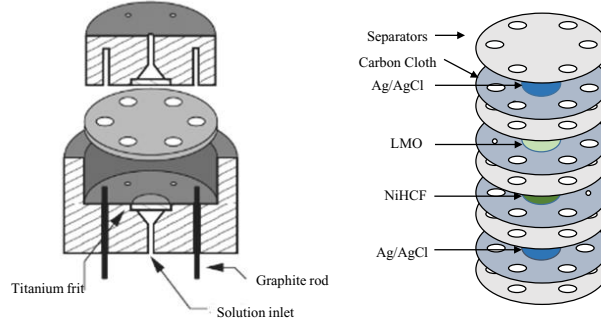


Figure 3.1: Representation of the cell (vertical section) on the left. The grey disk represents the electrode. On the right, the arrangement of the electrodes, one in top of the other, separated by a filter paper of the same size [64].

The Ag/AgCl electrodes were prepared applying a constant potential of 0.5 V on the Ag electrodes in 3 M KCl for 10 minutes. Ag/AgCl electrodes were directly immersed in the solution, because the solution contained always chloride ions. With this assembly of the electrodes, the WE potential was read by means of one reference electrode and in the meantime an open-circuit voltage (OCV) measurement was performed between the two references to monitor the Ohmic drop in the cell.

The second configuration used was a three electrodes cell (LMO as WE, NiHCF as CE and Ag/AgCl as a RE), where the reference electrode was a silver wire prior anodized in a solution of 3M KCl, inserted in the cell through one of the holes. Silver wire was later preferred as reference electrode, due to its higher stability upon time and cycles compared to the silver slurry electrode, whose stability was affected by the flow.

Once the cell was closed, four graphite rods were inserted through the sealed holes in the shell. Each rod pierced only one electrode, passing through the holes of the other electrodes cut previously. The ends of the graphite rods, outside the shell, were connected with the Biologic VSP-300 potentiostat.

As the NiHCF capacity is 60 mAh/g and the one of LMO is ≈ 105 mAh/g, the active material masses ratio of LMO and NiHCF was 1:4, to be sure that the NiHCF charge was larger than LMO charge.

The potential measured through the potentiostat is the difference between the WE and the RE, ΔV . The potential of RE (Ag/AgCl immersed in the solution) depends on the chloride concentration as follows:

$$E_{RE} = E_{Ag/AgCl}^{\circ} - \frac{RT}{F} \log \frac{a_{Cl^{-},exp}}{a_{Cl^{-},ref}}, \quad (3.1)$$

where $E_{Ag/AgCl}^{\circ}$ is the standard potential of the Ag/AgCl vs. SHE, $a_{Cl^{-},exp}$ is the activity of Cl^{-} ions in the solution and $a_{Cl^{-},ref}$ is the activity at a chosen reference concentration.

In order to get rid of the well-known thermodynamic dependence of the potential on lithium concentration, the measured potential is referred to a fictitious “relative lithium electrode” (RLE), whose potential E_{RLE} vs. SHE is:

$$E_{RLE} = E_{RLE}^{\circ} + \frac{RT}{F} \log \frac{a_{Li^{+},exp}}{a_{Li^{+},ref}}, \quad (3.2)$$

where $a_{Li^{+},exp}$ is the activity of Li^{+} ions in the solution and $a_{Li^{+},ref}$ is the activity at a reference concentration. Taking arbitrarily $E_{RLE}^{\circ} = E_{Ag/AgCl}^{\circ}$, the E of the WE can be rewritten vs. the fictitious RLE as:

$$\begin{aligned} E &= \Delta V + E_{RE} - E_{RLE} \\ &= \Delta V - \frac{RT}{F} \log \frac{a_{Cl^{-},exp}}{a_{Cl^{-},ref}} - \frac{RT}{F} \log \frac{a_{Li^{+},exp}}{a_{Li^{+},ref}}. \end{aligned} \quad (3.3)$$

Therefore, even if the concentration in the solution changes, the imposed extreme values of the potential of the galvanostatic cycle are the same for E vs. RLE and the effects of the Nernst equation are not considered in the result analysis. The $a_{Li^{+}}$ was approximated with the concentration of Li^{+} , while $a_{Cl^{-}}$ was evaluated using the activity coefficients reported in literature [65] as a function of the concentration of chloride ion.

The electrolyte was continuously pumped from a beaker by a peristaltic pump. The solution was stirred, to keep the concentration homogeneous. The investigated range of volumetric flow rate in this cell was 0.1-50 ml/min. A measurement of the pressure was carried out through a barometer.

This reactor was designed to perform the capturing step, investigating the efficiencies. The recovery step was never performed with this cell, because of its high volume compared to the active material volume. The recovery step must be performed in a very compact cell, where unnecessary volumes are minimized. Dead cell volumes can dilute the recovery solution, decreasing the final lithium concentration. Based on that, the cell described in the next paragraph has been designed to perform the entire process.

3.2.2 Final reactor design

The second cell has been designed in order to minimize dead volumes of the cell through a good compactness. Therefore the cell was simply made of two identical rounded plates with a funnel-shaped hole in the center and six equally-spaced holes at the border, as shown in Fig. 3.2. The electrodes were placed between the plates, one on the top of the other. Once that the electrodes are placed, the plates are fixed and pressed through six screws passing by the holes.

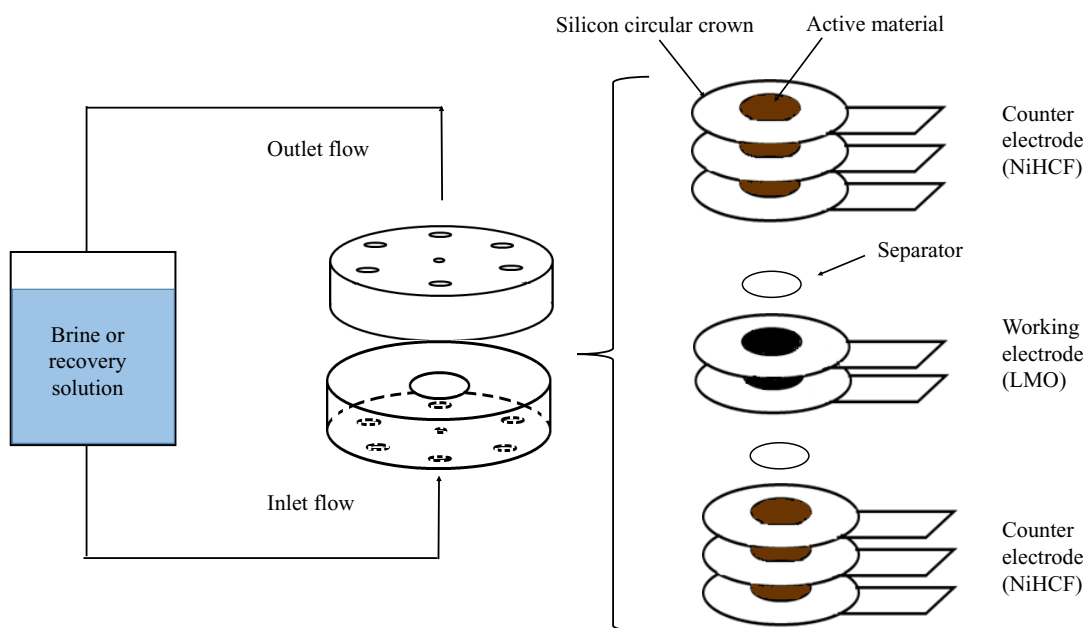


Figure 3.2: Representation of the cell plates (left) and of the electrodes stack (right).

The electrodes were made as follows. The carbon cloth was cut rounded-shape (1.4 cm^2), with an additional rectangular strip of approximately 0.5 cm^2 , as shown in Fig. 3.2. Once cut, the carbon cloth was surrounded by a circular silicone crown, attached to its edges. The area not covered by the silicone was painted by the active material and it had the same size of the fluid inlet area of the cell (1.1 cm^2). In this way, the silicon blocked any water leakage, forcing the flow to pass through the active area.

Once that the cell was closed, the contact with the potentiostat was made through the carbon cloth strip, which was left free from the silicon and protrudes from the plates. The electrodes stack had a sandwich configuration, with the working electrode placed between two counter electrodes, divided by paper separators on each side. The WE was composed by two short-circuited LMO foils, each counter was made by three NiHCF foils. This configuration was preferred to a classic configuration with alternating cathode anode electrodes, because it minimizes the number of paper separators that absorb solution creating dead volume. Placing the working electrode in the middle between the counter electrodes allows also to reduce the Ohmic drop. The total potential cell was recorded by the potentiostat, with two-electrodes measurement.

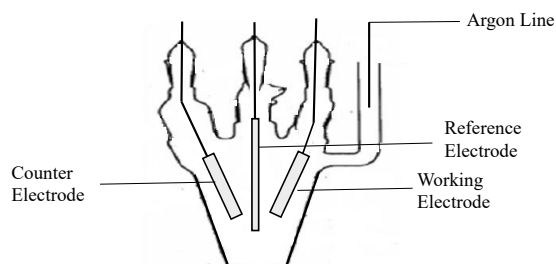


Figure 3.3: Representation of the conical cell.

3.2.3 Other electrochemical cells

Another cell geometry was used for the initial study of the materials. Its representation is reported in Fig. 3.3. The cell had a conical shape, the WE and the CE were placed in front of each other, and the reference electrode was placed in the middle between the two. The electrodes in this case were rectangular, with a size of approximately 2 cm^2 . The cell was also equipped with an entrance for the injection of the argon, that was used to bubble the electrolyte before the experiments to avoid any reaction with the oxygen.

The electrolyte was motionless (no mechanical stirring was applied during the experiments) except for possible natural convection. The reference used was $\text{Ag}/\text{AgCl}/3 \text{ M KCl}$ for all the measurements.

3.3 ICP-OES

Inductively Coupled Plasma Optical Emission Spectroscopy (ICP-OES) has been used to measure the amount of cations in the capture and recovery solutions after the process. ICP-OES is an analytical technique used for the detection of chemical elements. It consists on the measurement of the intensity and the wavelength of electromagnetic radiations emitted by atoms in the excited state, caused by their contact with inductively coupled plasma. The high density and temperature plasma is generated by the ionization of argon gas subjected to an electromagnetic field, created by high frequency current. The solution sample is delivered into a nebulizer, where it is converted into a mist, and then it is introduced into the plasma flame. The collision of the specie with the electrons and the charged ions of the plasma causes their excitement to a high energy state. Once excited, the atoms return to low energy level, emitting electromagnetic radiations. The wavelength of the radiation is characteristic of each chemical specie. The content of the atoms is instead determined by the radiation intensity.

Chapter 4

Thermodynamics of Materials

This Chapter is dedicated to the study of the active materials used for lithium recovery process.

In the first Section, the most accredited intercalation mechanism of lithium cations in LiMn_2O_4 is reported. Based on it, a simple thermodynamic model is developed to simulate the equilibrium potential profile of LiMn_2O_4 , which is applied in the complete model of the reactor reported in Chapter 5.

The second Section reports an investigation of the thermodynamic behavior of Nickel Hexacyanoferrate in single cationic and two cationic species solution. The results of this study are relevant for NiHCF application in ion pumping technology with mixed cations species. All the content of this Section has been previously published [48].

4.1 Lithium capturing electrode - Lithium Manganese Oxide

Lithium Manganese Oxide (LiMn_2O_4) is one of the most used cathode materials for lithium ion batteries because of its high energy density, low cost and low toxicity. It has a spinel structure, where the Li ions occupy the tetrahedral sites (8a) and the Mn ions occupy the octahedral site (16d). The scheme of this structure is reported in Fig. 4.1. The behavior of lithium intercalation in the lattice has been hugely studied in the past [66, 67, 68].

The typical equilibrium potential curve of LMO is shown in Fig. 4.2. The curve is represented vs. x , the molar fraction of Li^+ in the solid. The curve is calculated by averaging between the reduction and oxidation branches of a GCPL measurement of LMO in 10 mM of LiCl and 100 mM of NaCl performed at 0.05 C rate. The curve shows two inflection points that are correlated to the lithium intercalation mechanism. During the

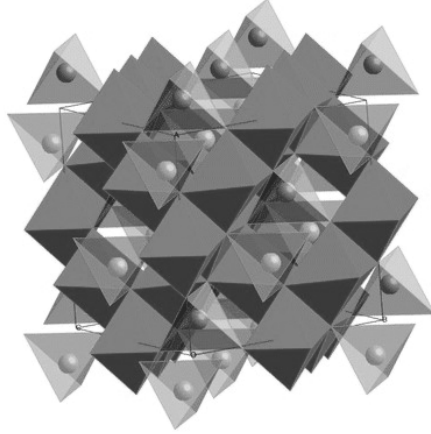


Figure 4.1: The cubic crystal structure of LMO, with lithium ions depicted as a sphere. The oxide ions form a cubic close packing with the manganese in the octahedral sites (dark grey) and the lithium inserted in the tetrahedral sites (light grey) [69].

discharge, the Li^+ cations intercalate inside the tetrahedral sites of the lattice, according to the following reaction:



The most accredited explanation of the shape of discharge curve was given by Liu and others [69]. From the fully charged state at $x=0$, the lithium starts to intercalate into the $\lambda\text{-MnO}_2$, to form a lithium-poor phase A, until $x=0.1$. Hereafter, the intercalation continues forming a second lithium-rich phase B. In this region, the chemical potential of the lithium in the two phases does not change with the concentration, leading to a flat plateau at a potential of 0.7 V vs. E_{RLE} , that indicates the coexistence of the two phases. At $x=0.35$, the end of the first plateau occurs and the phase A is totally converted in the phase B. In this region the potential starts to drop, indicating a change in the lattice parameter and the formation of a different solid solution C. When half of the lithium sites 8a are filled ($x=0.5$), the drop in the potential with the concentration becomes smoother, thus indicating the starting of lithium intercalation in the solid solution C, giving rise to the second equilibrium [69].

In other words, the process can be simplified in two steps: on the first plateau, lithium cations intercalate in $\lambda\text{-MnO}_2$, filling half of the available tetrahedral sites. This transformation is a two phases equilibrium that leads to the formation of the lithium-rich phase B. Hereafter, the potential decreases and another phase C is formed, where the lithium intercalation continues, leading to the filling of the remained available tetrahedral sites.

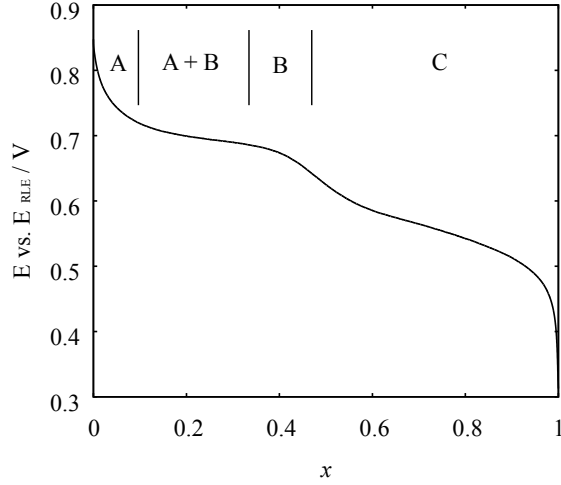


Figure 4.2: Typical equilibrium potential curve of LiMn_2O_4 vs. the molar fraction of Li, extracted from GCPL measurement performed at 0.05 C-rate in 10 mM LiCl and 100 mM NaCl, with the various phases of intercalation reported [69].

4.1.1 Thermodynamic model

According to the description of the intercalation mechanism of Li^+ in LMO structure, a simplified thermodynamic model to describe the shape of the equilibrium curve shown in Fig. 4.2 was developed. This model will be implemented for modelling the complete cell behavior during the capturing step (see Section 5.2).

In the model LMO structure is assumed to be formed by two different solid solutions that have two kinds of intercalation sites, named x_1 e x_2 . The reactions that occurs during the discharge can be described as follows:



where the first equation represents the intercalation of Li^+ in O_1 , the empty (oxidized) sites of the first solid solution, which leads to the formation of $\text{Li}_{0.5}\text{Mn}_2\text{O}_4$; the second reaction represents the intercalation of Li^+ in O_2 , the empty (oxidized) sites of the second solid solution, to form LiMn_2O_4 . R_1 and R_2 represents the occupied (reduced) sites of the two solid solutions, e^- the electron, Li^+ the lithium cation. It is worth to underline that the two reactions are not consecutive ($\text{R}_1 \neq \text{O}_2$). Indeed R_1 represents the occupied sites by lithium during the phase transition; while O_2 represents the empty sites that start to be filled once that the solid solution C is formed, at the end of the first plateau. C_{T_1} and

C_{T_2} are defined as the total concentration of active sites in the first and the second solid solution respectively, C_{s_1} and C_{s_2} as the concentration of filled states. Defining $x_1 = \frac{C_{s_1}}{C_{T_1}}$ and $x_2 = \frac{C_{s_2}}{C_{T_2}}$ as fraction of filled states for the two solid solutions, equilibrium potentials for the two reactions can be written as:

$$E_1 = E_1^0 - \frac{RT}{F} \log \frac{x_1}{1-x_1} + \frac{RT}{F} \ln \frac{C_{Li}}{C_0} \quad (4.4)$$

$$E_2 = E_2^0 - \frac{RT}{F} \log \frac{x_2}{1-x_2} + \frac{RT}{F} \ln \frac{C_{Li}}{C_0} \quad (4.5)$$

where E_1 and E_2 are the two equilibrium potentials of the reactions and E_1^0 and E_2^0 are the standard potentials.

The equilibrium curve of Fig. 4.2 is the electrode potential, which results from both equilibrium reactions occurring at the same interface. Imposing therefore E_1 equal to E_2 , one obtains:

$$\frac{x_1}{1-x_1} = \frac{x_2}{1-x_2} e^{\frac{F(E_1^0 - E_2^0)}{RT}} \quad (4.6)$$

A total fraction of sites x can be defined as:

$$x = \frac{C_{s_1} + C_{s_2}}{C_{T_1} + C_{T_2}} \quad (4.7)$$

which can be rewritten using the definitions of x_1 and x_2 as:

$$x(C_{T_1} + C_{T_2}) = x_1 C_{T_1} + x_2 C_{T_2} \quad (4.8)$$

Evaluating x_1 from Eq. 4.8 and substituting in Eq. 4.6, a second degree equation in x_2 is obtained. Choosing the solution that gives a positive number, the follow expression for x_2 is obtained:

$$x_2 = \frac{((bx - a - \beta) + \sqrt{((bx - a - \beta)^2 + 4abx}))}{(2a(\beta - 1))}; \quad (4.9)$$

where $a = \frac{C_{T_1}}{C_{T_2}}$, $\beta = e^{\frac{F(E_1^0 - E_2^0)}{RT}}$ and $b = (1 + a)(\beta - 1)$.

From Eq. 4.9 and Eq. 4.5, the potential equilibrium as a function of x is obtained.

The calculated curve is represented in Fig. 4.3 (black squares), together with the LMO experimental equilibrium curve (red line). Both curves are reported vs. the potential of E_{RLE} . Values of a and β that give a similar shape to the experimental curve were chosen. As expected, the two curves differ on the first inflection point. In this region a two phase transformation occurs which leads to a flat potential. This effect is not included in the model. Globally, the theoretical curve matches fairly well with experimental curve and can be implemented to qualitatively describe the intercalation mechanism in two solid solutions.

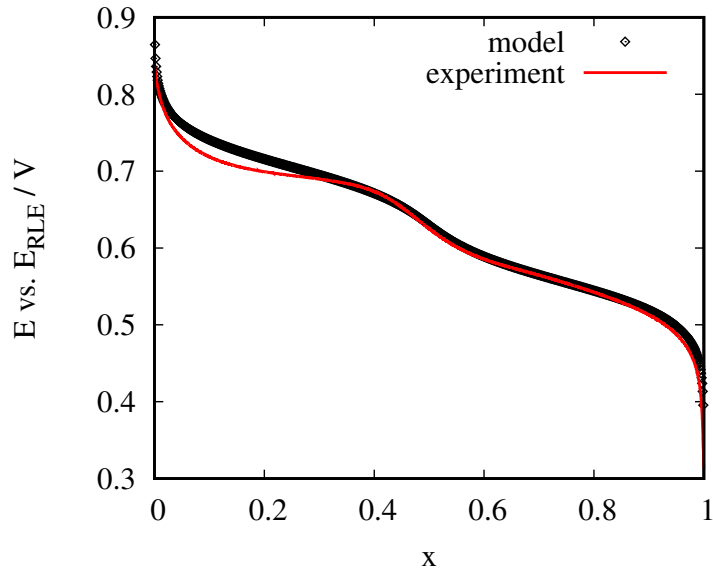


Figure 4.3: LMO equilibrium potential vs. Li molar fraction evaluated from Eq. 4.5 at $a=1$, $\beta=345.3$ (black squares) and experimental equilibrium curve (red line).

4.2 Lithium excluding electrode - Nickel Hexacyanoferrate

NiHCF is a material that belongs to the Prussian Blue family, which has recently raised attention in battery field [39, 70, 71]. Its formula is $A_n\text{Ni}(\text{CN})_6$, where A represents the intercalated cation. The crystal structure of NiHCF is shown in Fig. 4.4. The cubic crystallographic cell can be divided into four equal cubic sub-cells. The sub-cells are formed by $\text{Fe}^{\text{II/III}}$ and Ni^{II} ions at the corners and by the CN groups at edges. Hence each Ni^{II} is coordinated with six N and each $\text{Fe}^{\text{II/III}}$ with six C atoms [72]. This structure is equal to Prussian Blue materials [73, 74, 75, 76], where Ni is substituted by Fe, or to other derivatives, for example copper hexacyanoferrate, where Ni is replaced by Cu [39, 77]. Each sub-cell of the crystallographic structure is an interstitial site, where a cation can be hosted. Their intercalation occurs during reduction of Fe from 3 to 2. Thanks to the rigid structure, it occurs without distortion of the framework.

Its “open” framework, formed by larger interstitial sites, leads to a fast charging/discharging rate. Moreover, NiHCF has a good charge retention, low cost and low toxicity [78]. All these features make it a very interesting material in battery field application, despite its low charge density (ideally 86 mAh/g).

Intercalation in NiHCF, and in general in Prussians blue, is not selective: intercalation

of various cations are reported in literature such as lithium, sodium, potassium, rubidium, caesium and ammonium [38, 40, 49, 70], at different potentials. This potential depends on the Gibbs free energy of intercalation and it is higher for ions thermodynamically more favored in the solid phase than in the liquid. Indeed, considering the follow equilibrium reaction:



where A^+ and B^+ are two cations in solution, its standard Gibbs free energy is equal to:

$$\Delta G^0 = -F (E_B^0 - E_A^0), \quad (4.11)$$

where E_A^0 and E_B^0 are the standard potential of intercalation of the cations. If $E_B^0 > E_A^0$, ΔG^0 is negative, which means that B^+ is more favored to stay in the NiHCF structure than A^+ .

Due to its non-selective intercalation, application of Prussian Blue derivatives in various technologies, such as water desalination [79] or energy production from salinity difference [80, 81, 82], has been investigated in the last decade.

NiHCF was selected as a lithium excluding electrode in ion-exchange technique due to the low intercalation potential of Li^+ in its structure [40], that makes intercalation of other alkaline cations more favored. Its unselective intercalation allows the use of various aqueous sources as recovery solution during the release of lithium such as sea-water or brine. Moreover, its intercalation potential is lower than other Prussian blue derivative, well inside stability window of water.

A deeper understanding of thermodynamic of NiHCF in cation mixtures is very important due to its possible applications. While the intercalation of a single cationic chemical species has been largely investigated, a study of mixed ion intercalation is still missing.

During this PhD work, a step forward into the understanding of the intercalation thermodynamics of mixed cations was achieved. In this Section, the study on intercalation into NiHCF from solution with one and two cationic species is reported. Furthermore, the experimental results are supported by a thermodynamic model that explains the observed behavior.

4.2.1 Intercalation in single-salt solutions

A prior study on intercalation in single-salt solution was performed, as a starting point for the understanding of the thermodynamic behavior in mixed solution.

The electrochemical measurements were carried out in the cell described in paragraph 3.2.3, using a three electrode set-up with of ca. 10 mg NiHCF as the working electrode, 40 mg of NiHCF as the counter electrode and Ag/AgCl (3M KCl) as the reference electrode. In this way the reaction occurring at the counter is the capture and release

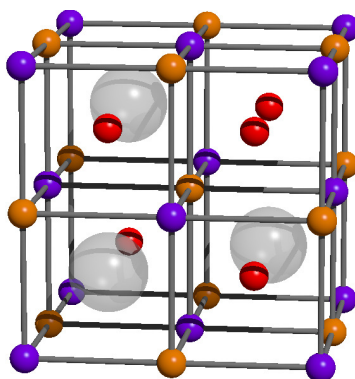


Figure 4.4: Structure of the crystallographic cell of nickel hexacyanoferrate. Orange and purple spheres represent the position of iron and nickel nuclei. Grey transparent spheres represent the empty interstitial sites. Red spheres represent intercalated cations, which can jump between interstitial sites. The sticks connecting the metal atoms represents the CN groups. Adapted from [48].

of cations as well, so that the electrolyte composition is not modified by production of other chemical species. The pH of the solution was decreased to 2 by adding nitric acid, to preserve the stability of the cyano bond [83]. The cell was bubbled with argon for 10 minutes before the start of each experiment to remove oxygen.

Since the goal of the work is to investigate the thermodynamic behavior of the system, an initial investigation of the conditions that most approaches to equilibrium was performed. In general, overpotential vanishes decreasing the current. Various GCPL measurements at different C-rates values were performed on NiHCF is $0.5 \text{ K}_2\text{SO}_4$ to find the optimal current that avoid large kinetic effects. The mean between oxidation and reduction branches of the potential vs. charge curve, E_t , is calculated and then dC vs. E_t is extracted at the various C-rates. The value of Q_{max} used is the maximum charge obtained experimentally at 1C. The results are shown in Fig. 4.5.

For higher value of C-rate, the curves are shifted along the E_t -axis, namely the overpotential is different between charge and discharge curves. That can be due to an asymmetry in the diffusion or charge transfer overpotential, while the resistance of the solution gives the same contribution during oxidation and reduction, since it depends by IR_l , which is equal in both current directions. The integrals of curves in Fig. 4.5 represent the charge passed into the system and they decrease with the C-rate. This effect is due to increase of diffusion overpotential in the solid, which leads to a lower filling of the material. Indeed, according to the literature, transport of cations inside the solid phase is the major overpotential for these kind of systems [84, 85]. The curve at 1C is similar to the one at

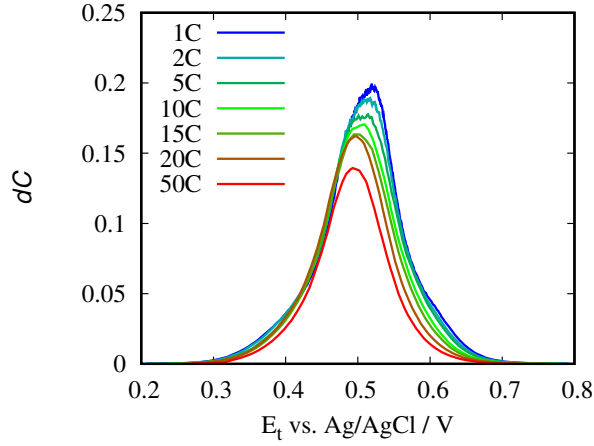


Figure 4.5: Average differential charge dC vs. potential E_t vs. Ag/AgCl 3 M, measured in K_2SO_4 0.5 M, at various C rates [48].

2C, therefore 1C rate is selected to perform the experiments. Lower C-rates than 1C are avoided to limit the effect of secondary reactions.

GCPL of NiHCF were performed in 0.5 M of K_2SO_4 , $(NH_4)_2SO_4$ and $NaSO_4$. The selected counter ion is SO_4^{2-} , because it is fairly inert during the reaction in solution. The correspondent dC curves are extracted and reported in Fig. 4.6. The peak position of dC curve indicates the potential at which most of the intercalation occurs.

In order to evaluate the peaks, the center of mass of the curves are calculated as:

$$\bar{E} = \frac{F}{RT} \int E dC(E) dE. \quad (4.12)$$

which, substituting the definition of dC of Eq. 2.29, becomes the average potential over x :

$$\bar{E} = \int_0^1 E(x) dx. \quad (4.13)$$

It is well assessed that the main contribution to the intercalation energy is due to the removal of the solvation shell of the cations [40, 86]. The smaller is the radius, the higher is the cation charge density and consequently the larger is its solvation shell. Intercalation of cations with higher radius is more favored. Values of \bar{E} obtained for intercalation of K^+ , Na^+ and NH_4^+ and ionic radii of each cation are shown in Table 4.1. It can be noted that intercalation potential decreases for smaller ionic radii.

The dC curve for NH_4^+ has an additional peak at ca. 630 mV vs. Ag/AgCl (3M KCl). The presence of this peak was already reported in literature for Prussian blue materials

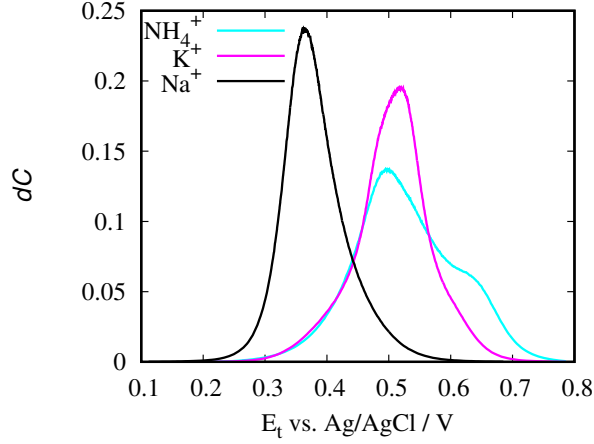


Figure 4.6: dC vs. potential E_t for single cation intercalation, K^+ , Na^+ and NH_4^+ , at 1C rate [48].

	\bar{E} [mV]	Ionic Radii [\AA]
NH_4^+	527	1.43
K^+	506	1.37
Na^+	381	1.25

Table 4.1: Mean potential of intercalation in NiHCF and ionic radii of NH_4^+ , K^+ and Na^+ .

at similar potential [87], although the reason of its formation is still not clear. Garcia et al. [87] attribute it to the formation of complex similar to M6hr's salt, composed by $(NH_4)_2SO_4$ in solution and the low spin Fe in NiHCF.

dC curves for various cations reported in Fig 4.6 show different shapes. This is due to the contribution of the “excess potential” introduced in Section 2.2, describing the interactions between redox species in the solid. This aspect is explained further in the next Paragraph.

4.2.2 Thermodynamic model in single salt solution

In Section 2.2 the expression of the equilibrium potential for the intercalation reaction has been derived:

$$E = E_A^0 + \frac{RT}{F} \ln \frac{C_A}{C_0} + \frac{RT}{F} \ln \frac{1-x}{x} + \frac{1}{F} \frac{\partial G_{exc}}{\partial x} \quad (4.14)$$

For $\frac{\partial G_{exc}}{\partial x_A} \rightarrow 0$, the potential expression represents the ideal condition, in which the interactions between redox species in the solid phase are neglected. The potential curve calculated in this condition from Eq. 4.14 is the black curve reported in Fig. 4.7 (a). The dC curve for the ideal case can be calculated from the inverse of the derivative of Eq. 4.14 with respect to x (dx/dE), for $\frac{\partial G_{exc}}{\partial x_A}=0$. The resulted curve is reported in black color in Fig. 4.7 (b). It has a bell-shaped curve, the half-peak width is equal to $3.5RT/F$ and the peak is perfectly symmetric.

The shape of experimental dC curves differs from the ideal shape. This is likely due to the interaction between the redox species in the lattice, represented by the term G_{exc} .

An expression for G_{exc} has been proposed by McCargar and others [49], for intercalation from single-salt solution in a Prussian Blue material. Specifically, they took into account the interactions between nearest-neighbouring sites in a simple lattice model. For a single cation intercalation, nearest-neighboring sites can be empty, both occupied by the cation and one empty and one occupied. To each couple, an interaction energy can be attributed, namely ε_{ee} , ε_{oo} , ε_{eo} respectively. The interaction term is a function of interactions of all couples.

Then the excess free energy of the solution is calculated using the regular solution approximation [88]. This approximation considers the entropic part of the excess free energy of a solution equal to 0. In other words, it assumes the entropy of the solution to be equal to the one of an ideal solution with the same composition, namely with random mixing without specific interaction. Hence, the excess free energy is equal to the excess enthalpy, which is defined as:

$$H^{ex}(x_A) = wx_A(1 - x_A) \quad (4.15)$$

where w is the interaction term, depending on the interaction energies ε_{ee} , ε_{oo} , ε_{eo} .

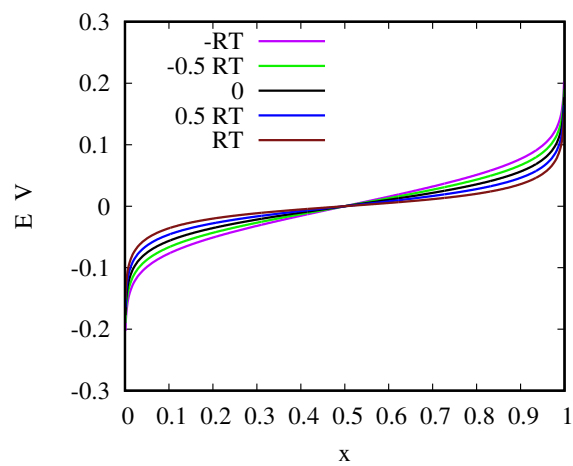
This term is included in the model by substituting $H^{ex}(x_A)$ in Eq. 4.14 [49]:

$$E = E^0 - \frac{RT}{F} \ln \frac{x_A}{1 - x_A} + \frac{RT}{F} \ln \frac{C_A}{C_0} - \frac{w}{F} (1 - 2x_A). \quad (4.16)$$

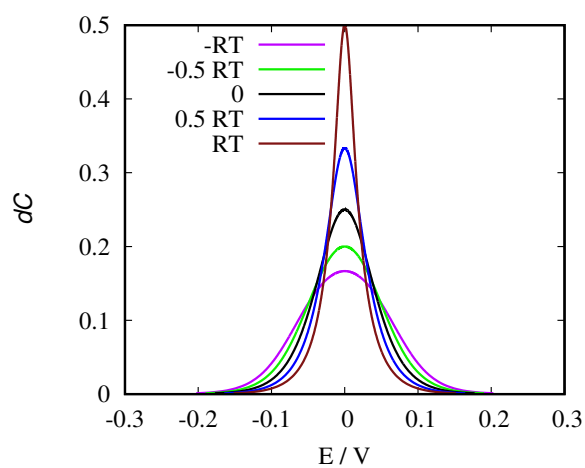
Potential profile and dC curves evaluated from Eq. 4.16 at different values of w are reported in Fig. 4.7 (panel (a) and (b) respectively). E^0 is arbitrary taken equal to 0, as well as $C_A=C_0=1$ M. The term w changes the width of the curve: for positive values the width decreases, for negative it increases. The position of peaks instead are not altered by w values: the presented model describes the change of the width, while does not describe possible asymmetries of the curve.

The average potential \bar{E} , as defined in Eq. 4.13, can be calculated from Eq. 4.14:

$$\bar{E} = E_A^0 + \frac{RT}{F} \ln \frac{C_A}{C_0}. \quad (4.17)$$



(a)



(b)

Figure 4.7: Galvanostatic cycling (a) and differential charge (b) calculated by Eq. 4.16 for various values of two-points interactions between particles w . For $w=0$ (black lines) the interaction are neglected and the curves are ideal [48].

This equation is based on the property of excess free energy of pure states: $G^{ex}(x_A = 0) = G^{ex}(x_A = 1) = 0$. When the dC curves are symmetric, \bar{E} corresponds to the peak potential. This is always true for the ideal model and for regular solution approximation.

The w value for NiHCF in pure solutions of Na_2SO_4 , K_2SO_4 and $(\text{NH}_4)_2\text{SO}_4$ were estimated by fitting the data of the dC curve with Eq. 4.16. The fitting works fairly well for the curves of K^+ and NH_4^+ (which are symmetric), the curve of Na^+ shows a slight asymmetry which is not predicted by the model. The obtained values are -0.09, -0.42 and -1.3 Wh/mol (-0.32, -1.5, -4.7 KJ/mol) for Na^+ , K^+ and NH_4^+ respectively. The value of w decreases for higher ionic radii, as reported by McCargar et al. for intercalation of various cations in iron hexacyanoferrate [49]. The calculated interaction energy values are less than 1% of the total thermodynamic energy of intercalation, that can be estimated as $\bar{E}F$ [49], equal to 10.2, 13.5 and 14 Wh/mol for NH_4^+ , K^+ and Na^+ respectively.

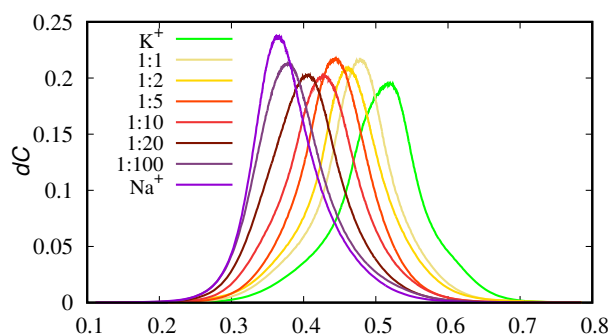
4.2.3 Intercalation in mixed solutions

GCPL measurements of NiHCF in two cationic species solutions were performed, at various cations ratio in solution, namely 1:1, 1:2, 1:5, 1:10, 1:20, 1:100, keeping the total concentration constant at 0.5 M, for the couples K^+ and NH_4^+ , K^+ and Na^+ and Na^+ and NH_4^+ . The dC curves are extracted and reported in Fig. 4.8.

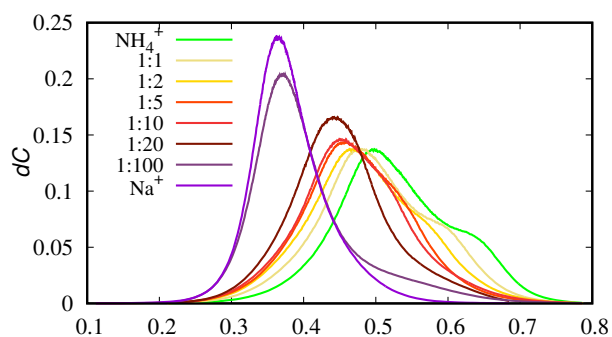
Intercalation of two cations from a two salts solutions does not occur at two different potentials. Instead, dC curves show a single peak. The curve moves in the E axis from the intercalation potential of one cation to the one of the other. \bar{E} for dC curves vs. relative concentration ($\frac{C_A}{C_A+C_B}$) are reported in Fig 4.9. The index A refers to the cation with higher intercalation potential in the couple. For K^+ and NH_4^+ , that have similar intercalation potential, the variation with the ratio in solution is small and linear. For the other two couples instead the variation is large and it has a quasi-logarithmic scale. This behavior is very interesting for applications of NiHCF intercalation in cations mixture, since the energy required for the process and the voltage cell depend on the intercalation potential. This can be explained through a mathematical model, reported in the next paragraph.

4.2.4 Model in a mixture of two cations

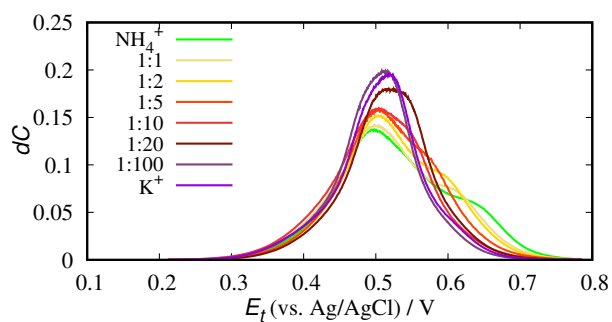
The previous calculations can be extended to solutions in which two species of cations, A^+ and B^+ , are present. Using the same procedure for deriving Eq. 4.14 for the two equilibriums occurring at the interface, the follow equations can be obtained:



(a)



(b)



(c)

Figure 4.8: Differential charge dC vs. potential E measured in mixtures cations solution at various ratios. Panel a: K^+ and Na^+ . Panel b: NH_4^+ and Na^+ . Panel c: NH_4^+ and K [48].

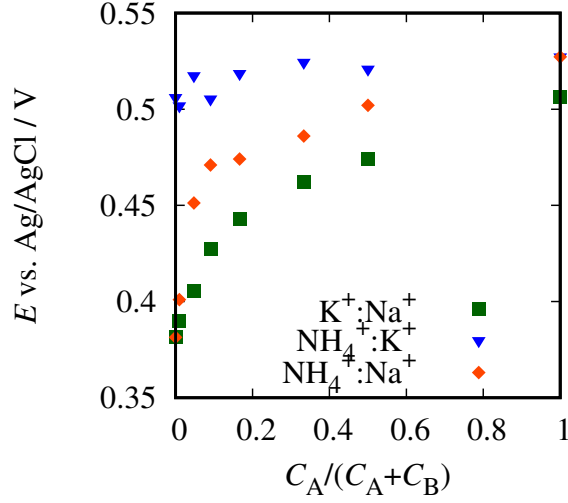


Figure 4.9: \bar{E} of the differential charge dC curve vs. relative concentration $C_A/(C_A+C_B)$ of the two cations in solution for the NH_4^+/K^+ , $\text{NH}_4^+/\text{Na}^+$ and K^+/Na^+ couples. The index A indicates the cations with higher potential in the couple [48].

$$E = E_A^0 + \frac{RT}{F} \ln \frac{C_A}{C_0} - \frac{RT}{F} \ln \frac{x_A}{1 - x_A - x_B} - \frac{1}{F} \frac{\partial}{\partial x_A} G^{ex}(x_A, x_B) \quad (4.18)$$

$$E = E_B^0 + \frac{RT}{F} \ln \frac{C_B}{C_0} - \frac{RT}{F} \ln \frac{x_B}{1 - x_A - x_B} - \frac{1}{F} \frac{\partial}{\partial x_B} G^{ex}(x_A, x_B), \quad (4.19)$$

where x_A and x_B are the molar fractions of sites occupied by cations A^+ and B^+ respectively. The term $G^{ex}(x_A, x_B)$ accounts possible interactions between the redox species in the lattice. The activity coefficients of the cations $\gamma_{R,A}$, $\gamma_{R,B}$ and of the empty sites γ_O can be extracted from the excess free energy:

$$\frac{\partial}{\partial x_A} G^{ex}(x_A, x_B) = RT \ln \frac{\gamma_{R,A}}{\gamma_O} \quad (4.20)$$

$$\frac{\partial}{\partial x_B} G^{ex}(x_A, x_B) = RT \ln \frac{\gamma_{R,B}}{\gamma_O}. \quad (4.21)$$

Equating the expressions of electrode potential E (Eqs. 4.18 and 4.19) one obtains:

$$\frac{\gamma_{R,A}x_A}{\gamma_{R,B}x_B} = \frac{C_A}{C_B} e^{-\frac{F}{RT}(E_B^0 - E_A^0)}, \quad (4.22)$$

The final expression of the potential can be found defining the total fraction of charge $x = x_A + x_B$ (that directly depends on the charge) and deriving x_A and x_B as a function of x through Eq. 4.22. Substituting x_A and x_B in Eq. 4.18, one obtains:

$$E = E_{A/B}^0 + \frac{RT}{F} \ln \frac{C_A + C_B}{C_0} - \frac{RT}{F} \ln \frac{x}{1-x} - \frac{1}{F} \frac{\partial}{\partial x} G'^{ex}(x), \quad (4.23)$$

where $E_{A/B}^0$ is defined as the standard potential for intercalation from two salts solution:

$$e^{\frac{F}{RT}E_{A,B}^0} = \frac{C_A e^{\frac{F}{RT}E_A^0} + C_B e^{\frac{F}{RT}E_B^0}}{C_A + C_B}, \quad (4.24)$$

All the activity coefficients can be grouped together, defining the function $G'^{ex}(x)$:

$$\frac{\partial}{\partial x} G'^{ex}(x) = RT \ln \frac{\frac{C_A}{C_0} e^{\frac{FE_A^0}{RT}} + \frac{C_B}{C_0} e^{\frac{FE_B^0}{RT}}}{\frac{C_A \gamma_{0,A}}{C_0 \gamma_{R,A}} e^{\frac{FE_A^0}{RT}} + \frac{C_B \gamma_{0,B}}{C_0 \gamma_{R,B}} e^{\frac{FE_B^0}{RT}}}.$$

A complete evaluation of the excess free energy for mixed cation intercalation has been developed in the work published by Erinwingbovo et. al [48]. In particular, we have shown that the experimentally accessible function $G'^{ex}(x)$ is an approximation of the excess free energy of the system $G^{ex}[x_A(x), x_B(x)]$. The entire demonstration is not reported here, because it is out of the scope of this PhD thesis.

For vanishing interaction ($G'^{ex} \rightarrow 0$), Eq. 4.23 has exactly the same shape of potential for single cation intercalation: this explains the presence of a single inflection point in the galvanostatic cycling and of a single peak in the dC curve consequently.

The average potential \bar{E} is calculated as follows:

$$\bar{E} = E_{A/B}^0 + \frac{RT}{F} \ln \frac{C_A + C_B}{C_0} - \frac{1}{F} G'^{ex}(x=1). \quad (4.25)$$

In this case, the term $G'^{ex}(x=1)$ is not equal to 0, since it is an approximation of the excess free energy for $x_A + x_B = 1$. Excess free energy is equal to 0 by definition only for the pure states, i.e. $x_A = 1$ or $x_B = 1$.

Neglecting the term $G'^{ex}(x=1)$, Eq. 4.25 is used to evaluate the \bar{E} for cation mixtures. Results are shown in Fig. 4.10, together with the experimental results.

The \bar{E} calculated shows a good agreement with the experimental values. For the couple K^+ and NH_4^+ that have similar average potential in single salt solution, the change of the average potential for the two salts solution is small and linear with the relative concentration. For the other two couples, namely K^+ and Na^+ and NH_4^+ and Na^+ , the average potential moves clearly for one extreme to the other. For equimolar solution ($\frac{C_A}{C_A+C_B}=0.5$), the average potential is similar to the one of the more favored

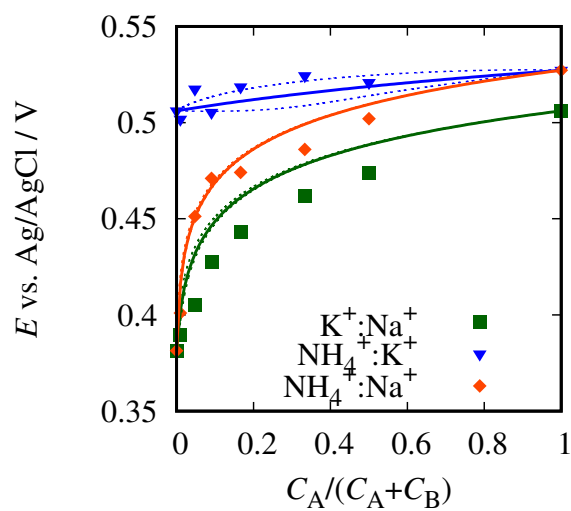


Figure 4.10: Experimental (points) and calculated values (line) of \bar{E} vs. relative concentration $C_A/(C_A + C_B)$ of the two cations in solution for the NH_4^+/K^+ , $\text{NH}_4^+/\text{Na}^+$ and K^+/Na^+ couples. The solid lines refer to the ideal model ($w_{AB}=0$); the dotted lines to the model with two-points interactions, with w_{AB} equal to RT and $-RT$ [48].

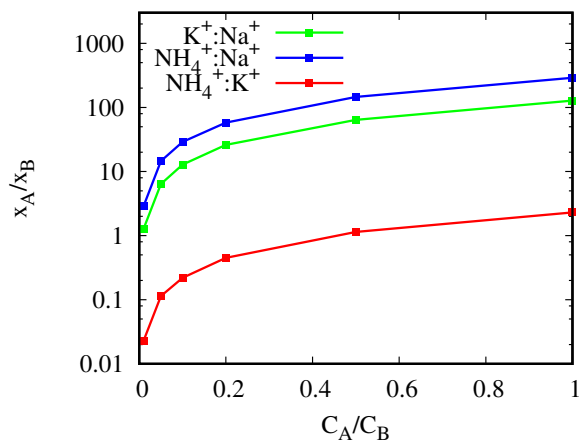


Figure 4.11: Ideal molar fraction ratio of cations in solid vs. concentration ratio in liquid, evaluated by Eq. 4.26.

cation (K^+ and NH_4^+). Only by decreasing its relative concentration down to 0.01, the average potential approaches the one of the less favored cation.

The behavior is explainable looking to Eq. 4.22, that relates the fraction of intercalated cation x_A/x_B with the concentration ratio in solution. For the ideal case ($\gamma_{R,A} = \gamma_{R,B} = 1$) the equation becomes:

$$\frac{x_A^{id}}{x_B^{id}} = \frac{C_A}{C_B} e^{-\frac{F}{RT}(E_B^0 - E_A^0)}. \quad (4.26)$$

The higher is E_A^0 respect to E_B^0 , the bigger is the ratio x_A^{id}/x_B^{id} respect to C_A/C_B . Fractions x_A/x_B for various C_A/C_B calculated by Eq. 4.26 are reported in Fig. 4.11. For the cations couples K^+/Na^+ and Na^+/NH_4^+ , at equimolar concentration ($C_A/C_B = 1$), the more intercalated cation is the more favored (K^+ or NH_4^+). By decreasing the concentration of the more favored cation, the ratio slowly decrease. Only at the ratio $C_A/C_B = 1/100$ the cations are almost equally intercalated. For the couple NH_4^+ and K^+ , which have similar intercalation potentials, $x_A/x_B \approx C_A/C_B$.

The evaluation of x_A/x_B explains also why the dC curve shows only one peak. For 1:1 concentration ratio in solution, the more favored cation is mostly intercalated in the solid, therefore only its peak is visible. At lower ratio, its concentration decreases and the average potential is shifted towards lower values with a Nerstian dependence. The concentration of the less thermodynamically favored cation keeps instead approximatively constant, so that the two peaks overlap. This is certainly valid at the extremes: for the couple K^+ and Na^+ at 1:100 ratio the average potential of K^+ lowers by 118 mV, practically equal to the average potential of Na^+ .

It is worth to include in the evaluation of the intercalation potential in mixed solutions an excess free energy evaluated through the regular solution approximation, to check if it gives a large contribution to the total average potential of mixed intercalation.

The calculation of G_{ex} reported previously using the regular solution approximation is extended for the case of intercalation from mixed-ion solutions. The excess enthalpy becomes:

$$H^{ex}(x_A, x_B) = w_A x_A (1 - x) + w_B x_B (1 - x) + w_{AB} x_A x_B, \quad (4.27)$$

where w_A and w_B correspond to the interaction energy w for single cation intercalation extracted from the experiments in single salt solution, while w_{AB} corresponds to the energy coming from interaction between two cationic species intercalated in the solid.

Equations 4.18 and 4.19 become:

$$E = E_A^0 - \frac{RT}{F} \ln \frac{x_A}{1-x} + \frac{RT}{F} \ln \frac{C_A}{C_0} + \frac{1}{F} (w_A x_A + w_B x_B + w_A x - w_{AB} x_B - w_A) \quad (4.28)$$

$$E = E_B^0 - \frac{RT}{F} \ln \frac{x_B}{1-x} + \frac{RT}{F} \ln \frac{C_B}{C_0} + \frac{1}{F} (w_A x_A + w_B x_B + w_B x - w_{AB} x_A - w_B) \quad (4.29)$$

These equations were solved numerically in x_A and x_B , using the experimental potential and charge (E and x), at various values of w_{AB} ($-RT$, 0 and RT). The average potentials \bar{E} are calculated from Eq. 4.25 and reported in Fig. 4.10. \bar{E} does not change appreciably, by changing w_{AB} . Concluding, the introduction of the excess free energy using the regular solution approximation does not lead to any relevant changes in the proposed model for intercalation from two salts cations.

4.2.5 Conclusions

In this Section the thermodynamics of intercalation in NiHCF was discussed, for single and two salts solution. The experiments were supported by a thermodynamic model that can be generally used for battery-like material.

Intercalation in NiHCF from single cation solution was performed. A correlation between the intercalation potential and the radius of the cation was found, as already reported in literature [38, 40, 70]. Moreover, the interaction energies between redox species in the host structure were estimated through a regular solution approximation. They give a small contribution to the total energy of intercalation.

After that, intercalation in NiHCF from two salts solutions was performed. The dC curves have a bell shape, whose peak potential can be predicted by an ideal thermodynamic model. The model allows to predict the amount of intercalated cations in the host structure. An estimation of the excess free energy for the intercalation of two cationic species was included in the model through the regular solution approximation. The inclusion of excess free energy in the calculation does not influence the intercalation potential considerably, showing that the presented ideal model well describes the system.

It is important to point out that the results shown in this Section can be very relevant for application of NiHCF in a mixture of two cationic species.

Firstly, Eq. 4.26 allows to have a fairly good quantitative evaluation of the amount of the two cations intercalated in the solid. This can be relevant for future application of the NiHCF in electrochemical ion pumping techniques for solution purification, included lithium recovery. Indeed, during the release step, NiHCF captures cations from a cation mixture and therefore it participates actively on the achievement of the final purity of the

solution. The developed model can be therefore useful to predict the final concentrations of a certain recovery solution upon cycles if there are more than one cation that can be inserted in the NiHCF, during the exchange of lithium.

Furthermore, from Eq. 4.25 the intercalation potential from two salts solutions can be predicted. This can be useful to estimate the thermodynamic energy or voltage cell during charge or discharge for some applications of NiHCF in mixture cations electrolyte (batteries, water treatment, etc.), including ion-exchange for lithium recovery. The thermodynamic energy of intercalation in NiHCF can be a large contribution to the total electrical energy required by the process, as it will be further discussed in Chapter 6.

Chapter 5

Capturing from Diluted Lithium Brine

This Chapter is dedicated to the study of lithium capturing process from diluted brine.

All the experiments reported in this Chapter, unless otherwise specified, have been carried out using the cell described in paragraph 3.2.1, running GCPL measurements, with LMO as WE, NiHCF as CE and Ag/AgCl as RE. Since the focus is to investigate only the lithium capturing step in LMO from diluted solutions, the experiments are performed as follows: a negative constant current is applied, so that the LMO is reduced until the potential of 0.37 V vs E_{RLE} and lithium cations are intercalated in the solid, then the current is inverted and the lithium cations are released back in the same solution, until the potential of 0.96 V vs E_{RLE} . In the graphs of this Chapter, the galvanostatic curves of LMO are reported with increasing positive charge during the capture of lithium, which occurs on the reduction branch.

The performances of the process have been investigated at various flow rates by changing some parameters, such as brine concentration (Sect. 5.1 and 5.7), electrode mass loading (Sect. 5.3) and applied current (Sect. 5.4). An estimation of the pumping energy required during the capturing step is made in Sect. 5.6. Moreover, a mathematical model of the flow-through electrodes cell has been developed to simulate the experimental results (Sect. 5.2). Some of the content of this Chapter have been previously published [64].

5.1 Effect of the lithium ions concentration

The effect of lithium concentration on the capturing step was investigated, firstly running a GCPL in the conical cell described in paragraph 3.2.3 in “similar-Atacama” solution. In order to have a first overview on the magnitude of the lithium concentration effect, the

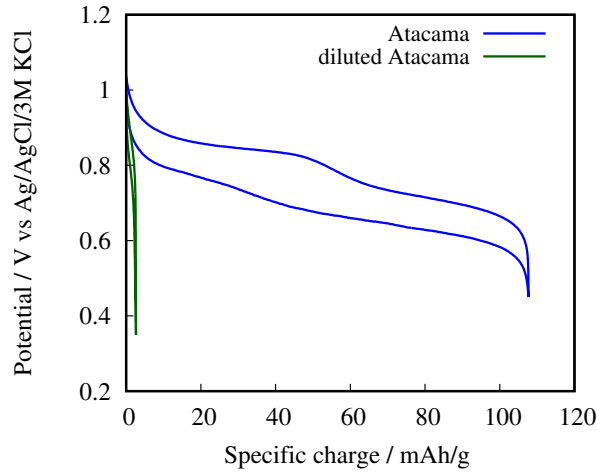


Figure 5.1: GCPL of LiMn_2O_4 in “similar-Atacama” solution and 10 times diluted “similar-Atacama” solution in the flooded cell without flow [64].

experiment was repeated in the same cell with a ten times diluted solution.

The galvanostatic curves are shown in Fig. 5.1. The charge is normalized by the mass of electrode. Both reduction (bottom curve) and oxidation (top curve) potential profiles in “similar-Atacama” solution have the classic shape of LMO [69].

As previously reported [6], the maximum reduction charge Q_f obtained in “similar-Atacama” solution (blue curve) is close to the theoretical capacity of LMO, c.a. 105 mAh/g. Repeating the experiment in the 10 times diluted similar-Atacama solution (green curve), where the concentration of LiCl is 4 mM, a value of Q_f equal to only 2.5 mAh/g is observed.

This huge difference in performances is due to the mass transport limitation, which increases by decreasing lithium concentration.

It is thus necessary to improve the transport of lithium by advection. Therefore, the same experiments were repeated in the flow-through electrodes cell described in Sect. 3.2.1, whose scheme is reported in Fig. 3.1. The discharge and charge curves of LMO, obtained in “similar-Atacama” solution and in the ten times diluted solution, are reported in Fig. 5.2, panel (a) and (b) respectively. Each curve is obtained pumping the electrolyte at a different flow rates.

The curves obtained in “similar-Atacama” solution in the flow-through electrodes cell at values of flow other than 0 are practically equal to the curve obtained in the flooded cell. On the other side the curve obtained without pumping (Fig. 5.2 (a), black curve) reaches much lower value of Q_f . That can be explained by estimating the volume of the flow-through electrodes cell. Considering the thickness of electrodes stack ($930 \mu\text{m}$

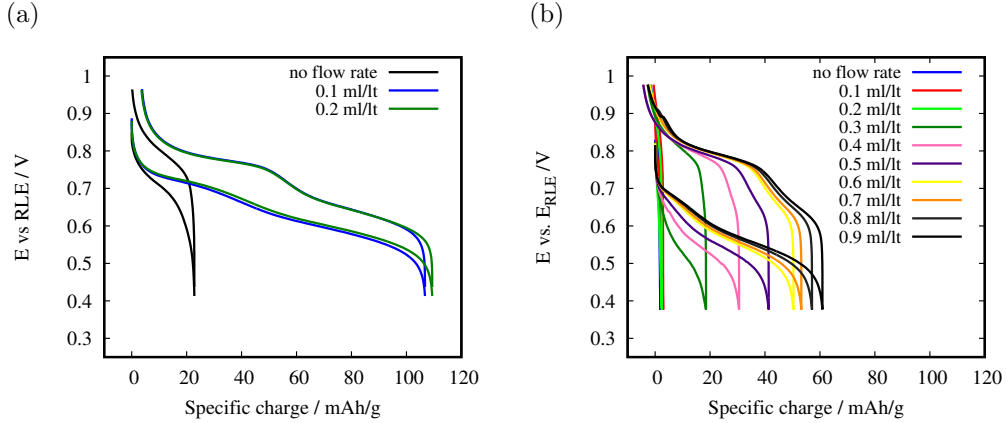


Figure 5.2: GCPL of LiMn_2O_4 in “similar-Atacama” solution and the diluted “similar-Atacama” solution at various electrolyte flow rates (0-0.2 ml/min and 0-0.9 ml/min respectively, in steps of 0.1 ml/min). The experiments are performed in the flow-through electrodes cell described in paragraph 3.2.1 [64].

including WE, CE and separator) and the geometrical area (c.a. 1.2 cm^2), the liquid volume in the cell is circa $114 \mu\text{L}$. Hence, the total amount of lithium inside the cell is $4.6 \mu\text{mols}$. Considering the mass of the active material (6 mg for the electrode used in the experiment), the specific charge of 20 mAh/g reached without flow corresponds to capturing $4.5 \mu\text{mols}$ of lithium, matching almost perfectly with the amount present in the cell. Hence, in absence of flow, the lithium capturing from “simil-Atacama” solution is limited by the amount of lithium ions in the cell. This limitation does not occur in the flooded cell, as the total volume used is 50 ml.

When the diluted “similar-Atacama” solution is used (Fig. 5.2, (b)), the curves measured at different flow rates differ in the reduction parts, thus indicating that the flow rate has an influence on the capturing of the lithium ions. On the other side the oxidation parts are very similar: they occur at the same potential and the first plateau fits almost perfectly for all the curves. A clear positive influence of the electrolyte flow rate on Q_f can be appreciated, thus confirming the importance of diffusive ion transport in the liquid.

In order to have a better view of the dependence of the maximum charge on the electrolyte flow rate, Q_f values vs. the volumetric flow rate Γ are reported in Fig. 5.3, for all the experiments performed in the two solutions. The values of Q_f are normalized by a “reference charge” Q_r , that is the maximum charge of the electrode, measured in “similar-Atacama” solution at the minimum available flow rate (0.1 ml/min). The ratio Q_f/Q_r represents the amount of solid that participates to the intercalation reaction, namely the

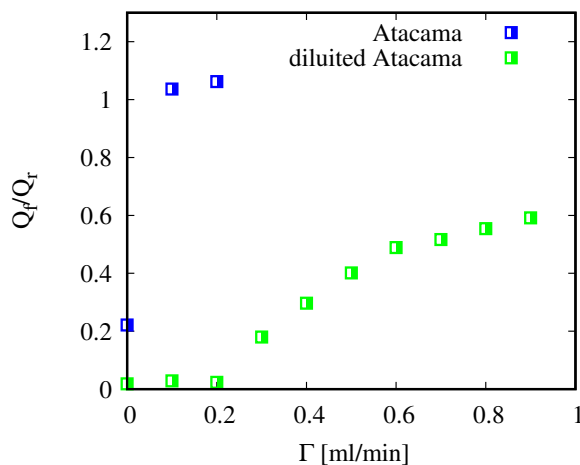


Figure 5.3: Maximum reduction charge Q_f of LiMn_2O_4 normalized by the reference charge Q_r vs. the volumetric flow rate of the electrolyte in “similar-Atacama” and 10 times diluted “similar-Atacama” solution [64].

fraction of the active material filled by lithium: the higher is Q_f/Q_r , the higher is the capture efficiency. Q_r was measured for each electrode prior to its use in the flow-through electrodes cell and every 10 capturing cycles, so that the degradation upon cycles of the LMO electrode was monitored.

The data representation as in Fig. 5.3 shows that in the ten times diluted solution, Q_f/Q_r is almost equal to zero for flow rates less than 0.2 ml/min. Then it starts to increase linearly until c.a. 1 ml/min, where it reaches a limit value of circa 0.6. Instead, the curve obtained in “similar-Atacama” solution reaches values of circa 1 for flow rates other than 0. Both flow rates and lithium concentration have a huge influence on the lithium capturing efficiency.

In order to investigate more on this effect, the same experiments in solutions with different concentrations of LiCl (1 mM, 2 mM, 5 mM, 10 mM) and 100 mM of NaCl have been performed. Na^+ was chosen as second cation in solution, since it is usually the most present cation in Li^+ brines. Na^+ concentration has been chosen so that the solution has a ratio Li/Na similar to the geothermal waters [89], which are brine sources relatively spread in Europe. The effect of the presence of other cations on Li^+ intercalation on LMO has already been studied [6].

The galvanostatic curves obtained at different flow rates are reported in Fig. 5.4, in panel (a) for 1 mM, (b) for 2 mM, (c) for 5 mM and (d) for 10 mM.

As expected, the flow rate has a large influence on lithium capture; indeed Q_f increases with the flow rate at each concentration until a maximum value. The flow rate values

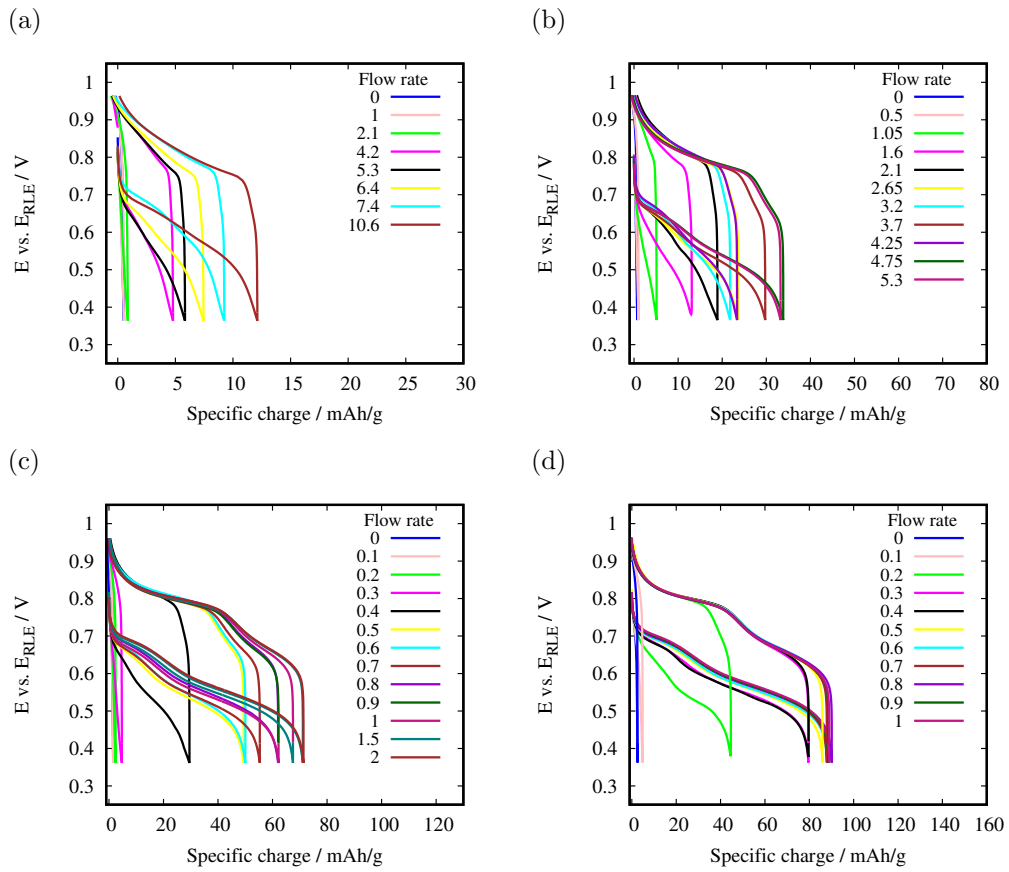


Figure 5.4: Galvanostatic curves of LiMn_2O_4 obtained in 1, 2, 5 and 10 mM LiCl and 0.1 M of NaCl (panel (a), (b),(c) and (d) respectively) at 1 mA and different flow rates. The value of the flow rate is indicated in the legend in ml/min [64].

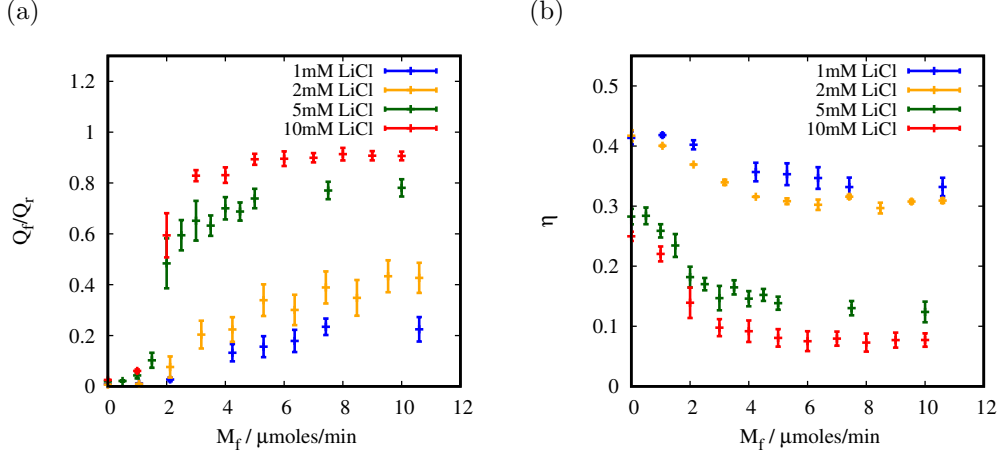


Figure 5.5: Panel (a): maximum filling (Q_f/Q_r) of LiMn_2O_4 ; panel (b): mean overpotential $\bar{\eta}$; both quantities are reported vs. the molar flow rate of the electrolyte at various concentrations of LiCl [64].

influencing the charge are in different ranges for each concentration, namely they are smaller by increasing the concentration. The more diluted is the lithium source, the higher is the volumetric flow rate that must be applied to obtain the maximum filling of material.

The Q_f/Q_r values vs. flow rate of the electrolyte in the cell are shown Fig. 5.5. The experiments have been repeated three times with three different electrodes and the error bar of the experiments is reported. In order to highlight the concentration effect, the curves are reported vs. the molar flow rate, evaluated multiplying the volumetric flow rate for the lithium solution concentration:

$$M_f = \Gamma C_{\text{Li}^+}; \quad (5.1)$$

The applied current during the experiment is 1 mA, that carries a charge equal to 60 mC/min, which on turn corresponds to a capturing rate of circa 0.6 $\mu\text{mol}/\text{min}$. Hence, for molar flow rates lower than this value, the limiting factor of the process is the amount of lithium pumped in the cell. This effect results in a increase of Q_f/Q_r less than linear, for $M_f < 1 \mu\text{mol}/\text{min}$. For $M_f > 1 \mu\text{mol}/\text{min}$, Q_f/Q_r increases instead linearly, thus indicating the positive effect of the flow on the capture. For $M_f > 5\text{-}6 \mu\text{mol}/\text{min}$, Q_f/Q_r reaches a saturation values much different for each concentration (0.2, 0.4, 0.75, 0.9 at 1, 2, 5 and 10 mM respectively). That suggests the presence of some limitations to the complete solid filling related to the concentration.

By reporting the Q_f/Q_r curves vs. M_f , it can be noted that the values of molar

flow rates at which Q_f/Q_r reaches its saturation (hereafter called “saturation molar flow rate”, M_s) are very similar for all the concentrations.

A more precise estimation of the saturation flow rate can be performed fitting the curve with a function of the type $a(1-\exp(-bx))$ and choosing M_s equal to $3/b$, which corresponds to the 95% of the saturation point. The found values are 10.4, 5.4, 3.6 and 3.2 $\mu\text{mol}/\text{min}$ for 1, 2, 5 and 10 mM. M_s values increase by decreasing the concentration, but less than the respective volumetric saturation flow rates (10.4, 2.7, 0.72, 0.32 ml/min). It can be concluded that the amount of lithium flowing through the reactor is an important parameter of the process, as its optimal value is similar for all the concentrations.

In Fig. 5.5 panel (b), the mean overpotential of the process vs. the flow rate for each concentration is reported, extracted from the galvanostatic curves as follows:

$$\bar{\eta} = \frac{1}{Q_f} \int_0^{Q_f} |E_{red}(Q) - E_{eq}(Q)| dQ. \quad (5.2)$$

where E_{red} is the potential of the reduction branch of the cycle, Q is the charge and E_{eq} is the equilibrium potential, obtained experimentally as already reported in Sect. 4.1 (Fig. 4.2). The overpotential follows an equal and opposite trend of Q_f/Q_r : it keeps almost constant at low M_f (0-1 $\mu\text{mol}/\text{min}$), it starts to linearly decrease for $M_f > 1$ $\mu\text{mol}/\text{min}$, until it reaches a saturation value for $M_f > 5-6$ $\mu\text{mol}/\text{min}$. The trend of $\bar{\eta}$ confirms further that the main overpotential of the process is the lithium transport in the liquid phase, since it decreases by increasing the flow rate.

In order to explain the trend of Q_f/Q_r and $\bar{\eta}$ with the flow rate and the large differences of their saturation values at the various concentrations, it is useful to observe the Scanning Electron Microscope (SEM) images of the porous electrode used in the experiments, reported in Fig. 5.6. The electrode is formed by macropores created by the carbon cloth fibers, where small particles of active material are spread, forming various size pores.

The porous structure of the electrode is not uniform but, on contrary, it is strongly irregular. For this reason, the flow is severely inhomogeneous in the porous matrix of the electrode. It can be supposed that the advection flow mainly passes in the largest pores, created by the carbon cloth fibers, that are probably almost inactive, since they are not filled by the active material. Then the flow passes in the pores created by the agglomerated particles of active material. Here lithium is mainly transported by advection and this explains the positive effect of the flow on captured lithium amount. Nevertheless, in the small pores the flow barely passes or it completely absent. In these pores, lithium transport occurs by diffusion. The lower is the concentration, the higher is the mass transport overpotential. In other words, the difference between the maximum fillings of active material at the various concentrations is due to the diffusion transport occurring in the small pores where the flow is low or absent.

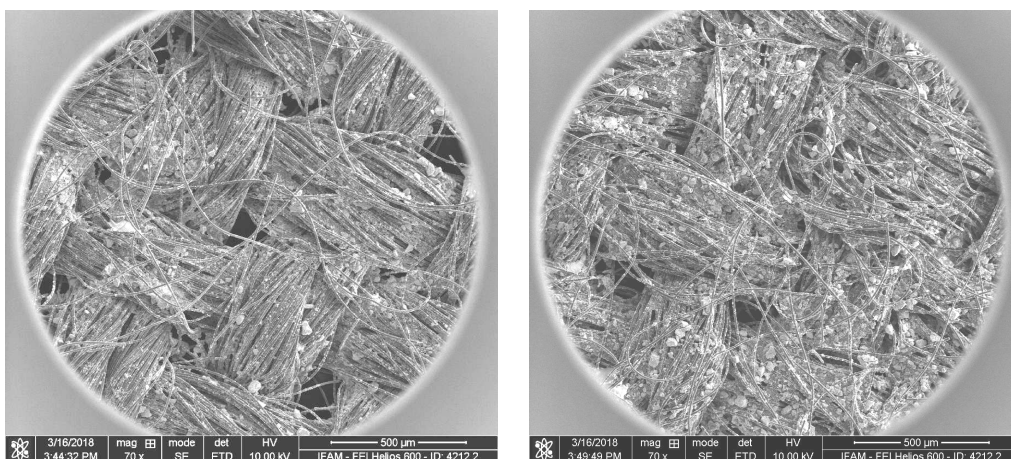


Figure 5.6: SEM images of the LMO electrode, loaded at 5 mg/cm^2 of active material. Dr. Jenz Glenneberg of IFAM institute is greatly acknowledged for having provided these images.

The reduction branches of the GCPL curves obtained at 10 mM and various flow rates (Fig. 5.4 panel d) show the two typical inflection points of LMO occurring at the same potentials even at low flow rates (for example at 0.2 ml/min), but compressed along smaller values of the x-axis. Similar shapes are observed also for the other concentrations, although strongly deformed by the overpotentials, especially at low concentration (1 and 2 mM). This phenomenon is in line with the system description given above. Indeed, the presence of the two inflection points for almost all the curves is given by that part of solid completely filled by lithium. This amount of “active” material is located in the pores that are sufficiently crossed by the advection flow, and their filling increases with the flow rate. On the contrary, the active material in smaller pores does not (or not completely) fill, giving rise to the mass transport overpotential that deforms the curves. In order to prove the interpretation of the results given in this Section, a mathematical model to describe the system has been developed. The model is reported in the next Section.

5.2 Mathematical model of the reactor

5.2.1 Introduction

In this Section a mathematical model of the flow-through electrodes reactor is reported. The model has been developed to simulate the electrochemical behavior of LMO during the capturing step and to understand deeper the occurring phenomena that limit the capture efficiency.

As already mentioned in Chapter 3, flow-through electrodes configuration in fixed bed reactor is widely used for ions removal from streams. The reactor design (estimation of cell length, particles dimension) and the search of the optimal parameters (flow rate, current density) require mathematical models that has been largely investigated and applied in electrochemical engineering field.

One of the first models for flow-through electrodes cell was proposed by Newman [54, 55]. The model of Newman for porous electrode is the most famous in batteries field, due to its simplicity and effectiveness [90, 91, 92, 93]. In this model, the local variables of the balance equations are average values, obtained through the average integral of mass and charge balance over a volume dV of the electrode, large compared to the porous structure and smaller than the region where microscopic variation occurs. The electrode structure is described as mono-dimensional and isotropic. In this way, one can treat the problem using variables that describe macroscopically the system, avoiding the details of complicated microscopic structure of the pores. The porous electrode model applied to flow-through electrodes cell predicts fairly good the cell length and electrolyte flux for an optimal metal removal [54, 55]. Due to the macroscopic treatment, Newman model does not take into account the velocity distribution inside the porous matrix. On the contrary the electrolyte velocity is assumed to be constant throughout the electrode. Nevertheless, the microscopic structure and the velocity distribution can play an important role in some cases, especially when the electrode is composed by particles and pores of various dimensions.

More recent models have introduced a distinction between macropores and micropores into the treatment, in order to take into account the different phenomena that occur at various pore size [62, 94, 95, 96]. These models consider the transport occurring only in macropores, and the interface phenomena (current and double layer) only in the micropores. The transport between the two kinds of pores is at the equilibrium. Although these models are a step forward to a more complete descriptions of porous electrodes, the advection flux is still considered uniform in the macroscopic porous matrix.

In order to prove the interpretation of lithium capture experiments given in the last Section, the use of an average electrode velocity is not sufficient. As the porous structure of the electrode is strongly inhomogeneous, the experimental behavior can be modelled

taking into account a velocity distribution in the porous matrix, which can explain the high diffusion overpotential, even at high flow rates.

The velocity distribution in a porous medium depends on the hydraulic transport properties, which on turn depend by the porous structure [97, 98]. The microstructure can be accurately estimated through many methods, for example micro or nano computer tomography (3D X-ray measurements) [99, 100, 101] and magnetic resonance imaging (MRI) [102, 103]. Obtaining an accurate image of the porous structure and solving the Navier-Stokes equation to get the local velocity, it is possible to extrapolate the pore scale fluid flow [104, 105] and estimate precisely transport parameters of the medium [105, 106]. Although this method leads to very accurate hydraulic model of porous media, it requires a strong computational power and long calculation time.

For these reasons, in this PhD thesis, a more simplified model has been preferred, using a form of the porous structure, that represents schematically the real electrode.

The use of a very simplified description of porous structure has already been used in previous works on lithium ion batteries, for describing the galvanostatic curves [107, 108]. These models have focused mostly on the description of the particle size distribution, in order to study its influence on the mass transport in solid, on the charge transport at the interface and on the current distribution. The most common models [109, 110] consider the active material as an assemble of spheres, representing the particles. Although this representation is a simplified scheme of the real porous structure, the model predicts fairly well the experimental results and it can be considered as a method to optimize the porosity and the particle size distribution of the electrodes.

Taking inspiration from these works, in this section a schematic electrode geometry is used to describe the capturing step in the flow-through electrodes cell. Differently from the above cited models, since the critical step of the process is the transport in the liquid, in this case the microscopic description regards the pores, rather than the particles distribution. Diffusion in the solid can be considered much faster than in the liquid, so that the solid description is neglected. A porous distribution is instead considered, with pores having various sizes and crossed by the flux at different velocities. The pores are assumed to have a specific direction in the space.

The cell is modelled as an assemble of five plates of 12 mm diameter (titanium frit upstream, LMO electrode, separator, NiHCF electrode, titanium frit downstream) in contact with each other (Fig. 5.7). The plates are crossed along their thickness by channels with various diameters, whose axis direction is parallel to the flux. The channels represent the pores of the electrode. A schematic representation of the electrode as a perforated

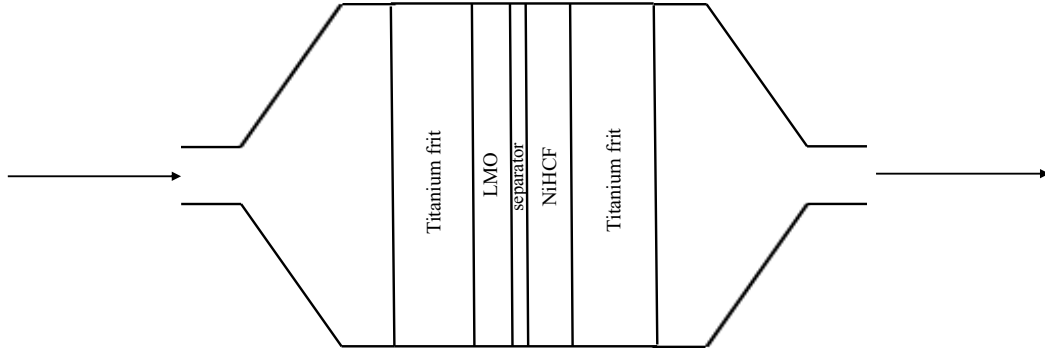


Figure 5.7: Schematic representation of the flow-through electrodes cell.

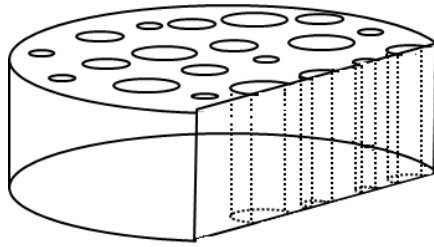


Figure 5.8: Schematic representation in section of the electrode geometry assumed in the model. The dotted lines represent the channels crossing the electrode.

plate is shown in Fig. 5.8. In this configuration, the liquid volume inside a single channel crosses the entire cell length, without contact with the liquid in the other channels. Therefore, the liquid transport across connections between the pores is neglected. The channels with the same diameter are crossed by the liquid at the same concentration $C_{i,k}$ and they are at the same liquid potential ϕ_k , where the index k indicates the channel group with the same diameter and the index i represents the specie.

A direct consequence of this model choice is that LMO and NiHCF electrodes have the same porous distribution, since the channels cross all the cell thickness. This is not true in the real system, as the NiHCF electrode has a different mass loading and porous structure. However, the main interest of this model is the investigation of the lithium transport along the LMO electrode, therefore a detailed description of the counter electrode is not necessary.

The total volume of the electrode V_e , evaluated from its radius (R_e , 6 mm) and thickness (L_e , 400 μm), can be divided into three volume fractions: the solid, the liquid and the carbon cloth volume fractions. The carbon cloth fraction f_{CC} is kept constant at the arbitrary value of 0.47. The solid volume fraction is estimated as $f_s = V_s/V_e$, where

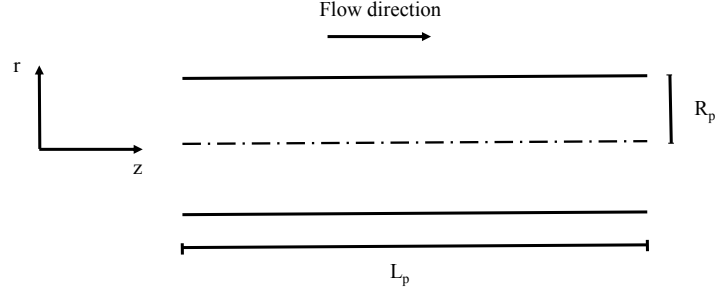


Figure 5.9: Schematic representation of the channel with the reference system.

V_s is the active material volume, which depends on the mass loading of the electrode. The liquid fraction f_l (or electrode porosity) is evaluated from difference between the other fractions, as $1-f_s-f_{CC}$.

5.2.2 Hydrodynamic model

The effect of the inhomogeneous distribution of the flux is simulated considering four types of channels with different diameters. The schematic representation of the channel is reported in Fig. 5.9.

The direction of the flow is parallel to the channel axis (z direction), because the pressure gradient is equal to zero in the other directions. Since the flow regime inside the cell is laminar during the experiments (see Section 5.6), the velocity has a symmetric parabolic profile along the radius, according to the Poiseuille equation:

$$v_p = \frac{\Delta P}{L_p} \frac{R_p^2}{4\mu} \left[1 - \left(\frac{r}{R_p} \right)^2 \right] \quad (5.3)$$

where ΔP is the pressure drop at the electrode extremes, R_p is the pore radius, L_p is the pore length, μ is the solution viscosity and r is the position along the radius. The velocity inside the pore for each channel group is approximated to a mean value, equal to the half of the maximum value, whose position is at the center of the pore ($r=0$).

$$v_{m,k} = \frac{\Delta P R_{p,k}^2}{8\mu L_p} \quad (5.4)$$

The number of pores of the electrode for each group k is calculated from the total volume of electrode V_e , the porosity f_l , the fraction of porosity occupied by a pore group $f_{l,k}$ and the volume of single pore $V_{p,k}$:

$$N_k = \frac{V_e f_l f_{l,k}}{V_{p,k}} = \frac{R_e^2 f_l f_{l,k}}{R_{p,k}^2} \quad (5.5)$$

By means of the velocity $v_{m,k}$ and the pore number N_k , the flow rate crossing a channel group is calculated as:

$$\Gamma_k = v_{m,k} \pi R_{p,k}^2 N_k \quad (5.6)$$

Substituting the definitions of $v_{m,k}$ and N_k in Eq. 5.6, Γ_k becomes:

$$\Gamma_k = \frac{\Delta P \pi R_e^2}{8 \mu L_p} f_l R_{p,k}^2 f_{l,k} \quad (5.7)$$

Γ_k depends from both characteristics of the porous distribution, $R_{p,k}$ and $f_{l,k}$, which are optimized for fitting the experimental data.

In order to simulate the experimental conditions, the total flow rate passing through all the channels must be equal to the flow rate Γ imposed experimentally:

$$\frac{\Delta P \pi R_e^2}{8 \mu L_p} f_l \sum_k R_{p,k}^2 f_{l,k} = \Gamma \quad (5.8)$$

Therefore, once fixed f_l , the values of $R_{p,k}$ and $f_{l,k}$ must be chosen so that they satisfy this condition.

Finally, the fractions of flow rate passing for one pore group $f_{q,k}$ can be defined as:

$$f_{q,k} = \frac{\Gamma_k}{\Gamma} = \frac{R_{p,k}^2 f_{l,k}}{\sum_k R_{p,k}^2 f_{l,k}} \quad (5.9)$$

As it will be shown in the next paragraphs, the value $f_{q,k}$ is an indicative parameter of the efficiency of the process, as it represents the amount of lithium passing through a pore group with respect to the total flow rate and it is linked to the electrochemical behavior of the reactor.

5.2.3 Mass and charge conservation equations

In the system, $C_{i,k}$ and ϕ_k are time and space variables. Specifically, they depend on the z and r directions in the space. In order to describe them, the mass and the charge balance laws are needed. For each species, the following mass balance equation is valid (II Fick's law):

$$\frac{\partial C_{i,k}}{\partial t} = -\nabla \mathbf{J}_{i,k} \quad (5.10)$$

where $\mathbf{J}_{i,k}$ is the flux for each component i for a channel group k .

The quantity $\mathbf{J}_{i,k}$ can be divided into three contribution terms, the diffusive, migrative and convective fluxes:

$$\mathbf{J}_{i,k} = \mathbf{J}_{i,k,diff} + \mathbf{J}_{i,k,migr} + \mathbf{J}_{i,k,conv} \quad (5.11)$$

which are described through the Nernst-Plank equation:

$$\mathbf{J}_{i,\mathbf{k}} = -D_i \nabla C_{i,k} - \frac{z_i F D_i C_{i,k}}{RT} \nabla \phi_k + C_{i,k} \mathbf{v}_{\mathbf{k}} \quad (5.12)$$

where D_i is the diffusion coefficient and z_i is the valence of each specie.

The charge balance equation is easily obtained multiplying each term of Eq. 5.10 for $z_i F$ and summing up for the overall species, considering that

$$\sum_i z_i F C_{i,k} = 0 \quad (5.13)$$

for the electroneutrality condition. One obtains:

$$F \nabla \sum_i z_i \mathbf{J}_{i,\mathbf{k}} = 0, \quad (5.14)$$

which, substituting the Nernst-Plank equation (Eq. 5.12) to explicit the term $\mathbf{J}_{i,\mathbf{k}}$, becomes:

$$\nabla (K_{s,k} \nabla \phi_k) + F \sum_i z_i \nabla (D_i \nabla C_{i,k}) = 0 \quad (5.15)$$

where $K_{s,k}$ is the electrical conductivity of the solution and it is equal to:

$$K_{s,k} = \frac{F^2}{RT} \sum_i z_i^2 D_i C_{i,k} \quad (5.16)$$

In the model only transport along the channel axis has been taken into account, considering the liquid in the radial direction well mixed and no gradient along the radius. This assumption is near to the reality for the small pores ($< 1 \mu\text{m}$), where the transport along the radius is very fast. It becomes progressively less true for bigger pore, where a concentration gradient can be formed in the radial direction, due to the larger diffusion length. Nevertheless, the radial transport has been neglected for all the pore sizes. This could be a strong assumption in some cases, however this simplified treatment can be considered as a good starting point for the development of more complicated descriptions. Furthermore, this assumption is similar to the classic treatment of bed packed flow reactors, where the local movement of the species, namely the microscopic transport from the liquid phase to the active site of the solid, is considered fast. In the traditional approaches only the transport along the reactor axis is taken into account [111, 112, 113]. Using this simplification, the system is treated as mono-dimensional.

In order to simplify the system, the average of charge and mass balance equations over the section of the channel A_p is performed, getting rid of the dependence on r . The average of a function f over the cylindrical pore section is defined as:

$$\bar{f} = \frac{\int_0^{R_p} f(z, r) 2\pi r dr}{A_p} \quad (5.17)$$

Given this definition, the average of Eq. 5.10 can be performed:

$$\int_0^{R_p} \frac{\partial C_{i,k}}{\partial t} \frac{2\pi r}{\pi R_p^2} dr = \int_0^{R_p} -\frac{\nabla \mathbf{J}_{i,k} 2\pi r}{\pi R_p^2} dr \quad (5.18)$$

The left side term can be easily solved, as $C_{i,k}$ is assumed independent by the r direction and the term $\frac{\partial C_{i,k}}{\partial t}$ can be brought out from the integral.

The term $\nabla \mathbf{J}_{i,k}$ can be split in divergence of the axial flux J_z and of the radial flux J_r , by means of the definition of divergence vector:

$$\frac{\partial C_{i,k}}{\partial t} = \int_0^{R_p} -\frac{\partial}{\partial z} J_{i,z} \frac{2r}{R_p^2} dr + \int_0^{R_p} -\frac{1}{r} \frac{\partial (J_{i,r} r)}{\partial r} \frac{2r}{R_p^2} dr \quad (5.19)$$

The first term represents the divergence of the axial flux along the z -axis, which is constant with r . The second term contains the divergence of the radial flux along the radius and it can be integrated as follows:

$$\frac{\partial C_{i,k}}{\partial t} = -\frac{\partial}{\partial z} J_{i,k,z} - \frac{2}{R_p^2} J_{i,k,r} r \Big|_0^{R_p} \quad (5.20)$$

and it becomes:

$$\frac{\partial C_{i,k}}{\partial t} = -\frac{\partial}{\partial z} J_{i,k,z} - J_{i,k,r} \Big|_{R_p} \frac{2}{R_p} \quad (5.21)$$

Substituting the expression of the flux along z , one obtains:

$$\frac{\partial C_{i,k}}{\partial t} = \frac{\partial}{\partial z} \left(D_i \frac{\partial C_{i,k}}{\partial z} + \frac{z_i F D_i C_{i,k}}{RT} \frac{\partial \phi_k}{\partial z} + C_{i,k} v_{m,k} \right) - J_{i,k,r} \Big|_{R_p} \frac{2}{R_p} \quad (5.22)$$

The last term of this equation is the radial flux evaluated at the pore wall and $\frac{2}{R_p}$ is the exchange area per unit of volume (a_{int}) for cylindrical geometry.

Following the same procedure, the charge balance averaged over the channel cross section can be derived, starting from equation Eq. 5.15. One obtains:

$$\frac{\partial}{\partial z} \left(K_s \frac{\partial \phi_z}{\partial z} \right) + F \sum_i z_i D_i \frac{\partial^2 C_{i,k}}{\partial z^2} = I_{k,r} \Big|_{R_p} a_{int} \quad (5.23)$$

The terms $J_{i,k,r} \Big|_{R_p}$ and $I_{k,r} \Big|_{R_p}$ of Eqs. 5.22 and 5.23, represent the phenomena taking place at solid/liquid interface, namely interfacial reactions and current respectively. By means of this mathematical expedient, they are treated like bulk generation terms ($\text{mol}/\text{cm}^3\text{s}$), as they occur throughout all the thickness of the electrode.

During the capturing step, the term $J_{Li^+,k,r} \Big|_{R_p} \frac{2}{R_p}$ in Eq. 5.22 represents the rate of the delithiation, which causes the lithium concentration lowering along the pore. The term of convective flux (or advection flux) depends on the electrolyte velocity $v_{m,k}$, which is proportional to $\Delta P R_{p,k}^2$, as expressed by Eq. 5.4. The depletion of the concentration along the pore is counterbalanced by high pressures and large pores size.

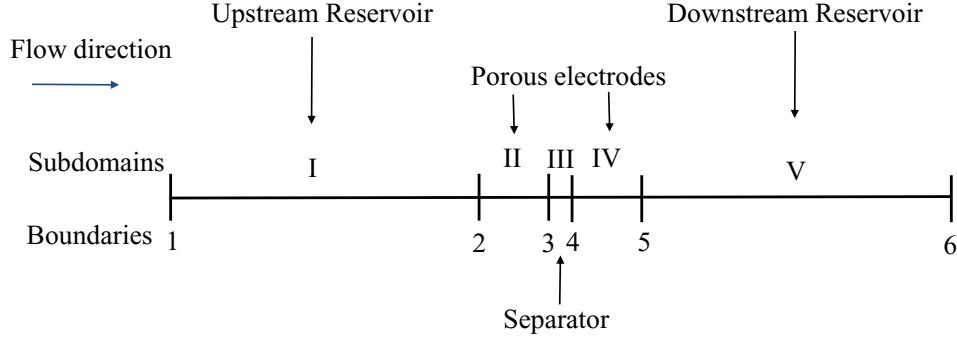


Figure 5.10: Schematic representation of the 1D model domain.

In the next paragraph, the application of these equations and their boundary conditions are reported.

5.2.4 The sub-domains and the boundary conditions

The cell is modelled in one dimension domain (see Fig. 5.10). The outer segments (I and V) represent the titanium frits adjacent to the electrodes (thickness 3 mm). The segment II and IV represent the LMO and the NiHCF electrodes respectively ($400 \mu\text{m}$). The III segment is the separator ($150 \mu\text{m}$).

Reservoirs and Separator

In the reservoirs and the separator (I, III and V sub-domains in Fig 5.10), Eqs. 5.22 and 5.23 are valid for all the components with the terms $J_{i,k,r}|_{R_p} = I_{k,r}|_{R_p} = 0$, because there is no reaction taking place.

At the points 1 and 6 Neumann boundary conditions are applied, namely $J_{i,k,diff}=0$ (the diffusive flux in these points is neglected) and $J_{i,k,migr}=0$, as no ionic current leaves or enters the cell. The variables $C_{i,k}$ and ϕ_k and the fluxes are continues through the boundaries 2,3,4 and 5.

Electrodes

In the electrodes lithium and sodium cations are participating to the (de)-intercalation reactions in LMO and in NiHCF respectively. The term $J_{Li,r}|_{R_p}$ is equal to $r_{Li,k}$ and $J_{Na,r}|_{R_p} = r_{Na,k}$ for the II and the IV sub-domains respectively, where $r_{i,k}$ are the reaction rates ($\text{mol}/\text{m}^2\text{s}$). Chlorine ions do not participate to any reaction, therefore $r_{Cl,k}=0$.

The term $I_{k,r}|_{R_p} a_{int}$ in Eq. 5.23 represents the current at the interface. It is composed by two contributions, the Faradaic current, due to the charge transport at the interface

linked to the reaction, and the charging current, due to the charge of the double layer:

$$I_{i,k} = z_i F r_{i,k} + C_{cdl} \frac{d\Delta\phi_{H,k}}{dt} \quad (5.24)$$

where $\Delta\phi_{H,k}$ is the difference of potential between the solid phase and the liquid phase at the interface in each pore:

$$\Delta\phi_H = \phi_s - \phi_k \quad (5.25)$$

The reaction rate $r_{i,k}$ depends not only on $C_{i,k}$ and $\Delta\phi_H$, but also on the filling of the solid, namely on the concentration of cations in the solid material. Therefore in the II and IV sub-domains the mass balances in the solid phases are necessary. Defining for each channel group k and each reagent species i (Li^+ and Na^+ in the II and IV sub-domains respectively) a solid concentration $C_{s,i,k}$, the equation has the form:

$$V_s f_{s,k} \frac{\partial}{\partial t} C_{i,k} = r_{i,k} A_{s,k} \quad (5.26)$$

where V_s is the total solid volume, $A_{s,k}$ is the exchange area between the solid and the liquid, defined as $2\pi R_{p,k} L_p N_k$, and $f_{s,k}$ is the fraction of solid that exchanges cations with the liquid in the correspondent channel group k . The left side of the equation is the accumulation term of cations in the solid and the right side is the generation term due to the reaction.

The reaction rate expressions

The term $r_{i,k}$ is the reaction rate occurring at the solid-liquid interface. In the sub-domain IV, representing the NiHCF electrode, it is expressed through the Butler and Volmer equation:

$$r_{Na,k} = nk_0 \left[x_k C_T e^{\frac{(1-\alpha)F}{RT}(\Delta\phi_{Hk} - \Delta\phi_H^0)} - \frac{C_{Na,k}}{C_0} (1 - x_k) C_T e^{\frac{-\alpha F}{RT}(\Delta\phi_{Hk} - \Delta\phi_H^0)} \right] \quad (5.27)$$

where $\Delta\phi_H^0$ is the standard potential difference and it is equal to $E^0 + \frac{\mu_e^{NiHCF}}{F}$, with E^0 defined as in Eq. 2.17, C_T is the maximum concentration of the active material, $(1 - x_k)C_T$ and $x_k C_T$ are the concentrations of the empty and filled interstitial sites respectively for each channel group, $C_{Na,k}$ is the concentration of sodium cations in the liquid, n is the number of electrons involved in the reaction (in this case equal to 1), α is the barrier coefficient ($\alpha = 1/2$ in the numerical calculations), k_0 is the kinetic constant of the reaction (expressed in m/s) and C_0 is a reference concentration (1 M was chosen for all the species arbitrarily).

It is worth to notice that this form of the Butler and Volmer equation is different from the form presented in Eq. 2.6, where the reaction rate was expressed as a function

of the overpotential; in this case it is written as a function of the potential difference at the interface $\Delta\phi_{Hk}$. If $r=0$, the system is at equilibrium and Eq. 5.27 falls into the form of Eq. 2.24.

The expression of the reaction rate of LMO in the II sub-domain includes mathematically the LMO equilibrium potential profile derived in Section 4.1.

As mentioned in Section 2.2, the equilibrium potential can always be expressed as a sum of an ideal potential and an excess potential:

$$E_{eq,LMO} = E_{id} + E_{exc} \quad (5.28)$$

where $E_{eq,LMO}$ is the potential expression of Eq 4.5 derived in Section 4.1, which contains the dependence of LMO potential from lithium concentration in the solid and in the liquid, while E_{id} is:

$$E_{id} = \frac{RT}{F} \ln \frac{1-x}{x} \quad (5.29)$$

Deriving E_{exc} from Eq. 5.28 and 5.29, one obtains:

$$E_{exc} = E_{eq,LMO} + \frac{RT}{F} \ln \frac{x}{1-x} \quad (5.30)$$

This is a potential expression as a function of the concentration in the solid material, which describes the intercalation in the two solid solutions of LMO as non ideal behavior of the intercalation process. It can be included in the Butler and Volmer equation for each channel group k as follows:

$$r_{Li,k} = k_0 \left[x_k C_T e^{\frac{(1-\alpha)F}{RT} (\Delta\phi_{Hk} - \frac{\mu_e^{LMO}}{F} - E_{exc,k})} + \frac{C_{Li,k}}{C_0} (1-x_k) C_T e^{\frac{-\alpha F}{RT} (\Delta\phi_{Hk} - \frac{\mu_e^{LMO}}{F} - E_{exc,k})} \right] \quad (5.31)$$

This expedient allows to include the effect of the equilibrium potential of LMO in the kinetic of the reaction through the Butler and Volmer equation. Indeed, when $r_{LMO}=0$, the interface is at equilibrium and the equation becomes:

$$\Delta\phi_{Hk} - \frac{\mu_e^{LMO}}{F} = E_{exc} - \frac{RT}{F} \ln \frac{x_k}{1-x_k} = E_{eq,LMO} \quad (5.32)$$

This procedure has been already used by Doyle et al. [93]. They found an arbitrary function that fits the potential profile of LMO material and they included it in the Butler and Volmer equation. This arbitrary function depends only on the lithium concentration in the solid and not in the liquid, unlike the Eq. 5.30, where the liquid concentration is included in the term $E_{eq,LMO}$ (Eq. 4.5).

The global equations

After having defined the equations valid for each channel group k , the global equations valid for the entire electrode are reported. The total current imposed on the cell is defined as the sum of the currents integrated over the exchange area in each channel group:

$$I_{tot} = \sum_k \int_{A_{s,k}} I_k dA \quad (5.33)$$

and developing the expression:

$$I_{tot} = 2\pi \sum_k N_{p,k} R_{p,k} \int_0^{L_e} I_k dx \quad (5.34)$$

The total cell potential measured experimentally is defined as the difference of Galvani potential of the solid between the two electrodes plus the transfer work of the electron from one electrode to the other:

$$\Delta V = \phi_{s,II} - \phi_{s,IV} - \frac{\mu_e^{LMO} - \mu_e^{NiHCF}}{F} \quad (5.35)$$

where $\phi_{s,II}$ is the solid potential of the working electrode (LMO, II sub-domain) and $\phi_{s,IV}$ is the solid potential of the counter electrode (NiHCF, IV sub-domain). $\phi_{s,II}$ is imposed equal to 0, so that the Eqs. 5.34 and 5.35 work as a potentiostat does: while the current I_{tot} is flowing into the system, ΔV is recorded, grounding the working electrode and imposing the counter electrode potential ($\phi_{s,IV}$).

5.2.5 Simulations

The system of equations was solved with the software COMSOL Multiphysics 5.3, based on the finite element method. The initial values of the variables have been set so that the system is at the equilibrium at the beginning of the simulations ($t=0$). The starting ion concentrations are equal to the brine concentration ($C_{Li^+} = 1,2,5$ or 10 mM, $C_{Na^+} = 1$ M and $C_{Cl^-} = C_{Li^+} + C_{Na^+}$); LMO is almost completely oxidized at the beginning (starting concentration 5% of the maximum solid concentration), NiHCF is half-oxidized (starting concentration is 50% of the maximum). From the starting liquid and solid concentrations values, the initial equilibrium potentials at the interfaces E_{eq} for the LMO and the NiHCF electrodes are evaluated. Their difference is the starting value of cell potential, ΔV .

The GCPL curves were calculated as follows: after 5 seconds in equilibrium condition ($I_{tot}=0$), a constant value of I_{tot} is given, (1 mA, positive or negative), ΔV is calculated over time, together with the $C_{i,k}$ and ϕ_l along the cell thickness, and the sodium and lithium concentrations in the solid. When ΔV reaches the potential extremes (ΔV_1 and ΔV_2), the current is switched in direction. Then the charge passed in the system is evaluated as a integral of the current over the time:

$$Q = \int I_{tot} dt \quad (5.36)$$

The meshing of the subdomains have been divided so that the farther is the position from the reaction region, the larger are the elements. This is due to the high precision requested to calculate lithium concentration profile during the capture near the reaction zone. A geometric sequence of the elements was used in all the sub-domains, distributed so that the smallest elements are always near the boundaries.

The I and V sub-domains (cell reservoirs) and the III sub-domain (separator) are divided in 50 elements, with an element ratio of 20. The element ratio is the ratio between the largest and the smallest element in the sub-domain. The IV sub-domain (NiHCF electrode) is divided into 200 elements with an element ratio of 50. The II sub-domain (LMO electrode) is the densest one, with 500 elements and an element ratio of 100. In this region, the lithium capture occurs, therefore a very high precision is needed, as the lithium concentration tends to 0. It may be necessary to further increase the elements number and the element ratio, for the most diluted concentrations (1-2 mM) and high convective fluxes.

5.2.6 Simulations parameters

The parameters used in the simulations are reported in Table 5.1. k_0 and C_{cdl} values used in the simulations are evaluated experimentally by Erinwmingbovo, whose work has not been yet published. The evaluation was performed by means of dynamic impedance measurements, a new technique used to investigate battery materials kinetic, developed by La Mantia et al. [114]. f_s value is evaluated from the mass loading of the active material (5 mg/cm²). C_T for the LMO is calculated from its weight density (4.1 g/cm³) and it corresponds to the ideal capacity of LMO (146.8 mAh/g). C_T of NiHCF is instead chosen arbitrarily 4 times larger than C_T of LMO, so that the total charge of NiHCF is larger than the one of LMO. Moreover a very large capacity of NiHCF allows to minimize the change of potential of NiHCF due to (de)intercalation of Na⁺, so that the variation of the total potential cell ΔV can be approximated to the variation of LMO potential. The value of Na⁺ concentration is kept constant at 1 M for all the simulations. This value is higher than the one used experimentally (100 mM), so that no diffusion effect due to lack of Na⁺ in the NiHCF influences the total cell potential. $E_{1,LMO}^0$, $E_{2,LMO}^0$ and E_{NiHCF}^0 values have been chosen arbitrarily to get a cell potential similar to the experimental one. The hydraulic resistance of the electrode R_h is defined for laminar flow as the ratio between the pressure drop on the electrode and the flow rate:

$$R_h = \frac{\Delta P}{\Gamma} \quad (5.37)$$

Parameters	Values
k_0	4.7e-7 cm/s
C_{cdl}	0.47 $\mu\text{F}/\text{cm}^2$
f_s	0.03
f_l	0.5
f_{CC}	0.47
$C_{T,LMO}$	22.46 M
$C_{T,NiHCF}$	91.44 M
$E_{1,LMO}^0$	0.9 V
$E_{2,LMO}^0$	0.75 V
E_{NiHCF}^0	0.35 V
μ_e^{LMO}/F	0.05 V
μ_e^{NiHCF}/F	0.1 V
R_h	0.3 mbar min/ml
T	298 K
D_{Li^+}	1.03e-5 cm^2/s
D_{Na^+}	1.33e-5 cm^2/s
D_{Cl^-}	2.03e-5 cm^2/s

Table 5.1: Simulations parameters.

Group number k	1	2	3	4
R_p	2.4 nm	0.24 μm	9.4 μm	23.6 μm
$f_{l,k}$	7e-4	0.8818	0.08	0.0375
N_k	2.3e9	2.9e8	16.2e3	1216
$f_{s,k}$	0.05	0.15	0.8	0
$f_{q,k}$	1.4e-10	1.75e-3	0.254	0.744

Table 5.2: Pores numbers, liquid fractions, solid fractions and flow rate fractions for the various pore sizes.

The value used in the simulation is extrapolated experimentally by pressures measurement on the cell at various flow rates, as reported in Sect. 5.6. The value of the diffusion coefficients are taken from the literature [65]. The potential extremes of the cycle ΔV_1 and ΔV_2 are chosen so that the mean overpotential is equal to 0.3 V for each investigated concentration:

$$\Delta V_1 = \bar{E}_{eq,LMO} - \bar{E}_{eq,NiHCF} + 0.3 \quad (5.38)$$

$$\Delta V_2 = \bar{E}_{eq,LMO} - \bar{E}_{eq,NiHCF} - 0.3 \quad (5.39)$$

As the overpotential on NiHCF is small, the total overpotential can be considered equal to the LMO overpotential. The difference between the potential extremes is 0.6 V, like in the experiments.

All the parameters regarding the porous structure of the electrode, namely the pore liquid and solid fractions ($f_{l,k}$ and $f_{s,k}$) as well as the radius of the pores ($R_{p,k}$) have been assumed to simulate the experimental results. The chosen porous distribution is made by four pore sizes. This leads to 12 free parameters of the porous structure (4 radii of the pores, 4 solid fractions and 4 liquid fractions). The pore group of biggest size is assumed to be electrochemical inactive ($f_s=0$). These pores represent the holes of the carbon cloth, which are not filled by the active material.

The follow procedure has been used to get the other parameters. Their values have been initially hypothesized to simulate the GCPL curves in 40 mM of LiCl (Fig. 5.2 (a)) at 0 and 0.1 ml/min. If the charges predicted by the model for these two cases is similar to the experimental ones, the same parameters are used to simulate the Q_f/Q_r curve vs. M_f for 10 mM LiCl, eventually adjusting their values to adapt the curve shape to the experimental one. After that, the Q_f/Q_r curve at 1 mM LiCl is simulated, modifying again the parameters if necessary, to get Q_f/Q_r values as close as possible to the experimental ones. The procedure is then repeated from the beginning, until the parameters give results as much similar as possible to the experiments.

Once fixed $f_{l,k}$ and $R_{p,k}$ values, the number of pores for each group N_k are fixed by Eq. 5.5, as well as flow rates passing for each channel group (Γ_k). The tested parameters have been always chosen so that $\sum_k f_{s,k} = 1$, $\sum_k f_{l,k} = 1$ and the total flow rate is equal to the experimental one, condition expressed by Eq. 5.8.

The final chosen parameters are reported in Table 5.2. The radius of the active pores are 9.4 μm , 0.24 μm and 2.4 nm. Most of the active material is assembled to form macropores with 9.4 μm radius ($f_{s,3}=0.8$). Smaller pores are made of less material. The flow rates passing for each channel group are reported in Table 5.2 as a fraction of the total flow rate ($f_{q,k}$). The nanopores with $R_p=2.4$ nm have almost 0 flow. The micropores of 0.24 μm radius are crossed by circa 0.175 % of the flow. The 25 % of the flow crosses the

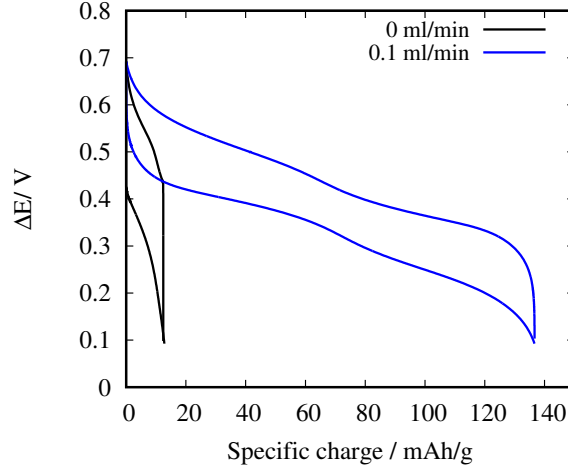


Figure 5.11: Simulated GCPL curves in 40 mM LiCl and 1 M NaCl solution, at 0 and 0.1 ml/min.

macropores of 9.4 μm radius. The main amount of flow passes by the inactive macropores of 23.6 μm radius (75 %).

5.2.7 Analysis of the results

Simulations of GCPL measurements at the same conditions of experiments shown in Fig. 5.2 (a) (40 mM of LiCl, at 0 and 0.1 ml/min) are reported in Fig. 5.11.

Q_f at 0 and 0.1 ml/min flow rates are fairly close to the experimental curves of Fig. 5.2 (a). The error on Q_f value at 0.1 ml/min is around 20%, which is considered acceptable. The shape of the curves are also similar. The curve at 0.1 ml/min presents the characteristic shape of the LMO potential profile.

In Fig. 5.12 (a) the cell potential is reported vs. the charges accumulated in each pore group participating to the capture ($R_{p1}=2.4$ nm, $R_{p2}=0.24$ μm and $R_{p3}=9.4$ μm). The pores of 23.6 μ radius representing the holes of the carbon cloth do not participate to the reaction, as they are electrochemically inactive ($I_4=0$). The charge is evaluated from the integral over time of the current passing for each pore group:

$$Q_k = 2\pi N_{p,k} R_{p,k} \int \int_0^{L_e} I_k dx dt \quad (5.40)$$

As expected, the main charge amount is stored in the macropores, as they are formed by the highest amount of active material and they are crossed by the highest flow rate. In panel (b) of Fig. 5.12, the filled solid fraction of each pore group, M_p , is reported, evaluated as the accumulated charge in each pore group divided by the respective maximum charge:

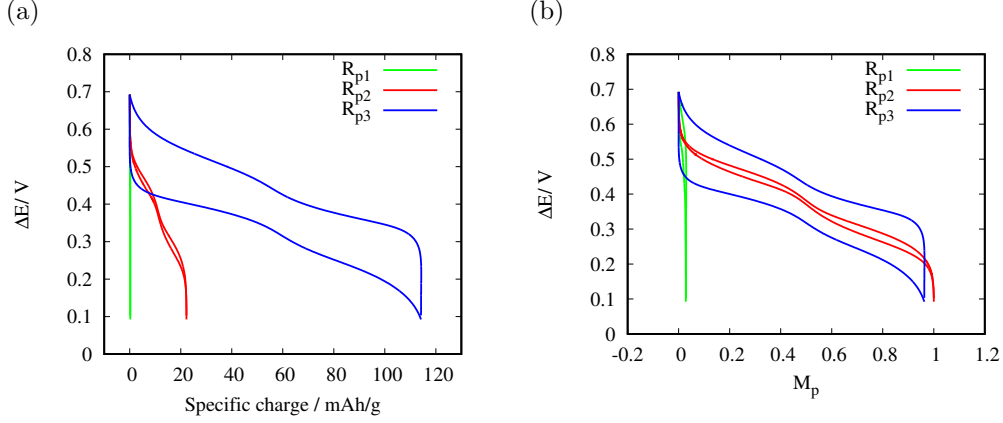


Figure 5.12: Accumulated charge (a) and filled solid fraction (b) vs. cell potential for each pore group in 40 mM LiCl and 1 M NaCl solution, at 0.1 ml/min.

$$M_{p,k} = \frac{Q_k}{FC_{T,LMO}V_s f_{s,k}} \quad (5.41)$$

In 40 mM LiCl, the pore groups of 0.24 and 9.4 μm radii are filled completely ($M_p \approx 1$). For the pores of 2.4 nm radius, M_p is instead almost 0: the nanopores do not charge. They are composed by 5% of total solid never participating to the capture.

Simulations at 1, 2, 5 and 10 mM LiCl, with 1 M NaCl are carried out, with the same M_f range used experimentally. The GCPL curves are reported in Fig. 5.13, in panel (a), (b), (c) and (d) for 1, 2, 5 and 10 mM respectively. The reduction branches of the curves at various flow rates are different, while the oxidation branches match with each other. Q_f values increase with the flow rate until a maximum value, different for each concentration, as occurs experimentally. This confirms that the model predicts the mass transport overpotential effect occurring during the reduction and the positive effect of the flow rate.

Nevertheless, the difference in the maximum reduction charge between the various concentrations are smaller than in the experimental curves of Fig. 5.4. This is clearly visible in the Q_f/Q_r vs. M_f curves reported in Fig. 5.14, extrapolated from the simulated GCPL curves for all Li^+ concentrations (a) and reported again from experimental curves (b). Q_r used for the simulated curves is equal to 136 mAh/g, which is the maximum charge obtained in 40 mM of LiCl at 0.1 ml/min (Fig. 5.11). For $M_f < 1 \mu\text{mol}/\text{min}$ the two curves shows good similarity for all concentrations, showing an increase of Q_f/Q_r with M_f less then linear. As mentioned before, in this region the critical value is the amount of lithium pumped into the cell (0-1 $\mu\text{mol}/\text{min}$), which is comparable with the capturing rate (1 mA that corresponds to 0.6 $\mu\text{mol}/\text{min}$). At $M_f > 1 \mu\text{mol}/\text{min}$, the

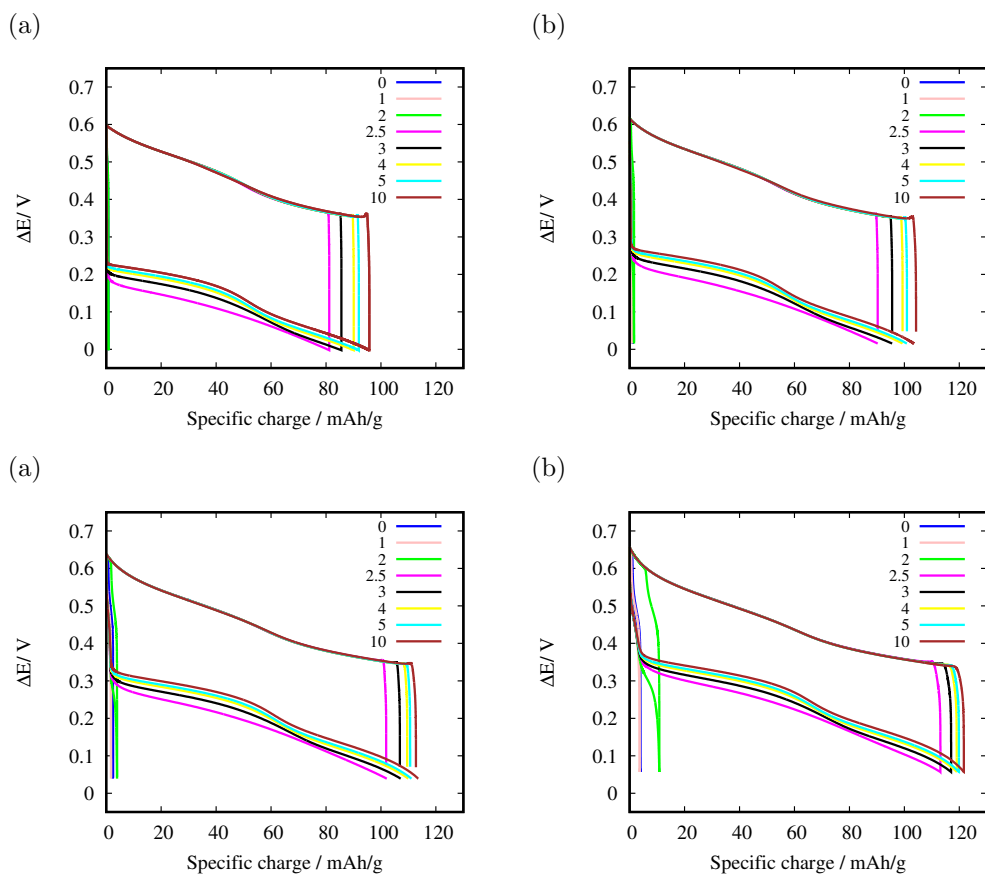


Figure 5.13: Simulated galvanostatic curves vs. total cell potential for 1, 2, 5 and 10 mM LiCl and 1 M NaCl at various molar flow rates. The values of M_f used are equal to the experimental values and they are reported in the legend in $\mu\text{mol}/\text{min}$.

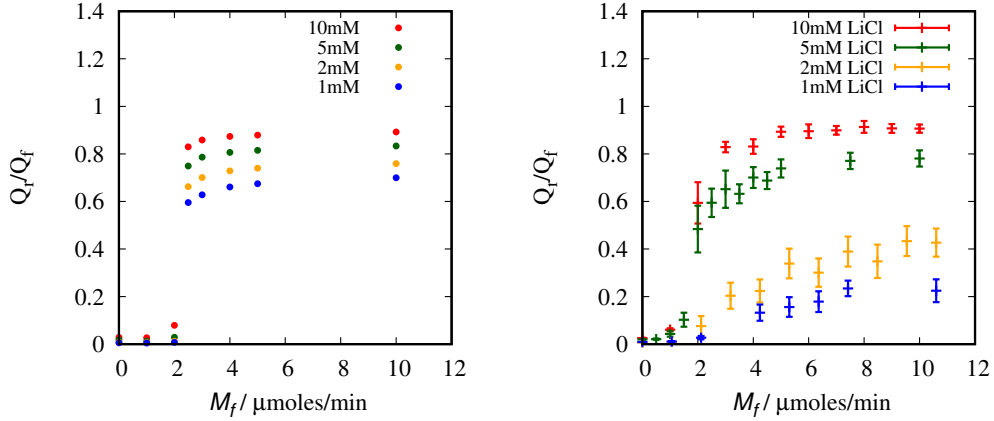


Figure 5.14: Q_f/Q_r vs. M_f extracted from the simulated galvanostatic curves (panel (a)) and from the experimental curves (panel (b)) at 1, 2, 5 and 10 mM of LiCl.

10 mM LiCl curve matches fairly well with the experimental one. The saturation flow rate in both cases occurs at circa $3 \mu\text{mol}/\text{min}$ and the maximum Q_f/Q_r value is 0.9. At 5 mM, the two curves are still fairly similar, although their difference in Q_f/Q_r values is larger than the one of the curves at 10 mM. On the contrary, at 1 and 2 mM of LiCl, Q_f/Q_r values extrapolated from the model is much higher than the experimental values. This difference will be discussed later, now the attention will be focused on the simulation results.

The shape of the GCPL curves of Fig. 5.13 can be better commented, looking to the normalized charge for each channel group ($M_{p,k}$). The discussion is restricted for the extreme cases, namely for the curves at 1 mM and 10 mM of LiCl. Fig. 5.15 shows M_p obtained at 1 and 10 mM LiCl, for the pores of 2.4 nm radius (panels (a) and (b)), of 0.24 μm (panels (c) and (d)) and of 9.4 μm (panels (e) and (f)).

In both solutions, the charge in the macropores mainly contributes to the total charge. $M_{p,3} \approx 0.8$ and 0.9 at high fluxes, namely the volume of macropores is almost totally filled. That leads to the two characteristic plateaus of LMO in the total charge curves of Fig. 5.13, deformed by the overpotential, as the flow rate decreases. The two plateaus were observed also in the experimental curves and they were explained admitting the existence of a part of active material not limited by diffusion, but filled almost completely by lithium. Generally, this material belongs to the pores that are large enough to be abundantly crossed by the convective flow. According to the model, these are macropores and their size distribution is represented by the pores of 9.4 μm radius.

The nanopores (2.4 nm) almost does not contribute to the charge. In both concentra-

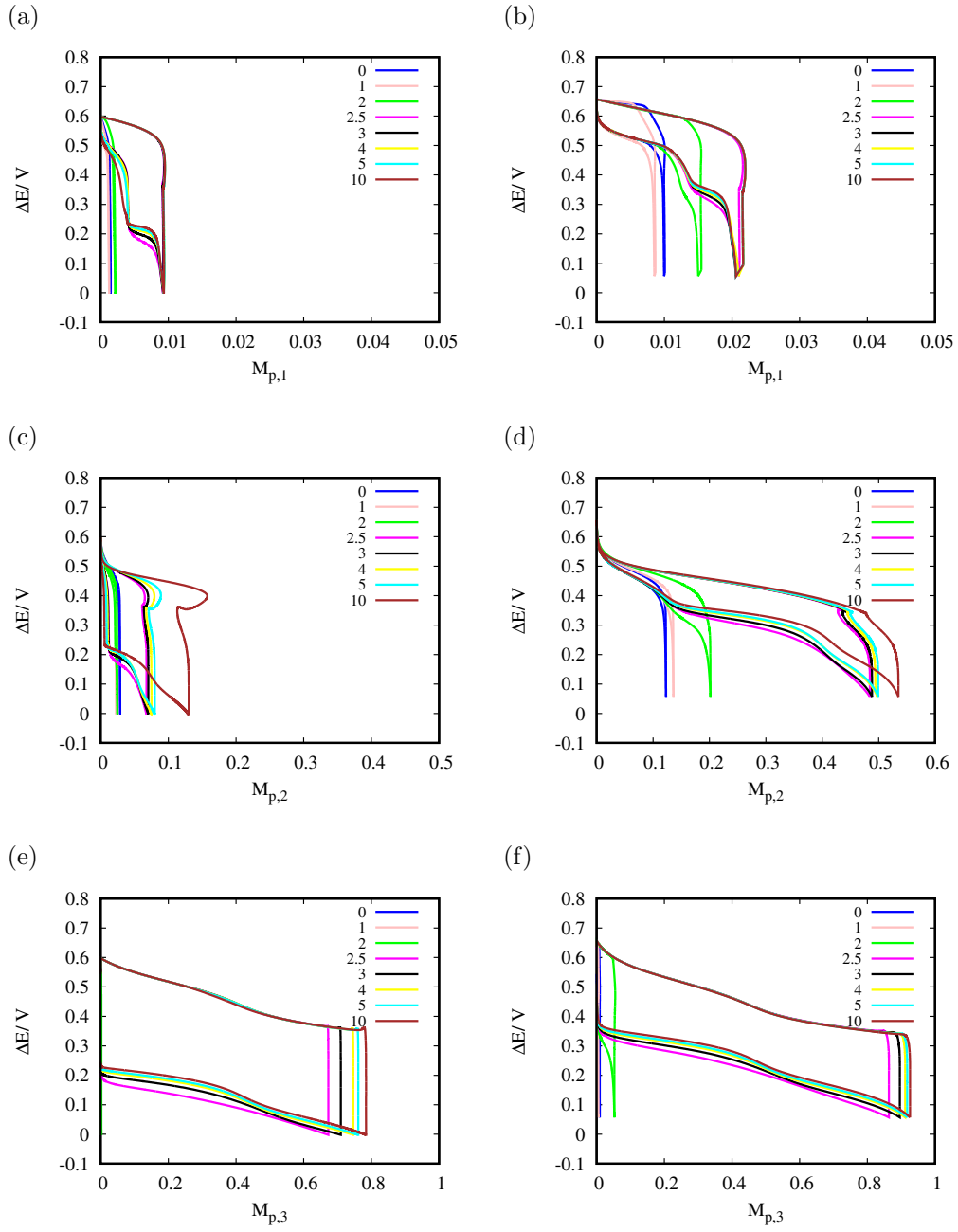


Figure 5.15: Fraction of filled solid M_p at 1 mM and 10 mM LiCl and 1 M NaCl for $R_p=2.4$ nm (panel (a) and (b) respectively), $R_p=0.24$ μm (panel (c) and (d)) and $R_p=9.4$ μm (panel (e) and (f)).

tions, $M_{p,1}$ saturation value is lower than 2%.

The 0.24 μm pores (Fig. 5.15 panel (c) and (d)) have the highest difference in filling at the two concentrations and the effect of flow rate is significant, especially in 10 mM LiCl. Indeed in this case, $M_{p,3}$ increases from 0.1 to 0.53 (panel (d)). In 1 mM LiCl solution, the flow effect in these pores is less significant and $M_{p,3}$ goes from 0.02 to 0.13 (panel (c)). This pore group represents the part of active material that becomes more “active” as the flow rate increases, and whose filling changes appreciably with the concentration.

A deeper analysis of the results can be carried out looking to the concentration profiles of Li^+ along the cell length. They were reported for 1 and 10 mM of LiCl solutions and each pore size, at two values of M_f , 2 and 10 $\mu\text{mol}/\text{min}$ (Fig. 5.16 and Fig. 5.17 respectively). Each concentration profile reported is extrapolated at a specific potential of the reduction curve. The selected potentials at each size pore are the same for both concentrations, differing only for a Nernstian potential ($\frac{RT}{F}\log(10)$), to exclude the shifting of potential due to thermodynamic effect of concentration. The change of concentration profile with the potential corresponds to the change with time. As the cell potential decreases (namely the reduction of LMO takes place), the capture goes on and lithium concentration in liquid decreases.

Fig. 5.16 shows the concentration profiles at 2 $\mu\text{mol}/\text{min}$ in 2.4 nm, 0.24 μm and 9.4 μm radii pores, in 1 mM (panel (a), (c) and (e) respectively) and 10 mM (panel (b), (d) and (f)). These profiles correspond to the green GCPL curves in Fig. 5.13 (a) and (d).

As reported in the literature regarding packed bed columns [115], the reactant concentration varies along the length of the reaction region. In the presented case this area corresponds to the LMO electrode, whose position is the interval 3-3.4 mm of the total cell length. A magnification around this length is reported in each graph.

The typical concentration profile is the so-called “breakthrough” curve, which has a S-shape. Generally, it is characterized by a “breakthrough” point, that is achieved when the reactant concentration reaches 5% of the initial value due to the consuming reaction, and by an “exhaustion” point, where the concentration tends to the bulk value. Between this two values, there is usually an inflection point, in correspondence of a change in the mass transfer mechanism [112].

In this case, in 2.4 nm and 0.24 μm radii pores (Fig. 5.16, panel (a), (b), (c) and (d)), due to the presence of the reservoirs, the profiles show two symmetric inflection points near the electrode boundaries. As the reaction starts, lithium concentration begins to deplete very fast with potential, forming a concavity in correspondence of the electrode. In this region, the convective flux is not strong enough to supply the reaction and the concentration goes down to the “breakthrough” point. The transport of lithium towards

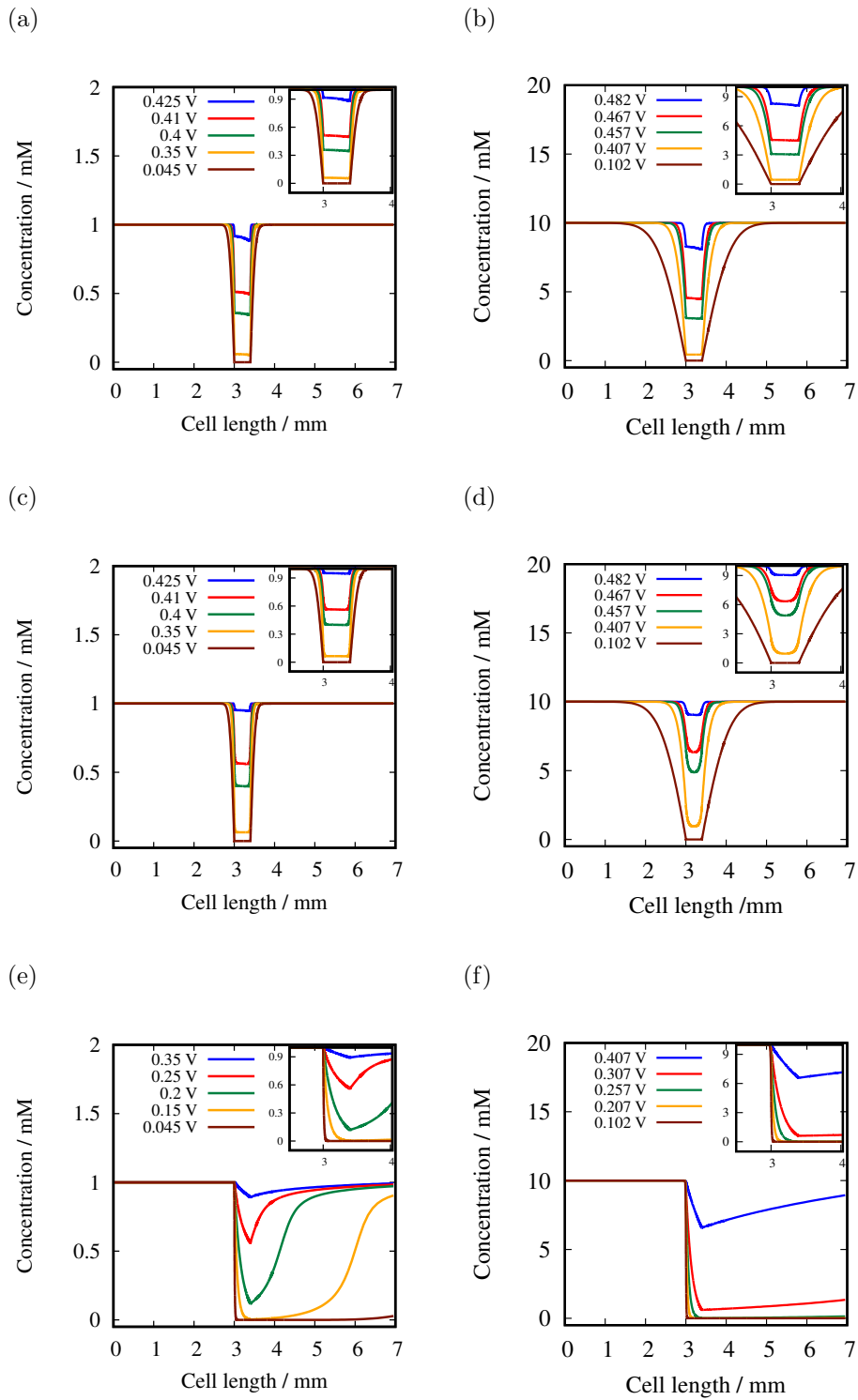


Figure 5.16: Concentration profiles at $2 \mu\text{mol}/\text{min}$ at 1 and 10 mM LiCl in the pores of radii 2.4 nm (a and b), 0.24 μm (c and d) and 9.4 μm (e and f).

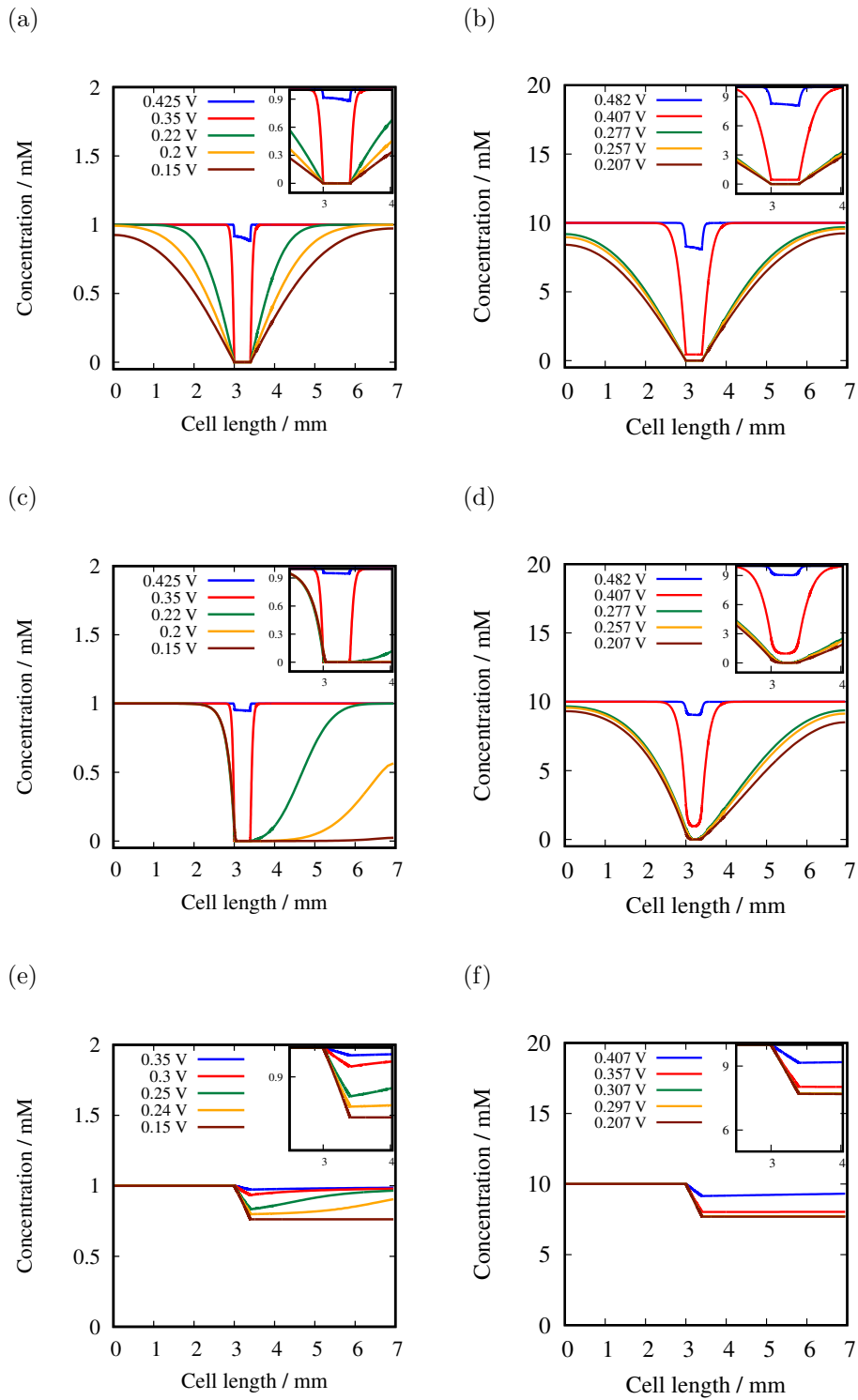


Figure 5.17: Concentration profiles at $10 \mu\text{mol}/\text{min}$ at 1 and 10 mM LiCl in the pores of radii 2.4 nm (a and b), $0.24 \mu\text{m}$ (c and d) and $9.4 \mu\text{m}$ (e and f).

the LMO electrode occurs through diffusion from upstream and downstream. The two inflection points are between the non-reactive zone (where the concentration is equal to the feed concentration) and the LMO electrode, where the concentration tends fast to zero.

It can be noted that the inflection points are steeper for 1 mM than for 10 mM. The profiles are broader in 10 mM LiCl, especially at the lower potentials: the delithiation at 10 mM occurs in a larger cell length. This is due to the different volumes treated in the two cases. Indeed, although the lithium mass flow is the same for both concentrations, the volumetric flows are very different (10 times higher for 1 mM LiCl). Since the capturing rate is the same (1 mA), in 10 mM LiCl the brine delithiation rate is higher, due to the smaller flowing volume.

In the pores of 9.4 μm radius (panel (e) and (f)), the upstream concentration (for cell length lower than 3 mm) keeps constant thanks to the high electrolyte flux. In correspondence of the electrode, the concentration suddenly decreases, hereafter there is a sudden change of slope and concavity, due to the presence of a lithium diffusive flow from downstream. The reached minimum concentration in proximity of the electrode reduces increasingly as the reaction goes on, until the curve is completely flattened at the value of 0 at the lowest potential. The profiles change with potential more abruptly at 10 mM, than in 1 mM. In the latter indeed, only the curve at the lowest potential reaches 0 mM, the other curves gradually move towards it. Instead at 10 mM LiCl after the steep change near to the left boundary of the electrode, almost all curves are near or equal to 0 mM. This is again an effect of the different volumetric flow rates.

Interesting to notice is that, along LMO electrode, in biggest pores, the concentration profiles have a linear decrease, that gradually becomes exponential, as the reaction goes on. This behavior was mentioned in the description of the PFR reactor in Sect. 2.4, and it is due to the progressive increase of the mass transport overpotential upon time.

In the nano and micropores, the main lithium depletion occurs fast at high potentials, 0.425-0.35 V (for 1 mM) and 0.482-0.407 V (for 10 mM), while in the macropores the concentration is still high enough to supply the reaction at the same potential range (Fig. 5.16, panel (e) and (f), blue curve). At lower potential values, in the smallest pores, the concentration does not change further, while in the pores of 9.4 μm radius, it starts to deplete, until it does not reach the value of 0. Only at these point, the lowest potential is reached and the capturing process is interrupted. In the pores of 2.4 nm and 0.24 μm radii, the current is so small that the lithium capture is compensated by the convective flux, so that the concentration profile keeps constant after a rapid initial change. In the biggest pores instead, where the main capture occurs, the concentration continues to decrease until the end of the reaction.

At this flow rate, the difference in captured lithium between the two concentrations is

not very high. Although at 10 mM the captured lithium is slightly higher than at 1 mM, this difference is not evident in the profile concentration, where the diffusion effects seems to be strongly present in all the pores (in various intensity), even at 10 mM. Generally it can be said that at low flow rates lithium flux in the cell is not enough to compensate the diffusion effects for both concentrations even in the macropores, where the concentration tends quite fast at 0. This behavior explains the low capturing efficiencies obtained experimentally at low flow rates, for $M_f \leq 2 \mu\text{mol}/\text{min}$ (Fig. 5.14 (b)).

The situation is different at $10 \mu\text{mol}/\text{min}$. In this case, as expected from Fig 5.14 (a), the amount of captured lithium is different for the two concentrations.

In the macropores (Fig. 5.17, panel (e) and (f)), the concentration profiles are similar in both solutions. They have a linear decrease on the LMO electrode and they keep constant in the downstream reservoir at a value near to the bulk concentration. Hence the current is far from the limiting diffusion value. This is in line with the M_p curves of Fig. 5.15 (panel (e) and (f), amaranth curve), that shows an high filling of macropores at $10 \mu\text{mol}/\text{min}$ in both solutions ($M_{p,3}=0.8-0.9$).

Therefore, the capturing process this time is not limited by lack of lithium in the big pores and it can proceed longer. The higher capturing time and the larger flow rate allow a further filling also in the micropores, where the amount of captured lithium is increased respect to low flow rates.

In the micropores of $0.24 \mu\text{m}$ radius, the accumulated charge at $10 \mu\text{mol}/\text{min}$ differs substantially for the two concentrations ($M_{p,2}=0.13$ at 1 mM and 0.53 at 10 mM). This difference can be appreciated also from the concentration profiles (Fig. 5.17, panel (c) and (d)). At initial potentials, the concentration profiles form the concavity near the electrode, like seen previously at low flow rate. This time, at 1 mM, as the capture proceeds, the slope of the breakthrough curve downstream decreases slowly, until it flattens at 0 mM. On the contrary, at 10 mM, even at the lowest potential, the curve is not flattened: enough lithium is transported towards the LMO electrode from downstream and upstream to supply the reaction. This explains the difference in $M_{p,2}$ at $10 \mu\text{mol}/\text{min}$ in Fig. 5.15 (panel (c) and (d), amaranth curve).

In the nanopores (Fig. 5.17 panel (a) and (b)) the profile shapes are quite similar for both concentrations, with the difference that at 10 mM the curves almost overlap at low potentials, while at 1 mM the change is more gradual, like already discussed before.

Concluding, according to the results, the highest difference in filling between the two concentrations at the saturation is given by the micropores of $0.24 \mu\text{m}$ radius, that corresponds to charge difference of $9 \text{mAh}/\text{g}$. The difference in Q_f/Q_r between 1 and 10 mM LiCl shown in Fig. 5.14 (a) (which correspond to $\approx 22 \text{mAh}/\text{g}$) is given by both pores of 0.24 and $9.4 \mu\text{m}$ radii. Although the difference in filling between the two

concentrations in the macropores is only 0.1, it leads to a difference in charge of 12 mAh/g, as they are made by the highest fraction of solid.

The difference in Q_f/Q_r values between 1 and 10 mM predicted by the model is circa 0.2 at the saturation, much lower than the difference predicted by the experiments (0.7). Results of simulations with other porous distributions (at various $f_{l,k}$ and $R_{p,k}$) are reported in the following paragraph, where it will be shown that, by using a distribution richer of nano or micropores, the difference does not enlarge. This discrepancy between model and experiments can be attributed to the electrode porous structure. Indeed, in the model, the electrode is assumed to be a solid plate, perforated by straight channels representing the pores. In this way the active solid is assumed to be well compact and homogeneous. The SEM images of Fig. 5.6 show the real electrode structure, very different from the perforated plate assumed in the model. The active particles are randomly spread on the substrate and the carbon cloth fibers are not properly filled by the material. The active pores are far from being well defined and evenly distributed.

Despite this difference, the model simulates fairly well the trend of Q_f/Q_r with M_f at 10 mM, but it predicts much higher capture efficiencies than the experiments at concentrations lower than 5 mM. This suggests that the performances at low concentrations can be improved with a more homogeneous and compact electrode, which resembles more to the ideal one assumed in the simulations.

Moreover, according to the model, the Q_f/Q_r curve shape does not change with the concentration. The curves at various concentrations can be rescaled in the y-axis to be almost identical and the saturation charges are reached at the same M_s for all the concentrations. This is different from the experimental curves, where M_s for the various concentrations are similar but not exactly equal. This difference can be attributed again to diffusion effects not included in the model, due to the non-ideal structure of the electrode.

5.2.8 Effect of porous structure parameters

Until now the results shown in this Section have been obtained using the pore sizes and the porous distribution reported in Table 5.1. These parameters, among all those tested, give the results that get closer to the experimental curves. In order to give an overview of the effect of porous distribution on the capturing process according to the model, in this paragraph some of the results obtained with others porous distributions are shown. It is worth to mention that changing the pore distribution experimentally may lead to a change in the pressure drop across the electrode, because the porous distribution influences the hydraulic resistance of the electrode. However, in this paragraph the results at various porous distribution are discussed at constant ΔP . Variation in R_h value will be taken into account in Sect 5.3.

k		1	2	3	4
R_p		2.4 nm	0.24 μm	4.7 μm	23.6 μm
Fig. 5.18 (a)	$f_{l,k}$	7e-4	0.8	0.1559	0.044
	N_k	2.3e9	2.6e8	12.6e4	1429
	$f_{q,k}$	1.38e-10	1.6e-3	0.124	0.875
Fig. 5.18 (b)	$f_{l,k}$	7e-4	0.624	0.34	0.0367
	N_k	2.3e9	2e8	27.5e4	1191
	$f_{q,k}$	1.38e-10	1.24e-3	0.27	0.729

Table 5.3: Pores numbers, liquid fractions and flow rate fractions used, for the results reported in Fig. 5.18.

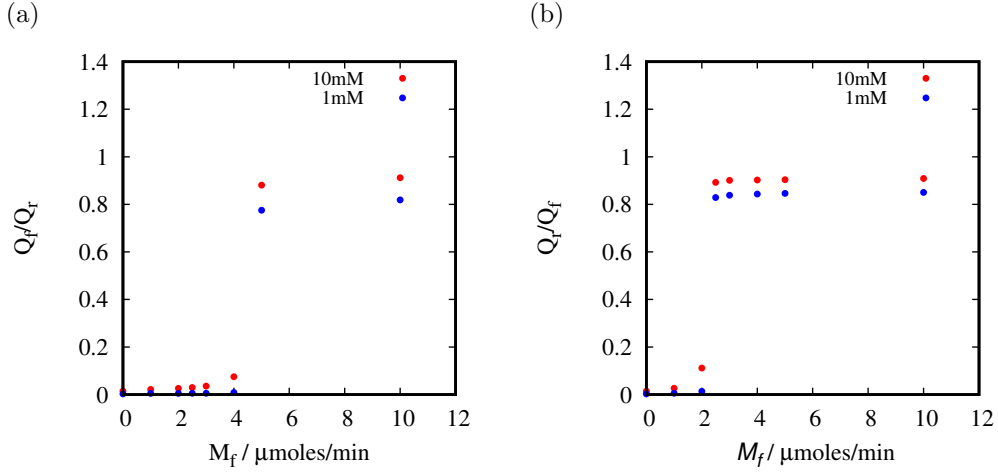


Figure 5.18: Q_f/Q_r vs. M_f calculated with parameters in Table 5.3.

Q_f/Q_r vs. M_f curves at 1 mA at the lowest and highest investigated concentrations (1 and 10 mM) are reported. Firstly, the results obtained by changing the pore distribution ($f_{l,k}$ and $R_{p,k}$) are reported, keeping constant the solid distribution. All the other parameters used in the previous simulations are the same.

In general, $R_{p,k}$ and $f_{l,k}$ must be changed always respecting the condition of Eq. 5.8, which fix the total flow rate equal to the experimental one. Moreover, $f_{l,k}$ values must always satisfy the equality $\sum f_{l,k} = 1$. The pores with higher $R_{p,k}$ ($k=3,4$) are crossed by most of the flow, so the equality of Eq. 5.8 mostly depends on their parameters.

In Fig. 5.18 (a) and (b) Q_f/Q_r vs. M_f curves are obtained with parameters reported in Table 5.3. For both cases $R_{p,3}$ is half of the value used in previous simulations (4.7 μm). By decreasing $R_{p,3}$, the flow rate in the pores decreases as well ($\Gamma_k \propto f_{l,k} R_{p,k}^2$),

k		1	2	3	4
R_p		2.4 nm	0.24 μm	9.4 μm	23.6 μm
Fig. 5.19 (a)	$f_{l,k}$	7e-4	0.9	0.06	0.0408
	N_k	2.3e9	2.9e8	12e5	1324
	$f_{q,k}$	1.4e-10	1.8e-3	0.188	0.81
Fig. 5.19 (b)	$f_{l,k}$	7e-4	0.739	0.25	0.0103
	N_k	2.3e9	2.4e8	50.7e3	333
	$f_{q,k}$	1.3e-10	1.47e-3	0.795	0.204

Table 5.4: Pores numbers, liquid fractions and flow rate fractions used, for the results reported in Fig. 5.19.

globally decreasing the total flow rate. Therefore $f_{l,k}$ values must be adjusted arbitrarily, so that Eq. 5.8 is satisfied.

The results reported in Fig. 5.18 (a) are evaluated with a $f_{l,3}$ value chosen so that $f_{q,3}$ is the 12.4% of the total (circa half of the previous one, which was 25%, as indicated in Table 5.2), and increasing the flow rate in the inactive pores $f_{q,4}$ up to 87.5%, respect to the previous value (74%). $f_{l,1}$ and $f_{l,2}$ values are approximately the same. Conversely, the curves in Fig. 5.18 (b) are calculated at higher $f_{q,3}$ (27%), while the flow rate in the inactive pores is reduced (73%). The two curves have a different shape with respect to results of previous paragraph. The curves of panel (a) reach the Q_f/Q_r saturation values at higher flow rate (5 $\mu\text{mol}/\text{min}$). This occurs because the fraction of flow rate ($f_{q,3}$) and the velocity ($v_{m,3}$) in the macropores are reduced, so the flow rate of reactant necessary to reach the maximum efficiency is higher. In panel (b), the situation is opposite, as $f_{q,3}$ is larger, and saturation flow rate is lower (2.5 $\mu\text{mol}/\text{min}$). In both cases, curve at 1 mM is closer to the curve at 10 mM. Although $R_{p,3}$ is lower, therefore a larger difference between 1 and 10 mM curves was expected due to diffusion effects, both $f_{l,3}$ and $N_{p,3}$ values are higher than in previous results, thus increasing the exchange area of the macropores $A_{s,3}$ ($= 2\pi R_{p,k} L_p N_k \propto f_{l,k}/R_{p,k}$), decreasing the local current (and consequently the overpotentials) and influencing positively the efficiencies also at low concentration. Summing up, according to the model, the trend of Q_f/Q_r with M_f depends mostly on the liquid and flow rates fractions in the macropores (active and inactive), as they are crossed by most of the electrolyte. Increasing the macropores exchange area, by enlarging the ratio $f_{l,3}/R_{p,3}$, improves the efficiency at low concentrations and at high flow rates.

Changing $R_{p,k}$ or $f_{l,k}$ of the small pores (k=1,2) while keeping constant the other parameters, does not lead to differences in the results. Particularly, two tests were carried out, the first at lower $R_{p,2}$ (10 and 50 times), the second at higher $f_{l,1}$ (up to 0.5)

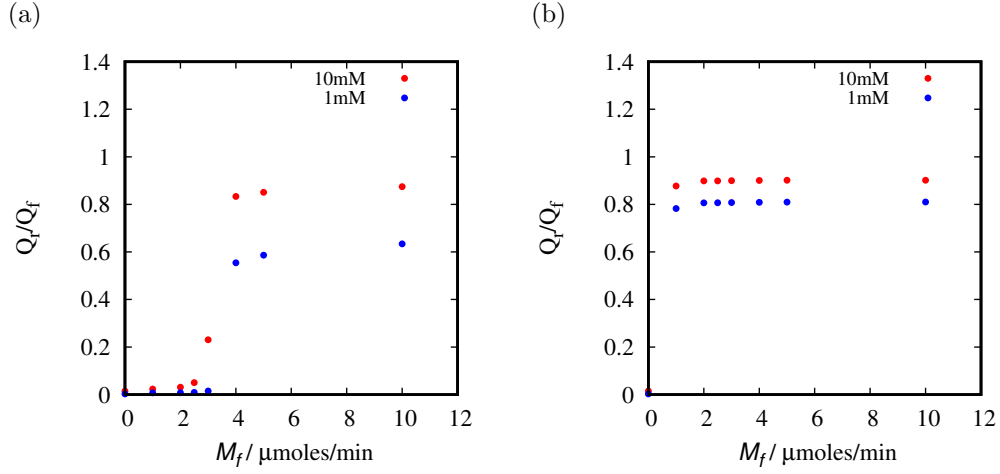


Figure 5.19: Q_f/Q_r vs. M_f calculated with parameters in Table 5.4.

by adjusting $f_{l,2}$ (0.3825). The total flow rate keeps almost equal, since it is barely influenced by the nanopores parameters. In both cases Q_f/Q_r curves are fairly the same of Fig. 5.14. Therefore increasing the quantity of nanopores, keeping constant the number of the macropores, has neither positive nor negative effect on the efficiency. They are crossed by too small flow rate and contain too low active material amount respect to macropores for playing a difference during the capturing.

Fig. 5.19 (a) shows the curve at higher $f_{l,2}$ and lower $f_{l,3}$ (Table 5.4). They show a higher saturation flow rate, due to the reduction of $q_{l,3}$ (18.8%). Q_f/Q_r curve at 1 mM LiCl is lower than the one of Fig. 5.18 (a), which was obtained at similar $q_{l,3}$, so it has similar saturation flow rate, but ten times higher $N_{p,3}$.

Finally, the curves of Fig. 5.19 (b) are obtained at higher $f_{l,3}$ and lower $f_{l,4}$ (Table 5.4). which leads to higher $f_{q,3}$ (80%), and lower $f_{q,4}$ (20%). For flow rates other than 0, the efficiencies for both concentrations are almost the maximum, due to the reduction of the inactive macropores.

In order to complete the investigation of the effect of porous distribution, the change of distribution of solid is performed, keeping $f_{l,k}$ and $R_{p,k}$ constant. Values of $f_{s,k}$ used are 5%, 42.5%, 42.5% and 5%, 80%, 15% for $f_{s,1}$, $f_{s,2}$ and $f_{s,3}$ respectively. Results are shown in Fig. 5.20. Decreasing the active solid on the macropores and increasing it in the micropores bring a decrease of the efficiency for both concentrations, while the difference between the two curves keeps approximately the same. Q_f/Q_r is always calculated with respect to the total charge obtained in 40 mM LiCl. This charge decreases as well for both distributions (79 and 44 mAh/g respectively, respect to the previous 136 mAh/g).

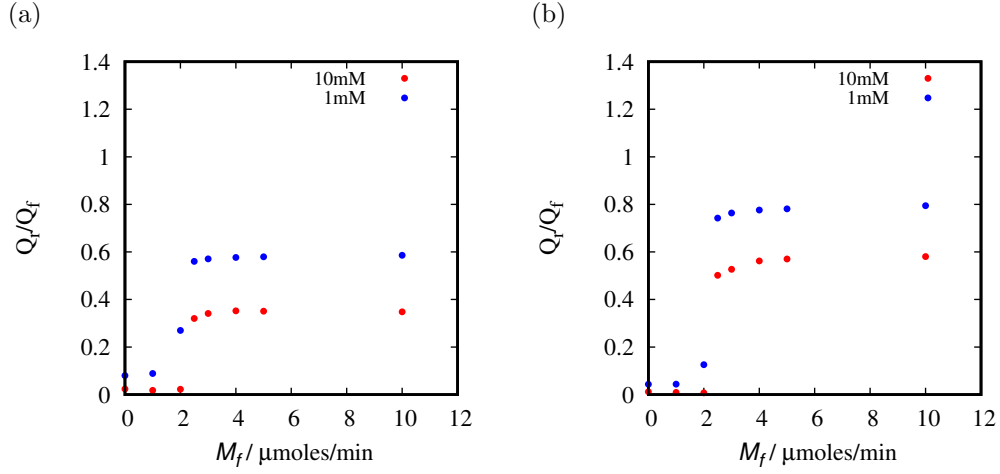


Figure 5.20: Q_f/Q_r vs. M_f at various solid distributions: 5%, 42.5%, 42.5% (panel (a)) and 5%, 80%, 15% (panel (b)) for $f_{s,1}$, $f_{s,2}$ and $f_{s,3}$ respectively.

According to the model, lowering the amount of solid of the biggest pores leads to a decrease of efficiency for all concentrations and flow rates.

Concluding, in this paragraph an overview of the effect of the electrode porous distribution on the capture efficiency has been shown.

The Q_f/Q_r trend with the flow rate depends mainly on the amount of the macropores (active or inactive), that are crossed by the highest amount of electrolyte. Saturation flow rate is higher by decreasing the flow rate in the active macropores. A high amount of nano- and micropores does not worsen the capture efficiency, if the macropores number is constant. Values of efficiencies are positively influenced by the increase of macropores exchange area $A_{s,3}$. Changes in solid distribution does not influence the concentration effect on the solid filling. The best solid distribution to get high efficiencies involves the highest amount of solid in the macropores.

5.2.9 Conclusion

In this Section, a mathematical model that describes the behavior of the flow-through electrodes cell was developed. An arbitrary pore distribution was used to simulate the effect of lithium concentration and flow rate on the capturing process.

Despite the simplicity of the model, the flow rate effect on the solid filling is well reproduced. As occurs experimentally, the active material does not totally participate to the reaction. This behavior is due to the diffusion effects along the electrode thickness, that are not balanced by the convective flow and that prevent the total filling of the

active material. The effect of the concentration on the maximum filling is well predicted for values of concentration ≥ 5 mM. At 1 mM and 2 mM, the maximum filling in the simulations is much higher than in the experiments. This is attributed to the ideal structure assumed in the model that does not fully represent the real structure of the porous electrode.

The analysis of the model results has revealed that the pore distribution has an influence on the solid filling and on the saturation flow rate. A pore distribution rich of active macropores leads to high capture efficiencies and low saturation flow rates. For this reason the pore size and the pore distribution should be experimentally controlled, together with the solid distribution of the active material on the substrate.

These results have been a hint for further investigations in order to improve the capture efficiency of the process. A first tentative is carried out trying to get a more compact active solid layer on the substrate, more similar to the ideal structure of the model. This is performed increasing the mass loading on the LMO electrode, as reported in the next Section.

5.3 Effect of mass loading

In this Section the effect of mass loading of the active material on LMO electrode is discussed.

The higher capture efficiencies predicted by the model at low concentrations suggest the possibility to improve the process performance by using an electrode structure more similar to the one assumed in the model. One of the hypothesis made in the model is the presence of 9.4 μm radius pores formed by the 80% of active material. According to the model results, lithium is mostly captured by these pores at all the concentrations. The effect of these pores translates in the real system into a solid active part that forms a distribution of macropores abundantly crossed by the flux. Hence a more compact structure with big active channels, more similar to the ideal one, can improve the cell performances at low concentration.

In order to improve the solid distribution, the electrodes are loaded 3 times more with LMO slurry, painting 14 mg/cm^2 of active material, instead of 5 mg/cm^2 . The experiments are repeated 3 times with 3 different electrodes, at the same brine concentrations (1, 2, 5 and 10 mM of LiCl and 100 mM NaCl) and current (1 mA), using two short-circuited NiHCF electrodes with 35 mg/cm^2 active material as a counter, to balance the charge of LMO.

The SEM image of the higher mass loading electrode is shown in Fig. 5.21. The structure is very different from the lower mass loaded electrode (Fig. 5.6). The active material forms a compact and solid layer, filling more the carbon cloth fibers and leading to a structure more similar to the one hypothesized in the model.

In Fig. 5.22, GCPL curves obtained at high flow (10 $\mu\text{mol}/\text{min}$) with 5 mg/cm^2 (panel (a)) and 14 mg/cm^2 (panel (b)) mass loaded electrodes are reported. Q_f/Q_r increases with the mass loading at all the concentrations. This positive effect of the mass loading is higher at low concentration (1-2 mM) and it becomes negligible at higher concentrations. Moreover, the two inflection points in the potential profile of LMO material at high mass loading are more visible at 1 and 2 mM, indicating that the totally filled solid part is larger.

In Fig. 5.23, Q_f/Q_r vs. M_f (panel (a)) and the mean overpotential $\bar{\eta}$ vs. M_f (panel (b)) are reported for all the investigated concentrations. The shape of the curves is equal to the one obtained at lower mass loading, with a linear increase ending with a saturation. The curve at 10 mM of LiCl is not much different from the one at lower mass loading, namely at this concentration the structure of the electrode does not influence considerably the efficiency. By decreasing the concentration, the improvement of the capture efficiency becomes relevant. Q_f/Q_r saturation values passes from 0.2 to 0.7 for 1 mM, from 0.4 to 0.8 at 2 mM, from 0.75 to 0.9 at 5 mM and from 0.9 to 1 at 10 mM. The same discussion

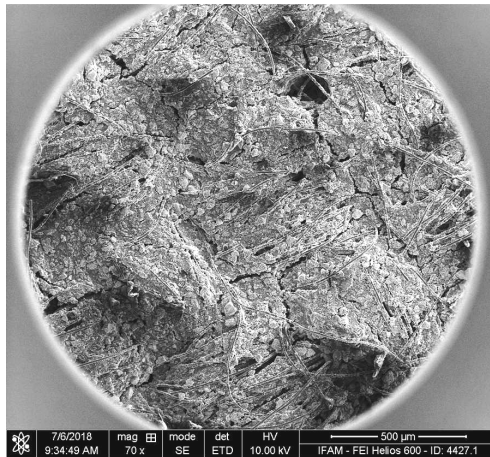


Figure 5.21: SEM image of the LMO electrode loaded at 14 mg/cm^2 of active material. Dr. Jenz Glenneberg of IFAM institute is greatly acknowledged for having provided these images.

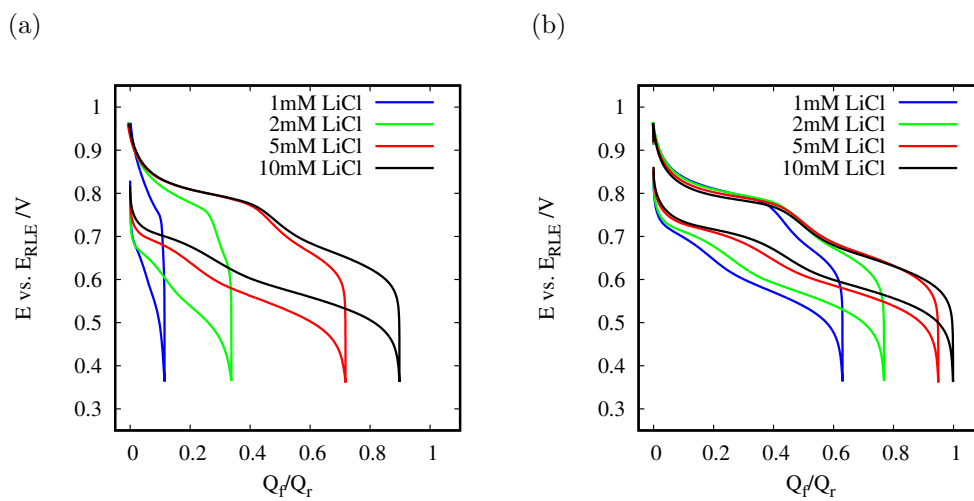


Figure 5.22: Galvanostatic charge at various concentrations and $M_f=10 \text{ } \mu\text{mol/min}$, for low mass loading (panel (a)) and high mass loading (panel (b)).

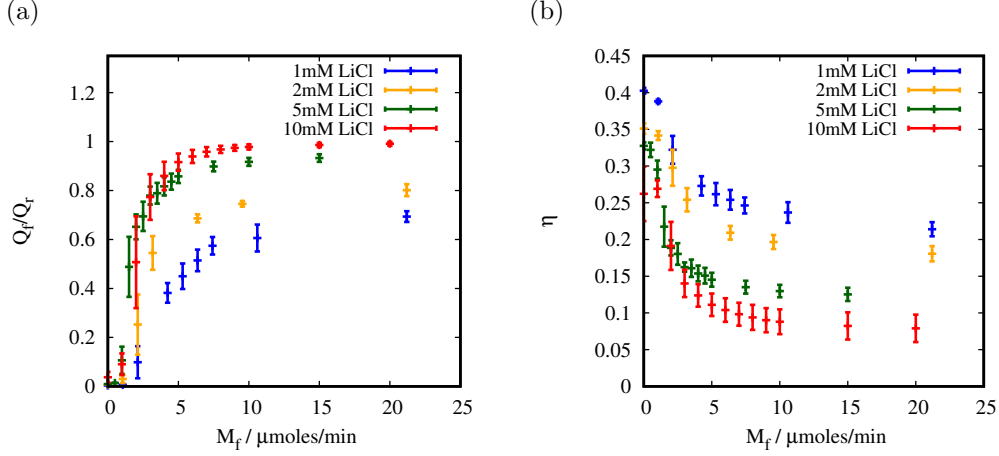


Figure 5.23: Panel (a): maximum solid filling of LiMn_2O_4 ; panel (b): mean overpotential obtained with the high mass loaded electrode; both quantities are reported vs. the molar flow rate of the electrolyte at various concentrations of LiCl.

is valid for $\bar{\eta}$, that is shifted to lower values at 1 and 2 mM with respect to the lower mass loaded electrode (see Fig. 5.5 panel (b)).

The value of M_s extracted through the exponential function from Fig. 5.23 (a) are equal to 18.3, 12.5, 6.6 and 6.4 $\mu\text{mol}/\text{min}$ at 1, 2, 5 and 10 mM respectively. The M_s values are double than M_s values evaluated at lower mass loading for all concentrations. According to the model (Sect. 5.2.8), an increase of the saturation flow rate is due to a shifting of the porous distribution towards smaller pore sizes, which it translates into a decrease of the flow rate across the active macropores. This change in the structure is attributed to the increase in mass loading. Indeed, on one side the carbon cloth is better filled of the active material, namely there are more active pores and less inactive macropores with respect to the low mass loaded structure. This increases the efficiency at low concentrations. On the other side, the increase in mass loading leads to a more compact active material layer, that is made by narrower channel. This causes a decrease of velocity inside the porous matrix and a consequent increase of the saturation flow rate.

This can be explained also by means of the Darcy law, which expresses the mean velocity in a porous medium through its permeability K_Γ :

$$\bar{v} = \frac{K_\Gamma}{\mu} \frac{\Delta P}{L} \quad (5.42)$$

K_Γ is a characteristic of the medium type. Generally, it increases with the medium porosity and with the pore size [116, 117]. By increasing the mass loading, the porosity decreases, as well as the average porous distribution size, leading to lower permeability

Group number k	1	2	3	4
R_p	2.4 nm	0.24 μm	4.2 μm	23.6 μm
$f_{l,k}$	0.0307	0.9	0.06	0.0093
N_k	8.8e10	2.6e8	5.4e4	268
$f_{s,k}$	0.05	0.15	0.8	0
$f_{q,k}$	2.7e-8	0.008	0.17	0.822

Table 5.5: Pores numbers, liquid fractions, solid fractions and flow rate fractions for various pores sizes assumed for the high mass loaded electrode.

and lower mean velocity. By rewriting the hydraulic resistance by means of the Darcy law, expressing the flow rate Γ as $\bar{v}A_e f_l$, one obtains:

$$R_h = \frac{\mu L}{A_e f_l K_\Gamma} \quad (5.43)$$

The decrease of K_Γ and of the porosity f_l leads to higher hydraulic resistance. This is confirmed by pressure measurements performed on the high mass loaded electrode, reported in Sect. 5.6. R_h value for 14 mg/cm² mass loaded electrode is 5 times higher than the one of the 5 mg/cm² mass loaded electrode.

Simulations at the various concentrations and molar flow rates were repeated modifying opportunely the parameters for the high mass loaded electrode. The solid fraction f_s calculated from the new mass loading (14 mg/cm²) is 0.085, and the electrode porosity f_l is decreased down to 0.445. The value of R_h used in the simulations was extrapolated experimentally (1.5 mbar min/ml, as reported in Sect. 5.6). The pore distribution parameters are reported in Table 5.5.

A pore distribution richer of smaller pores with respect to the distribution of the lower mass loaded electrode was hypothesized. $R_{p,1}$ and $R_{p,2}$ were kept constant, while $R_{p,3}$ was decreased ≈ 2.2 times. $f_{l,2}$ was increased from 0.8818 to 0.9 and $f_{l,3}$ is reduced from 0.08 down to 0.06.

The increase of ΔP that occurs experimentally is mainly due to the decrease in the number of inactive large pores, due to the higher filling of the substrate. $f_{l,4}$ was therefore reduced, adjusted to satisfy Eq. 5.8.

The curves Q_f/Q_r vs. M_f for the four concentrations are reported in Fig. 5.24. By comparing these curves with the ones obtained with parameters of the lower mass loaded electrode (Fig. 5.14 (a)), the increase of the saturation flow rate can be noted. This confirms that the model describes the effect of the permeability reduction of the higher mass loaded electrode, by using a pore distribution richer of smaller pores.

The shape of the curve at 10 mM LiCl describes approximately the experimental curve

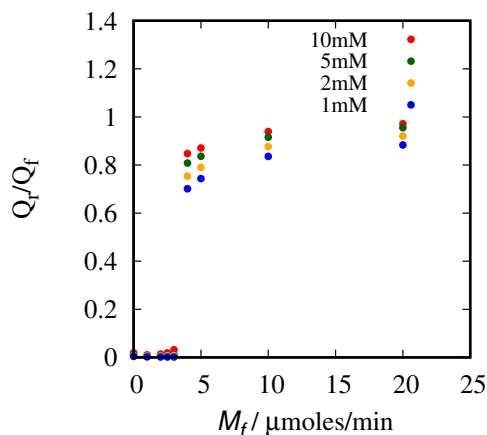


Figure 5.24: Q_f/Q_r vs. M_f extracted from the simulated galvanostatic curves at 1,2,5 and 10 mM of LiCl for the 14 mg/cm² loaded electrode.

reported in Fig. 5.23. Both curves arrives to the total maximum charge ($Q_f/Q_r \approx 1$) and the saturation flow rate is circa 6 $\mu\text{moles}/\text{min}$. At the other concentrations the simulated curves have the same trend. The lowering of Q_f/Q_r values at lower concentration is reduced with respect to the one simulated for the low mass loaded electrode (Fig. 5.14 (a)). This is caused by the increment of ΔP , which leads to higher velocity in the 2.4 nm and 0.24 μm pores, and by the increase of the exchange area $A_{s,3} \propto f_{l,3}/R_{p,3}$, which decreases the overpotentials.

The model and the experimental results for high mass loaded electrode (Fig. 5.24 and Fig. 5.23 (a) respectively) have some discrepancies. Firstly, the capture efficiencies predicted by the model at concentrations lower than 5 mM are higher than the experimental ones; secondly, the variation of M_s with the concentration is not predicted by the model. These differences may be due to diffusive effects not included in the model. Indeed, only the diffusion effects occurring along the thickness of the electrode are included. In the real situation, lithium transport along other directions may count, such as radial or inter-porous transport. The error in the efficiencies at high flow rates for the lowest concentration (1 mM) is $\approx 20\%$, which can be considered acceptable for a rough estimation of the capture efficiency.

Summarizing, it was demonstrated experimentally that capturing with a higher mass loaded electrode leads to a large improvement of the capture efficiency at low concentrations. This is attributed to a more compact structure with a better porous distribution. The active material fills more the inactive macropores of the carbon cloth, leading to a

more compact distribution, richer of active pores. The higher mass loading on the electrode improves the transport of lithium along the pores, meanwhile leading to an increase of pressure drop.

Beside, it was shown that the mathematical model qualitatively describes the experimental results obtained with the higher mass loaded electrode, by modifying opportunely the pressure on the electrode and the porous distribution parameters.

The use of an high mass loaded electrode has another important advantage, namely it allows to capture a larger amount of lithium per cycle. This translates not only into a higher lithium concentration in the recovery solution, but also into a higher reduction of the lithium concentration in solution during the capture.

Until now, the aim of the experiments was to investigate the limit of capture given by the solid filling. The experiments were therefore performed at almost constant inlet brine concentration, namely the volume pumped during the capture contains an amount of lithium much higher than the quantity that the electrode can ideally contain.

In an industrial application of the reactor, given the same amount of captured lithium, pumping continuously fresh brine to the reactor has much higher costs of pre-treatment and hydraulic energy than depleting completely a certain volume of brine. On these grounds, once known the efficiency limit on the solid filling, it is interesting to investigate also on the yield of the process, defined as the lithium concentration reduction in solution during the capturing step. In the next paragraph this investigation is carried out at various applied currents.

5.4 Effect of current

Once found the conditions for the optimal solid filling, the investigation of process yield is carried out at various currents. It has been already proved that by decreasing the applied current, the process efficiency increases [6], due to the overpotential reduction.

The experiments have been performed using a 14 mg/cm^2 mass loaded electrode at 1 mM LiCl and 100 mM NaCl , pumping 40 ml of solution into the cell during the reaction.

GCPL measurements have been carried out at $1, 0.5$ and 0.2 mA in the flow rate range $0\text{-}20 \text{ }\mu\text{mol/min}$. Fig. 5.25 shows the galvanostatic curves at each investigated current, at low flow rate ($2.1 \text{ }\mu\text{mol/min}$, panel (a)) and at a high flow rate ($21.2 \text{ }\mu\text{mol/min}$, panel (b)). At higher flow rate, the reduction charge is larger than at lower flow rate, due to the higher flux. As expected, the positive effect of the flow rate is larger at 1 mA , while it is almost negligible at 0.2 mA . Indeed, the lower is the current, the lower is the mass transport overpotential.

The current effect becomes clearer representing Q_f/Q_r and $\bar{\eta}$ vs. M_f (Figs. 5.26 and

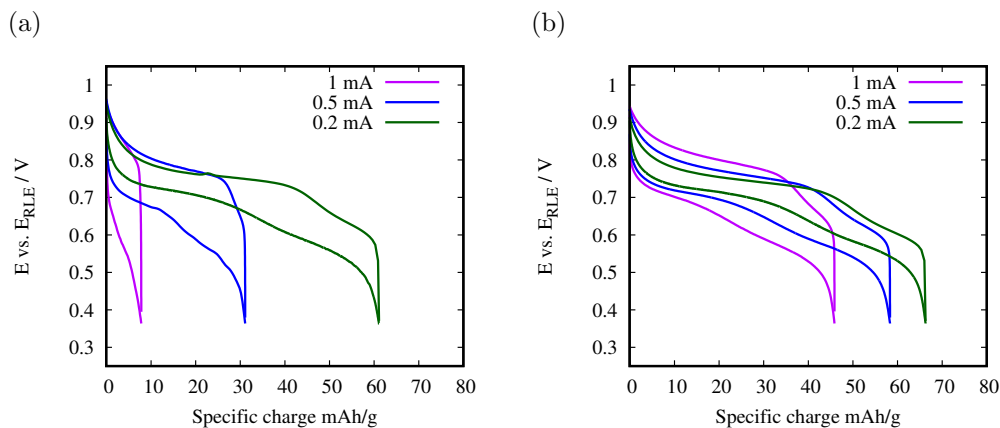


Figure 5.25: Galvanostatic curves at 0.2, 0.5, 1 mA at low molar flow rate ($2.1 \mu\text{mol}/\text{min}$, (a)) and at high flow rate ($21.2 \mu\text{mol}/\text{min}$, (b)).

5.27 respectively). The curves follow the well-known trend: Q_f/Q_r increases linearly and then it reaches a saturation value, $\bar{\eta}$ follows the opposite trend.

At $M_f=1 \mu\text{mol}/\text{min}$, Q_f/Q_r is very different for the three currents. This can be explained considering the capturing rates in each case. At 1 mA, 0.5 mA and 0.2 mA, the rates of lithium capturing are 0.62, 0.31 and $0.12 \mu\text{mol}/\text{min}$ respectively. Hence while at 1 mA the flowing-through lithium ions amount is just enough to compensate the capturing rate, at the lowest current M_f is much larger than the rate of capturing, so that the lithium ions amount is no more a limitation for the process.

More in general, at all the flow rates Q_f/Q_r is larger at lower current, due to the vanishing of the diffusion overpotential.

In the secondary axis of Fig. 5.26, the yield of the process is reported. It is calculated as the ratio between the amount of captured lithium (evaluated from the circulated charge) and the total amount of lithium in the solution (0.04 mmoles). The yield increases by increasing the flow rate and decreasing the current, reaching 62% at 1 mA, 85% at 0.5 mA and 98% at 0.2 mA.

Saturation flow rates values also change with the current. They are estimated from curves of Fig. 5.26 through the fitting with the exponential function, as already reported in Sect. 5.1. M_s values obtained are 2.4, 9.2 and $22.4 \mu\text{mol}/\text{min}$, for 0.2, 0.5 and 1 mA respectively. The lower is the current, the lower is the flow rate that must be applied to reach the maximum efficiency. This is due to the positive effect of the current decrease on the mass transport overpotential, that reduces the influence of the flow rate on the capture. Hence the process reaches high efficiencies at lower pressures, and the required hydraulic energy is reduced. This aspect will be further discussed in Sect. 5.6. On the

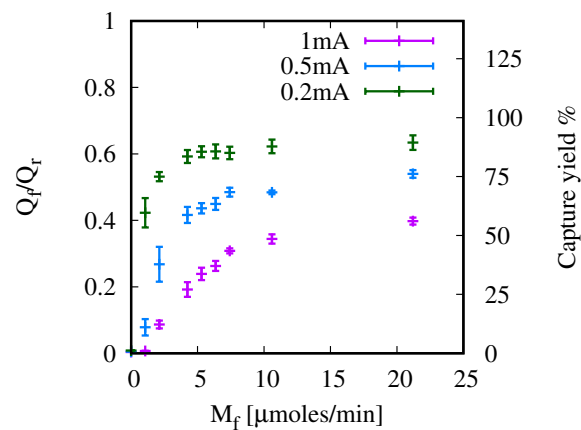


Figure 5.26: Q_f/Q_r at various currents and flow rates (primary axis) and yield of the capturing process (secondary axis) evaluated as the ratio between the amount of captured lithium and the amount of lithium in solution before the start of the process.

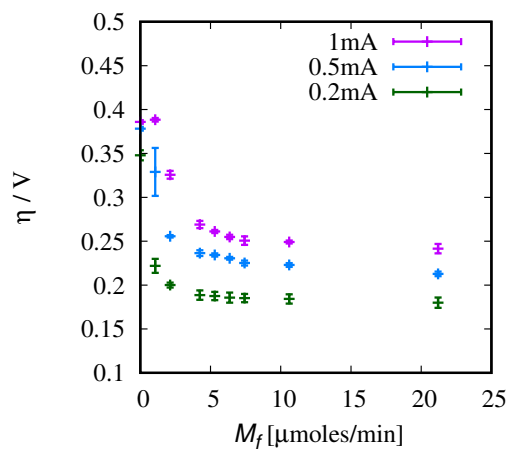


Figure 5.27: Mean overpotential vs. molar flow rate M_f at different currents.

other hand, the decrease of current leads to an increase of the operation time, 5 times higher at 0.2 mA than at 1 mA.

It is worth to notice that the M_f values in these measurements are not constant during the experiments, but they decrease, due to the inlet solution concentration reduction. The values reported in the graph are the starting values of M_f , therefore they are overestimated with respect to the real values during the capturing. The flux must compensate not only the diffusion overpotential due to the lithium depletion in the pores, but also the bulk concentration reduction. This explains why M_s at 1 mA ($22 \mu\text{mol}/\text{min}$) is 20% higher than M_s obtained in the previous experiments at 1 mM LiCl and 1 mA ($18 \mu\text{mol}/\text{min}$), run at constant concentration of the inlet solution.

Concluding, in this Section it has been demonstrated that the capturing process reaches more than 90% yield by lowering the current. The current is an important operative parameter, that can be chosen as trade-off between the capture yield, the hydraulic energy and the operation time.

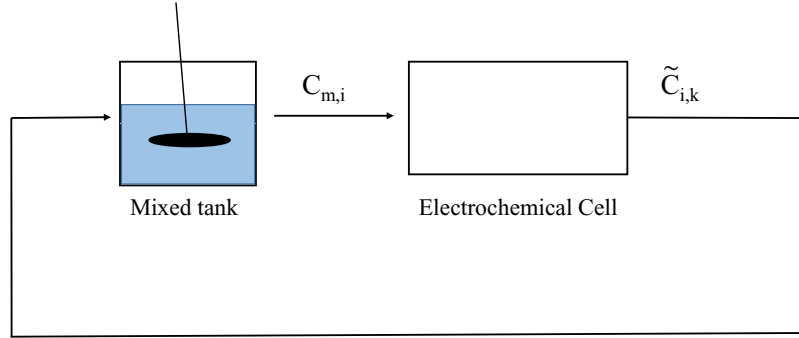


Figure 5.28: Flow sheet of the capturing process.

5.5 Model results at various currents

In the last Section, it has been shown that the current is a fundamental parameter of the process. By regulating the current, the yield of the capture can be increased, while saving hydraulic energy. Hence it is useful to demonstrate that the mathematical model developed in Section 5.2 predicts the behavior of the system at various currents.

In order to simulate the experiments of Fig. 5.26, the concentration reduction of the source solution must be taken in account. In the model presented in Section 5.2, the solution entering into the cell is always fresh, with a concentration equal to the starting one. This assumption works when the charge circulated into the cell is much smaller than the amount of lithium cations present in the liquid. In this case, the concentration reduction of the total liquid flowing into the cell is negligible and a fixed brine concentration of the fed solution can be used in the model to simulate the results. When the amount of lithium in the liquid is lower or comparable to the amount that can be stored in the electrode, the concentration depletion of the liquid pumped from the feeding tank into the cell must be taken into account.

5.5.1 Integration of the feeding tank in the model

In order to consider the concentration reduction of the inlet solution, the feeding tank must be added into the model.

The solution is pumped from the tank to the cell. The solution going out from the reactor, depleted in lithium concentration, goes back into the tank, as shown in Fig. 5.28. The tank is supposed to be perfectly mixed, so that its bulk concentration inside is equal to the outgoing one. The liquid is then recirculated in the reactor at lower concentrations upon time. The process could ideally continue until the lithium in the tank is completely exhausted.

A further equation is added to the equation system reported in Sect. 5.2. It is a mass balance equation of the reacting species in solution (lithium and sodium ions) on the feeding tank and it has the following form:

$$A_m \left[\sum_k \tilde{C}_{i,k} v_{m,k} f_{l,k} - \sum_k C_{m,i} v_{m,k} f_{l,k} \right] = V_{mix} \frac{dC_{m,i}}{dt} \quad (5.44)$$

In the left side, the first term represents the incoming mass in the tank, equal to the outgoing mass from the cell. $\tilde{C}_{i,k}$ is the concentration downstream of the reactor for each channel group. For $k=4$, representing the inactive carbon cloth pores, $\tilde{C}_{i,k} = C_m$. Indeed, in these pores, the fluid is pumped from the tank and pass through the cell without varying its concentration, as no reaction occurs. The term on the right side of the equation is the accumulation term. V_{mix} is the tank volume, A_m is the total fluid passage section of the electrode, evaluated as $f_l \pi R_e^2$.

By solving the equation, the variation of species concentration in the tank ($C_{m,i}$) upon time is obtained.

To add this equation, the boundary condition of point 1 (Fig. 5.10) is modified. The Neumann condition on the diffusive fluxes equal to zero is substituted with a Dirichlet boundary condition on the concentration, imposing $C_{i,k} = C_{m,i}$.

5.5.2 Analysis of results

Simulations are performed at different currents (1, 0.5 and 0.2 mA), at 1 mM of LiCl and 1 M of NaCl concentrations, using porous distribution parameters of both low and high mass loaded electrodes (reported in Table 5.2 and Table 5.5 respectively). The V_{mix} values used in the simulations have been chosen so that the ratio between the amount of lithium in solution and the amount that can be captured by the electrode in the best conditions (40 mM LiCl) is equal to the experimental one (≈ 0.6). V_{mix} values are therefore 17.5 and 50 ml for the low and for the high mass loaded electrode respectively.

In Fig. 5.29, Q_f/Q_r values vs. M_f are reported for each current, extracted from the simulated curves, for the low mass loaded electrode (a) and the high mass loaded electrode (b). The experimental trend of Q_f/Q_r with the current and with the molar flow rate (reported in Fig. 5.26) is well reproduced. The shapes of the curves calculated at different mass loadings are similar, namely the model reproduces the effect of the current for both porous distributions and pressure drops. With the higher mass loaded electrode, the curves have higher saturation flow rates, as expected from the lower permeability of the electrode.

In Fig. 5.30 the galvanostatic curves at low flow rate (2.5 $\mu\text{mol}/\text{min}$) and high flow rate (10 $\mu\text{mol}/\text{min}$) are reported for each investigated current. The model reproduces the effect of current and flow rate on the galvanostatic curves. By decreasing the current,

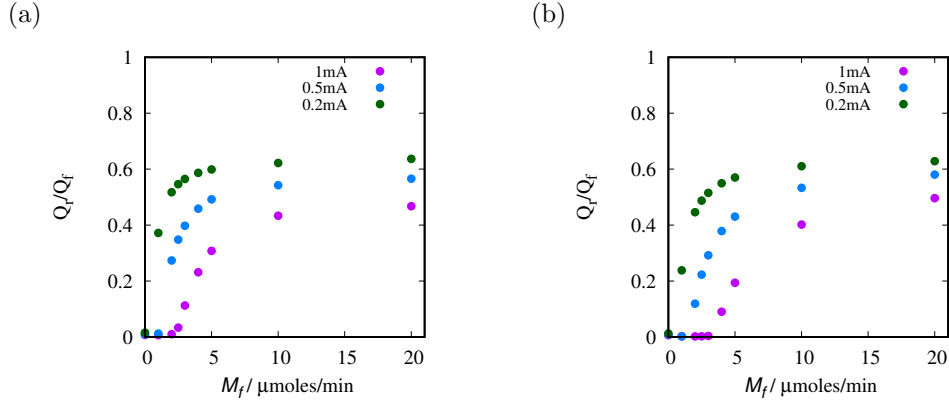


Figure 5.29: Q_f/Q_r vs. M_f extracted from the simulated galvanostatic curves at different currents for 5 mg/cm^2 mass loading (a) and 14 mg/cm^2 mass loading (b).

the curves reduction branches occur at higher potential, namely capture overpotentials decrease, like in the experimental curves of Fig. 5.25. The same occurs with less intensity during the release, as the potential of the oxidation branches decreases at lower current. As already observed experimentally, the positive effect of the flow rate on Q_f is large at 1 mA and almost negligible for 0.2 mA.

The inflection points of LMO profile potential are almost absent in the curves. They are slightly visible at the lowest current. As previously discussed, the two inflection points are present when some solid parts are completely filled, reaching the maximum state of charge. These solid parts form those pores abundantly crossed by the flow. In the model the solid distribution is a simplification of the real system. The active material that mainly participates to the capture (which is assumed to be 80% of the total solid) forms the biggest pores and it is described as a “slab” that fills as a unique block. According to the simulated galvanostatic curves of Fig. 5.30, it does not fill completely, due to the lack of lithium in solution. Conversely in the real system, the porous distribution is much more complex and diversified, namely the active material is distributed in form of particles in macropores of various sizes. These particles fills independently from each other and some of them reaches the maximum state of charge, giving rise to the characteristic shape of the LMO material.

In Fig. 5.31, time variation of the tank concentration is reported for the three currents at high flow rates. The concentration changes linearly in time, as expected at constant current. The concentration reduction increases by decreasing the current, up to 95% at 0.2 mA, which is close to the maximum yield found experimentally.

Concluding, by adding the mass balance equation on the feeding tank, the model

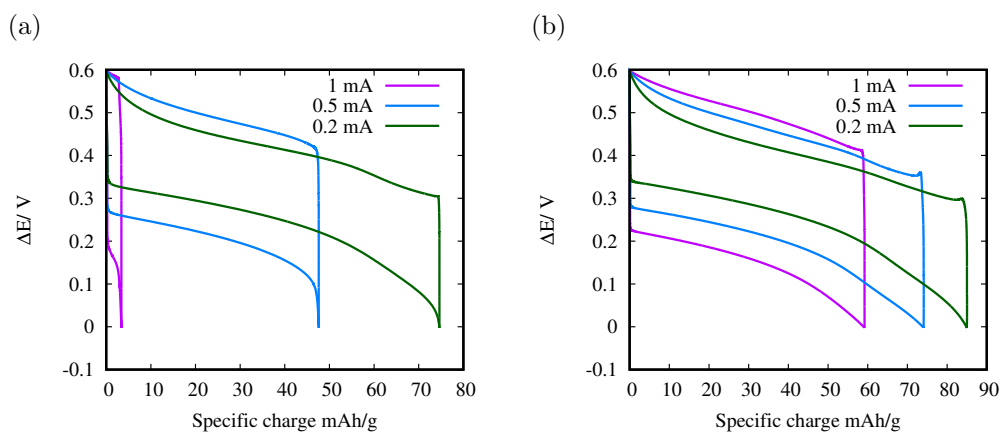


Figure 5.30: Galvostatic curves simulated at different currents at low flow rate ($2.5 \mu\text{mol}/\text{min}$, (a)) and high flow rate ($10 \mu\text{mol}/\text{min}$, (b)) for the low mass loaded electrodes.

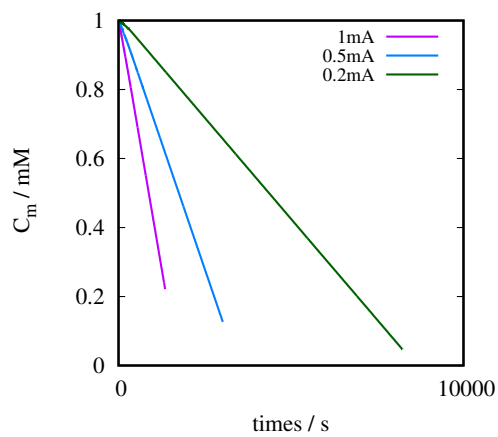


Figure 5.31: Concentration in the mixer vs. reaction time.

describes very well the electrochemical system behavior at various currents, for a given lithium concentration brine. By knowing the electrode pressure drops and by choosing a porous distribution roughly representing the real one, the capture yield and the saturation flow rate of the process can be estimated at various currents.

In this Chapter, it has been shown how the proposed mathematical model describes the solid maximum filling at various flow rates, concentrations and electrode pressure drop, with a good precision for lithium concentrations ≥ 5 mM. The validity of the model has been further confirmed by the results at various currents. By decreasing the current, the capture yield of the process increases, meanwhile decreasing the saturation flow rate, as occurs experimentally. This latter is a very important parameter, because it determines the hydraulic energy required by the system, as it will be shown in the next Section. Concluding, by choosing the right parameters of the electrode porous distribution, the model qualitatively reproduces the system behavior at various process conditions and it can be used to estimate the best reactor working point, finding the trade-off between the various parameters (current, flow rate, brine volume, pressure drop, mass loading).

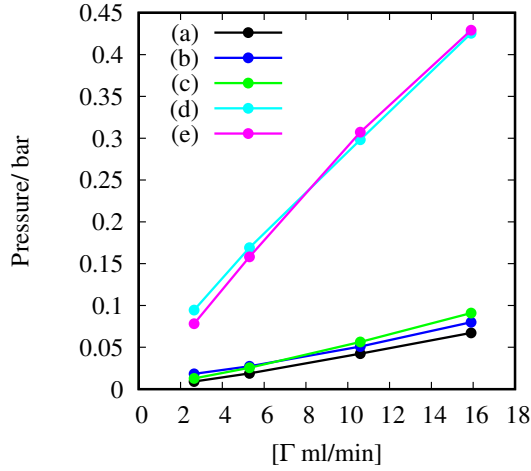


Figure 5.32: Pressures vs. volumetric flow rate for the empty cell (a), for the cell with the 5 mg/cm² loaded electrode (b), with the 14 mg/cm² loaded electrode (c), with the first electrodes stack (low mass loaded LMO and one NiHCF electrode) (d), with the second electrodes stack (high mass loaded LMO and two NiHCF short-circuited electrodes) (e).

5.6 Pumping energy

The evaluation of pumping energy is important to estimate the operational costs of the process. The pressure drop on the cell has been experimentally evaluated. Firstly, an evaluation of the Reynolds number Re can be useful to know the flow type inside the cell. Reynolds number is evaluated in the narrowest part of the cell, namely the tube before the funnel-shaped hole that has a diameter of 2 mm. It is calculated as:

$$Re = \frac{4\rho\Gamma}{\pi d\mu} \quad (5.45)$$

where ρ is the solution density, Γ is the volumetric flow, d is the diameter and μ is the viscosity of the solution. Using the value of the highest flow rate used during the experiments (50 ml/min), the obtained value is 530 (< 1000), namely the flow is laminar. Therefore, a linear behavior of the pressure with the flow rate is expected. Various measurements have been performed on single elements of the cell. The pressure values are reported in Fig. 5.32 vs. the volumetric flow rate. The trend of the curves is linear, confirming that the flow is laminar into the cell. The slopes of the lines have been evaluated through a linear regression and they indicate the hydraulic resistance of each configuration.

The line (a) is the pressure on the empty cell (without any electrode). The line (b) instead was measured adding only the low mass loaded LMO electrode. The slopes of

the (a) and (b) are very close (4.4 and 4.7 mbar min/ml). Considering the hydraulic resistances of the cell and of the electrodes as resistances in series, the low mass loaded electrode resistance can be estimated as a difference between the two values (0.3 mbar min/ml).

The resistance of the high mass loaded electrode (extracted from line (c)) is 5 times higher than the low mass loaded one, thus the mass loading has an effect on the pressure drop. The increase of pressure is due to the decrease of the porosity and permeability, occurring for the higher filling of the substrate fibers of active material.

Adding the counter electrode and the separator (lines (d)), the hydraulic resistance is much higher (25 mbar min/ml), thus suggesting that the highest pressure drop of the cell are due to the NiHCF electrode, loaded at 25-30 mg/cm².

Furthermore, adding the second NiHCF electrode into the cell (line (e)) seems to have no effect on the hydraulic resistance. This result suggests that the fluid, after crossing LMO electrode, does not cross the NiHCF electrodes, probably choosing a lower pressure alternative path, outside the active area. This explains why the hydraulic resistance is much higher respect to the other cases and it does not depend on the number of NiHCF electrodes. This behavior of the flow is allowed by the cell geometry that has a volume much larger than the active material volume. This configuration defect is solved with the new cell geometry, as reported in Sect. 3.2.2.

The hydraulic resistance can be used to get a first evaluation of the pumping energy required for the process.

The energy required to capture a mole of lithium can be expressed as:

$$E_h = \frac{R_h \Gamma_s^2 t_r}{m_{Li}} \quad (5.46)$$

where t_r is the capturing time, R_h is the hydraulic resistance of the cell (containing WE, CE and separators), m_{Li} is the amount of captured Li⁺ moles and Γ_s is the saturation flow rate. For $\Gamma > \Gamma_s$, the increase of the captured lithium is not high enough to justify the increase in hydraulic energy. Knowing that $m_{Li} = Q_f/F$ and $t_r = Q_f/I$, the hydraulic energy can be rewritten as follows:

$$E_h = \frac{R_h \Gamma_s^2 F}{I} \quad (5.47)$$

E_h depends quadratically by volumetric flow rate, it is directly proportional to R_h and inversely proportional to I .

In this phase, only pumping power required for the capturing step is taken into account, since it is higher than the one for recovery, as it will be discussed in Chapter 6. It is interesting to show the dependence of capturing hydraulic energy on some process parameters.

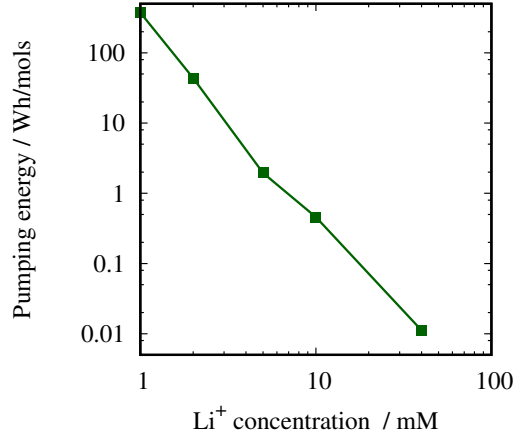


Figure 5.33: Pumping energy per mole required during the capturing process vs. the lithium concentration in source solution.

In Fig. 5.33, the molar hydraulic energy is reported vs. the brine concentration. It is calculated using the evaluated molar saturation flow rates for the various concentrations from the experiments reported in Fig. 5.23. As expected, the pumping energy decreases with lithium concentration. This behavior is due to the volumetric flow rate, which is inversely proportional to the concentration ($\Gamma_s = M_s / C_{Li}$). This dependence translates in a quadratic trend of the hydraulic energy with the concentration (Eq. 5.47). By increasing $C_{Li} \rightarrow 0$. A smaller effect is due also to M_s , which decreases for higher concentrations.

Pumping energy depends also on applied current. According to Eq. 5.47, the hydraulic energy decreases proportionally with current. Nevertheless, M_s and consequently Γ_s decrease with the current, as observed in Sect. 5.4. Using M_s values extrapolated by Fig. 5.26, the correspondent pumping energy at the three different investigated currents are calculated and reported in Fig. 5.34. Thanks to the decrease of Γ_s , the pumping energy decreases with the current.

In the same graph, the relative cost of pumping is reported, evaluated as the ratio between the cost of electricity due to the pumping (0.097 Euro/kWh, considering a medium size industrial plant located in Germany [118]) and the price of produced lithium (evaluated from the current price of Li_2CO_3 , 20 Euro/kg [12]). Even at the highest investigated current, the pumping costs are the 7% of the income, which means that the process is economically sustainable at the investigated conditions. The energy costs can be further reduced by decreasing the current.

The operational costs of the process include also the required electric energy due to

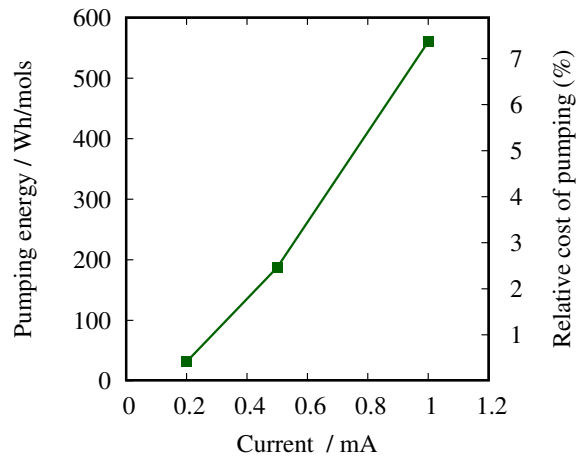


Figure 5.34: Pumping energy per mole required during the capturing process (primary axis) vs. the current. The cost of pumping is reported in the secondary axis, in percentage with respect to the process income.

the current. In Chapter 6, this cost will be included in the evaluation and it will be shown that for low brine concentration (less than 5 mM) the required electric energy is negligible compared to the pumping energy.

Concluding, pumping energy depends on the cell hydraulic resistance, saturation flow rate, brine concentration and applied current. The hydraulic resistance depends on the mass loading of the electrode and on its porosity. A way to decrease R_h is to tailor the porous distribution of the electrode. A structure with low amount of active material and many big inactive pores leads to a lower R_h value, but also to low capture efficiency. Filling more the substrate with active material increases R_h , but it is necessary to have a good yield of the process.

The other determining factor is the brine concentration. At low concentrated brine, pumping energy cost is the highest operational cost. Nevertheless, hydraulic energy can be controlled by tuning the current. Decreasing the current, namely slowing down the capturing rate, leads to a decrease of the saturation flow rate and in a optimization of the costs. The current value can be chosen as a trade-off between the pumping cost and the time production.

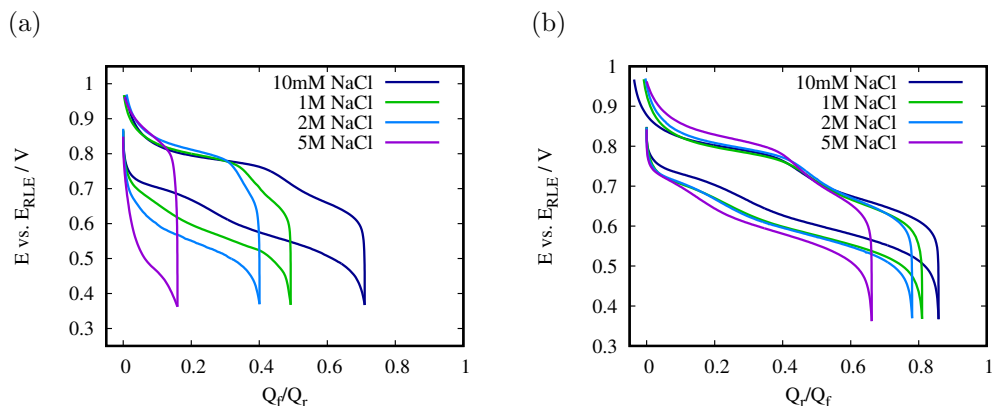


Figure 5.35: Galvanostatic curves of LiMn_2O_4 in 10 mM, 1, 2 and 5 M NaCl and 5 mM of LiCl, at 0.4 (a) and 2 ml/min (b) [64].

5.7 Effect of sodium concentration

Lithium brines contain many other cations, such as Mg^{2+} , Ca^+ , K^+ , Na^+ and so on. Selectivity of LMO towards lithium have been extensively studied in the past [6, 34]. Trócoli et al. [6] reported that the coefficient of lithium selectivity, defined as the ratio between amount of lithium and other cations in the recovery solution, is circa 35 for K^+ , Na^+ and more than 300 for Mg^{2+} .

Nevertheless, the good selectivity of LMO does not prevent the other cations to influence lithium intercalation. A previous study [8] has shown that the presence of sodium can interfere in the capturing step, limiting the amount of lithium intercalated. This phenomenon is very important for lithium capturing from natural brine, since most of them contain sodium cations at high concentration. In order to have a quantitative estimation of this effect in low concentrated lithium brine, GCPL measurements at various sodium concentrations were performed. The investigated sodium concentrations are 10 mM, 1, 2 and 5 M, together with 5 mM LiCl. The applied current is 1 mA, using the 5 mg/cm² mass loaded electrode. In Fig. 5.35, GCPL curves at low flow rate (a) and high flow rate (b) for the four investigated concentrations are reported. The x-axis is normalized by Q_r . The higher is the sodium concentration, the lower is Q_f/Q_r , thus confirming the negative effect of sodium during lithium intercalation. This effect is less evident at high flow rate (panel (b)). The results are represented clearer in Fig. 5.36, where Q_f/Q_r and $\bar{\eta}$ vs. Γ are reported. The curves show the typical behavior of Q_f/Q_r and $\bar{\eta}$ already observed in previous paragraphs, due to lithium mass transport overpotential. By increasing the sodium concentration, the curves show lower value of Q_f/Q_r . The saturation value of Q_f/Q_r passes from 0.85 at 10 mM, down to 0.65 at 5 M. The mean overpotential shows

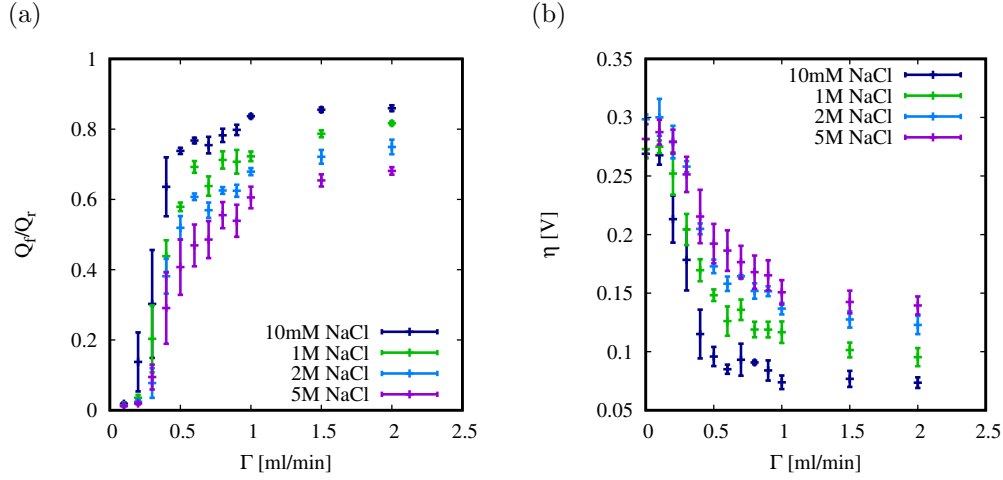


Figure 5.36: Panel (a): maximum solid filling of LiMn_2O_4 vs. flow rate; panel (b): mean overpotential; both quantities are reported at 10 mM, 1, 2 and 5 M NaCl and 5 mM of LiCl [64].

the opposite behavior, passing from 150 mV at 5 M, down to 70 mV at 10 mM. The results suggest the existence of an effect of Na^+ cations on the process efficiency. However, the difference between the captured lithium amount at 10 mM and 5 M at low flow rates is higher than the one at high flow rates. This suggests that the sodium effect can be compensated by increasing the flux inside the cell.

As already mentioned, this effect was reported in a previous work [8], where the authors attribute this behavior to a co-adsorption of sodium on the electrode surface, which limits the numbers of active sites available for lithium cations adsorption. Adsorption is indeed the first step of lithium intercalation in LMO [119, 120]. The effect of sodium co-adsorption is visible also in the oxidation branches of the galvanostatic curves of Fig. 5.35, although with less intensity compared to the reduction branch. The first plateau of the oxidation branches shows higher potential at higher sodium concentration, suggesting the presence of an overpotential also during the de-intercalation of lithium.

Fig. 5.37 reports the percentage of decrease of Q_f/Q_r vs. the ratio Na/Li, extracted by Fig. 5.36 (a) at Γ_s for 5 mM LiCl (1 ml/min), calculated with respect to the values obtained at 10 mM of NaCl. This graph gives a rough estimation of the efficiency decrease in term of amount of lithium captured due to the presence of sodium in solution.

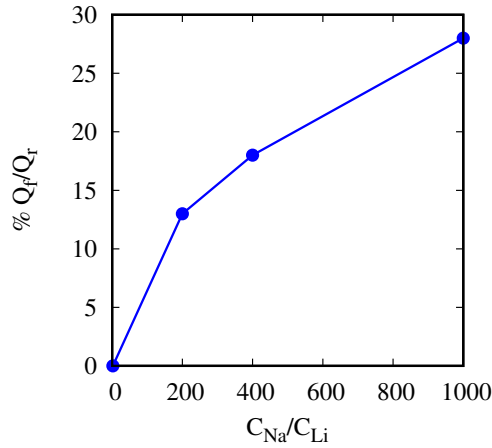


Figure 5.37: Percentage decrease of Q_f/Q_r calculated with respect to Q_f/Q_r measured in 10 mM of NaCl and 5 mM of LiCl vs. sodium and lithium concentration ratio in solution [64].

5.8 Ohmic drops

The estimation of the Ohmic drop η_Ω of the cell was performed. The measurement has been carried out thanks to the use of the two Ag/AgCl electrodes immersed in solution, by measuring the difference of potential between them during LMO cycles at various concentrations of NaCl in solution. The results are shown in Fig. 5.38, at 5 mM of LiCl and 10 mM, 1 M, 2 M and 5 M in panel (a), (b), (c) and (d) respectively. The potential is recorded vs. time, the black line represents LMO potential, the green line is η_Ω , which is positive during oxidation, negative during reduction of LMO and ≈ 0 between the cycle, when no current is applied. η_Ω potential at 10 mM is ≈ 33 mV, at 1 M is ≈ 2.5 mV, at 2 M is ≈ 1 mV and at 5 M is ≈ 0.7 mV. This values of η_Ω , which are a negligible with respect to LMO overpotential $\bar{\eta}$ shown in Fig. 5.36 (b) shows the advantage of the flow-through electrodes cell configuration, which allows to reduce the Ohmic drops thanks to the minimized distance between the electrodes.

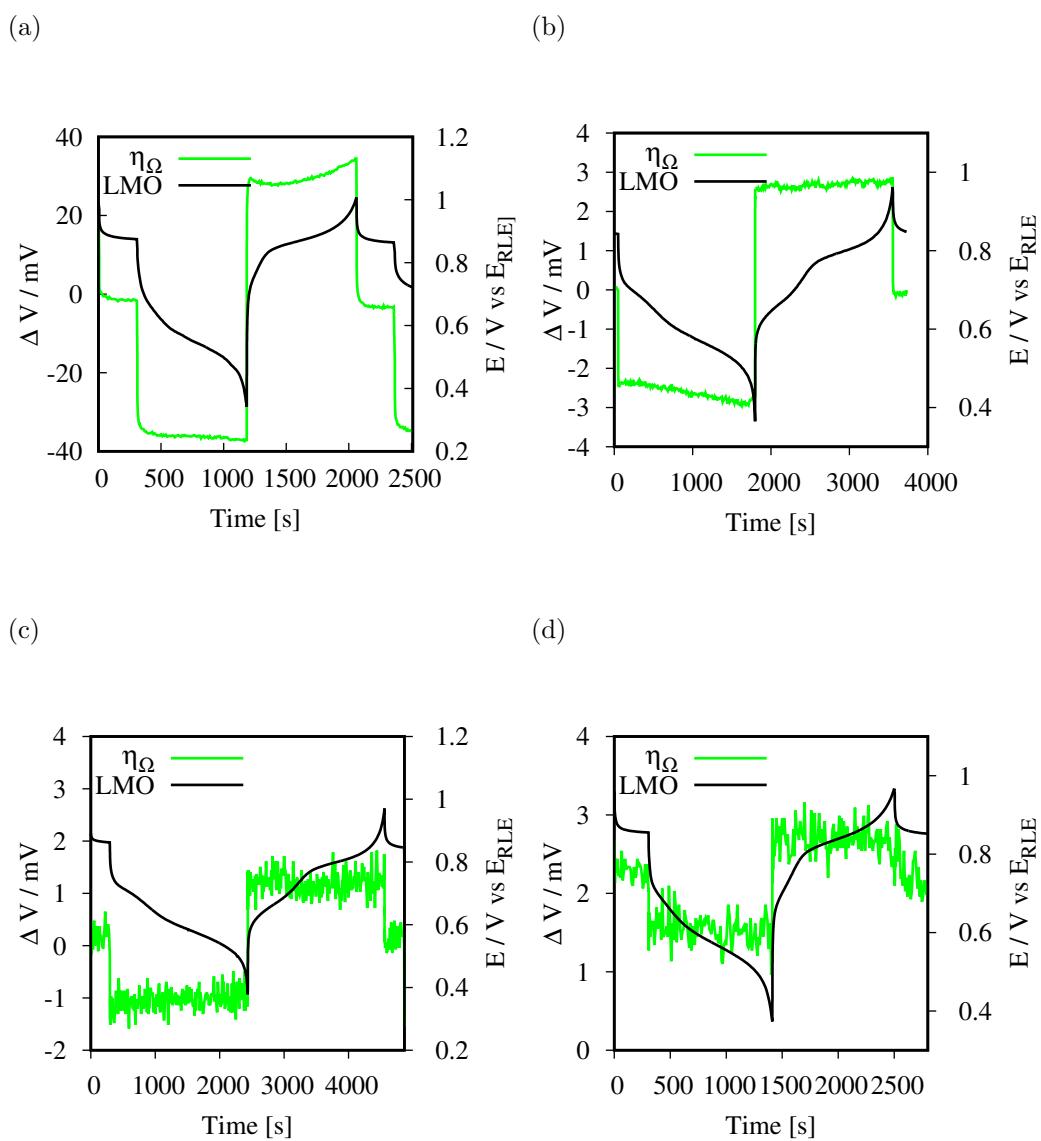


Figure 5.38: Ohmic drops and LMO potential vs. time during galvanostatic cycle, in 10 mM (panel (a)), 1 M (panel (b)), 2 M (panel (c)) and 5 M (panel (d)) of NaCl and 5 mM of LiCl [64].

Chapter 6

The Complete Process

In this Chapter, the procedure and the results of the complete lithium recovery process (capturing and release step) are reported. The extraction has been performed from a solution with the lowest investigated lithium concentration, 1 mM LiCl, and 100 mM NaCl. The information previously gained on the capturing step were used to choose the process working conditions (flow rate, current, mass loading).

The cell used to perform the entire process is the one described in paragraph 3.2.2. The WE is composed by 2 LMO electrodes, each loaded with 20 mg/cm² of active material, the CE is composed by 6 NiHCF electrodes, each loaded with 14 mg/cm² of active material. The masses ratio of LMO and NiHCF was decreased to 1:2 with respect to previous experiments, to minimize the unused mass of the counter. Mass loading of NiHCF is lower than in the previous cell to decrease its pressure drops. The total LMO active mass is circa 32 mg ($Q_r=3.4$ mAh), the total NiHCF active mass is circa 64 mg ($Q_r=3.8$ mAh).

The steps of the experiments are the following:

1. 150 ml of brine are pumped inside the cell with a flow rate of 15 ml/min (15 μ mol/min of Li⁺).
2. A negative current (0.5 mA) is applied to the cell. Li⁺ intercalation in LMO electrode and Na⁺ de-intercalation from NiHCF occurs.
3. The cell is clean with 120 mM KCl. Then the solution is pumped out by an air-flow to remove the residuals. After that, 5 ml of recovery solution (initial concentration 120 mM KCl) are pumped inside the cell.
4. A positive current is applied (1 mA) and de-intercalation of Li⁺ occurs, together with intercalation of K⁺ in NiHCF. The flow rate is 5 ml/min. At the end of the oxidation, the solution is pumped out by air-flow.

The volume amount pumped (150 ml) during capture contains 20% more lithium than the maximum amount that could be captured by LMO from “simil-Atacama” solution. The flow rate chosen was ~50% higher than the saturation flow rate extrapolated from Fig. 5.26 at the same current. The current has been chosen as a compromise between high capture yield, low pumping energy and convenient experiment time (~8 h).

During the release step, the electrolyte is pumped through the cell to allow the contact of the entire solution volume with the electrodes, allowing an homogeneous increase of the liquid concentration in the overall volume and improving the mass transport from solid to liquid. Considering the volume of the cell plates (0.73 ml) and the liquid volume retained by the electrodes ($0.7 \mu\text{l}/\text{mg}$) and separator ($10 \mu\text{l}/\text{cm}^2$) that were measured by weight difference, the total liquid volume contained in the cell is circa 0.82 ml, therefore lower than the recovery solution volume (5 ml). Beside, the recovery solution is recirculated continuously, because the complete charge would not be possible in one solution passage, as the liquid residence time is much smaller than the reaction time, like in the capturing step. The flow rate in this step was chosen as 1/3 of the one used during the capturing step.

The current applied during the release step is 1 mA, since it was already proved that a higher current during the release does not compromise the final lithium concentration and the charge efficiency [6]. Nine cycles (both capturing and release step) were performed one after the other, so that lithium is captured from a total brine volume of 1.35 l and released in 5 ml of recovery solution.

6.1 Analysis of the results

In Fig. 6.1 the galvanostatic curves of the charge and discharge steps of the cell are reported for the I, III, V, VII and IX cycle. In the bottom curve, the charge negatively increases as far the lithium capturing occurs. In the top curve the charge negatively decreases and lithium cations are released into the recovery solution. The cycle occurs clock-wise, the discharge occurs at lower potential then the charge, namely the process requires energy to proceed. The area between the two curves is equal to the energy required by the process.

The discharge curves are very similar to each other, only a slight difference is present in the maximum reduction charge. The capacity fading is higher than expected (15 % in nine consecutive cycles). This behavior may be due to the contact with air after each half-cycle, to remove the solution from the cell. The use of air flow is important especially before the injection of the 5 ml of recovery solution, to remove as much solution residual as possible to minimize contamination of recovery solution.

Q_f/Q_r is 0.7, higher than the saturation value obtained at 0.5 mA in the experiments

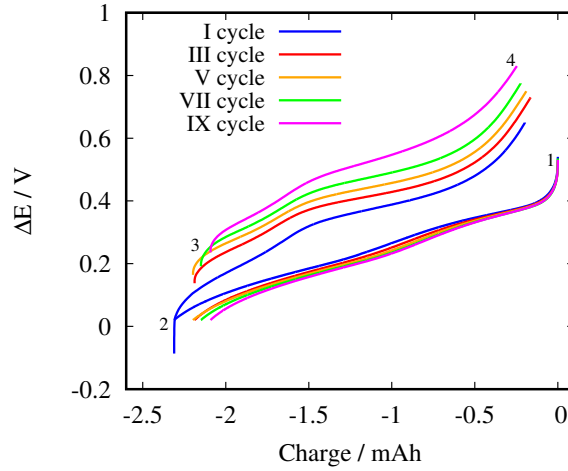


Figure 6.1: Galvanostatic charge/discharge curves for the I,III,V and VII cycles. Lithium is captured from the right to the left of the x-axis.

shown in Fig. 5.26, because in that case the ratio between the amount of lithium in the solution and the capacity of the electrode was lower than 1, while in this case it is 1.2.

The charge curves have higher potentials upon cycles. This is the Nernstian increase due to the higher Li^+ concentration in the recovery solution upon cycles, which leads to an increase of the required energy of the process, as it will be further discussed in the next paragraph.

The initial ($C_{i,in}$) and final ($C_{i,f}$) concentrations of the species i of the source solution were measured at each cycle with ICP-OES measurements. The C_f of recovery solution were measured for the I,II,III,V,VII,IX cycles. Specifically 10 μl were taken from the 5 ml recovery solution at the end of each cycle to be analysed. The detected concentrations of sources and recovery solutions for each cation are reported in Table 6.1 and Table 6.2 respectively. Moreover, in Table 6.2 purity coefficients of lithium in recovery solution upon cycles are reported, evaluated as the lithium concentration divided by sum of all cations concentration in the recovery solution:

$$K_{Li} = \frac{C_{Li}}{\sum C_i} \quad (6.1)$$

From Table 6.1, the mean values of $C_{Li,in}$ and $C_{Li,f}$ of the source solution are 0.93 ± 0.07 and 0.4 ± 0.05 mM, namely the yield of the capturing process is $\approx 60\%$. The relative error is attributed to the ICP-OES measurements. $C_{Na,f}$ is always higher than $C_{Na,in}$, as NiHCF electrode releases Na^+ in solution during the capturing. Nevertheless their difference is very small, due to the high amount of Na^+ in solution respect to the

Cycle	$C_{Li,in}$	$C_{Li,f}$	$C_{Na,in}$	$C_{Na,f}$
1	0.97	0.37	102.1	103.4
2	0.99	0.45	103.9	106.1
3	0.984	0.43	102.2	101.3
4	0.86	0.4	93.6	94.5
5	0.87	0.4	93.4	95.3
6	0.88	0.35	93.4	96
7	0.86	0.4	93.3	94.5
8	0.9	0.34	97.3	93.4
9	0.9	0.42	97.6	97.04

Table 6.1: Lithium and sodium concentrations in mM in the source solution at the beginning and at the end of the capturing step.

Cycle	$C_{Li,in}$	$C_{Li,f}$	$C_{K,in}$	$C_{K,f}$	$C_{Na,f}$	K_{Li}
1	0	15.6	117.5	101.3	0.63	0.13
2	15.6	29.5	101.3	85	1.49	0.25
3	29.5	41.7	85.2	68.1	2.03	0.37
5	-	60.9	-	44.1	6.87	0.54
7	-	80.2	-	8	-	
9	-	100	-	1	4.84	0.94

Table 6.2: Lithium, potassium and sodium concentration in mM in the recovery solution at the beginning and at the end of the release step and purity coefficient of lithium in recovery solution.

de-intercalated amount. In the source solutions of III, VIII and IX cycles $C_{Na,f} < C_{Na,in}$, probably due to some errors in the ICP-OES measurements.

It is worth to notice that the NiHCF at the end of the release step is full of K^+ , while during the capturing it mostly deintercalates Na^+ . This is due to the equilibrium exchange of K^+ with Na^+ after the release step, during the cell rinsing with the source solution, because of the presence of Na^+ in the liquid phase in contact with the solid.

As shown from the Table 6.2, Li^+ concentration in recovery solution increases upon cycles up to 100 mM, while K^+ concentration decreases down to 1 mM. K_{Li} increases upon cycles as expected, for the exchange of K^+ with Li^+ in solution. Na^+ concentrations increases upon cycles, probably due partial intercalation/adsorption in LMO electrode during the capturing step. C_{Na} of the VII cycle is not reported, as it is out of range. The final purity of the recovery solution is 94%.

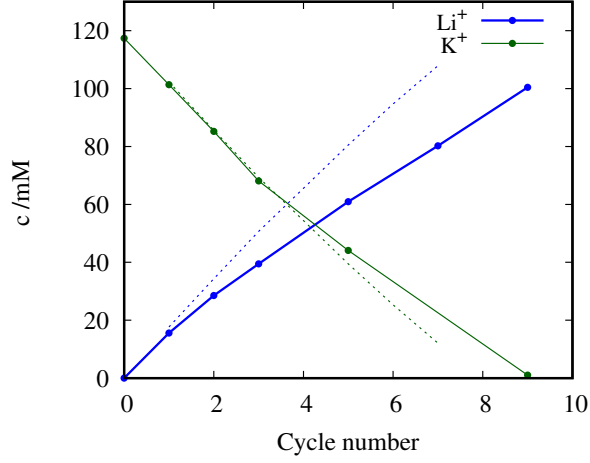


Figure 6.2: Li^+ and K^+ concentrations in the recovery solution vs. cycles (pointed line). The dotted lines are the estimated concentrations by means of the Faraday law with Coulombic efficiency equal to 1.

From the experimental values of the initial and final solution concentrations of each cycle, the Coulombic efficiencies η can be estimated for semi-reactions. Coulombic efficiency of intercalation (of Li^+ during the capturing step, of K^+ during the release) can be estimated as:

$$\eta_c = \frac{C_{i,in}V - |Q|/F}{C_{i,f}V} \quad (6.2)$$

where $C_{i,in}$ and $C_{i,f}$ are the starting and final Li^+ or K^+ concentrations detected by ICP-OES measurements, Q is the net charge passed during the (dis)charge, V is the solution volume.

The Coulombic efficiency of de-intercalation (of Li^+ during the release step and of Na^+ during the capturing step) can be instead evaluated as:

$$\eta_r = \frac{C_{i,f}V}{C_{i,in}V + |Q|/F} \quad (6.3)$$

The Coulombic efficiencies of the reactions occurring during the capturing step can be calculated for each cycle, by means of the initial and final concentrations of the source solution reported in Table 6.1. Their average values are 0.98 for Na^+ deintercalation and 0.9 for Li^+ capturing. This last value is in agreement with the one found in literature [6] and suggest the presence of a side reaction on LMO.

In Fig. 6.2, K^+ and Li^+ concentrations of recovery solution are reported vs. cycle numbers (pointed lines). In the same graph, “ideal” concentrations upon cycles evaluated

by means of Faraday law with Coulombic efficiency equal to 1 are reported (dotted lines). The value of K^+ measured with ICP-OES at the end of VII cycle is not reported in the graph because its measured value (8 mM) is too low and it leads to an efficiency higher than 1. The concentration of recovery solution at the beginning is 117 mM KCl, measured with ICP-OES before the start of the process. According to calculations, the maximum achievable concentration of Li^+ with a process efficiency equal to 1 is reached at the VII cycle and it is equal to 107 mM, while the respective K^+ concentration is 9.6 mM. The difference between calculated and the experimental final concentrations depends on the process efficiency. The release process efficiency evaluated as a ratio between final Li^+ concentration obtained experimentally and the ideal one is 75%.

The process efficiency is lower than 1 mainly due to two effects: the Coulombic efficiencies of the reactions that are lower than 1, for the presence of side reactions during (de)intercalation, and the effect of contamination from the rinsing solution, namely the starting recovery solution (117 mM KCl), which remains into the tubes, parts of the cell or absorbed into the electrodes. The contamination leads to a dilution of Li^+ concentration and to an increase of K^+ concentration. These effects give two different contributions to the shape of the concentrations curves vs. cycles: Coulombic efficiency decreases the line slope, while the contamination effect leads to a saturation value. After a certain number of cycle, the concentrations variation due to the electrochemical reactions becomes comparable with the one coming from contamination from rinsing solution and the process becomes no longer convenient. In Fig. 6.3 the concentrations upon cycles are reported at various values of retained volume, using the following expressions:

$$C_{j, Li} = \frac{C_{j-1, Li}V + |Q_j|/F}{V + V_r} \quad (6.4)$$

$$C_{j, K} = \frac{C_{j-1, K}V + C_{r, K}V_r - |Q_j|/F}{V + V_r} \quad (6.5)$$

where the index j indicates the cycle number and $C_{j, Li}$ and $C_{j, K}$ are the final concentrations of the cycle. V_r is the volume retained into the cell and $C_{r, K}$ is the concentration of the rinsing solution. Q_j is the net charge passed during the release step at each cycle. In Fig. 6.3, the arrows indicate the direction of larger V_r values. The higher is V_r , the lower is the cycle number at which the saturation of Li^+ concentration is reached. The K^+ concentration decreases slower with higher V_r , until it starts to increase. V_r has influence on the final concentration and purity of the recovery solution. Hence, it is very important to keep the value of V_r as low as possible.

If Coulombic efficiency was equal for the two reactions, the only effect that caused the decrease of efficiency would be the contamination from the rinsing solution. In this case, choosing a value of V_r , it would be possible to match the calculated curves with the experimental ones for both Li^+ and K^+ . This is not the case, as it was already observed

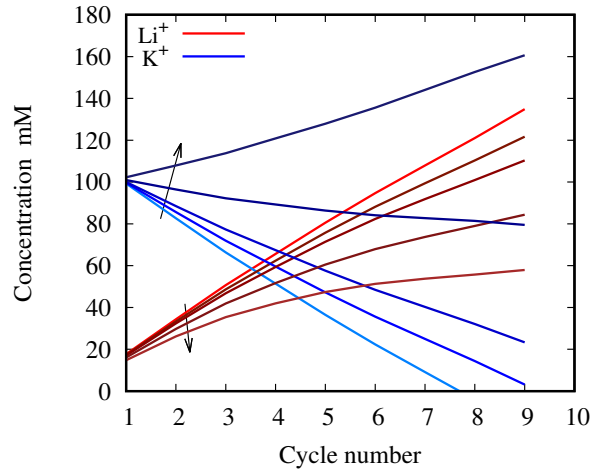


Figure 6.3: Li^+ and K^+ concentrations evaluated with Eqs. 6.4 and 6.5 at various V_r values, namely 0, 0.1, 0.2, 0.5 and 1 ml. The arrows go in the direction of larger V_r .

that the reactions have different values of Coulombic efficiencies. Choosing a V_r value of $70 \mu\text{l}$ and Coulombic efficiencies of 0.94 for capturing of K^+ and 0.8 for release of Li^+ , a good match between the curves is obtained. The result is reported in Fig. 6.4 (a).

According to the calculations, the retained volume is $70 \mu\text{l}$, namely 9% of cell volume and 1.4 % of recovery solution volume. This volume is close to the value of measured volume retained in the electrodes and separator ($90 \mu\text{l}$). The results show that in this experimental condition at the IX cycle the saturation of Li^+ concentration is still far. Using the same values of V_r and Coulombic efficiencies, the concentrations have been calculated for further cycles, starting from an initial K^+ concentration of 1 M in the recovery solution. The results, reported in Fig. 6.4 (b), show that Li^+ concentration curve approaches the saturation at circa 200 cycles, reaching a concentration of 0.8 M.

At the investigated experimental conditions, the total process efficiency, evaluated as the final lithium amount in recovery solution (3.45 mg) divided by the total amount in the source solution (9.3 mg) is 37%. This final efficiency can be further improved increasing the capture yield. In this final experiment, the capture yield is kept to 60 %, but it can be optimized up to 90 %, as proved in Section 5.4, by decreasing the applied current and the source solution volume.

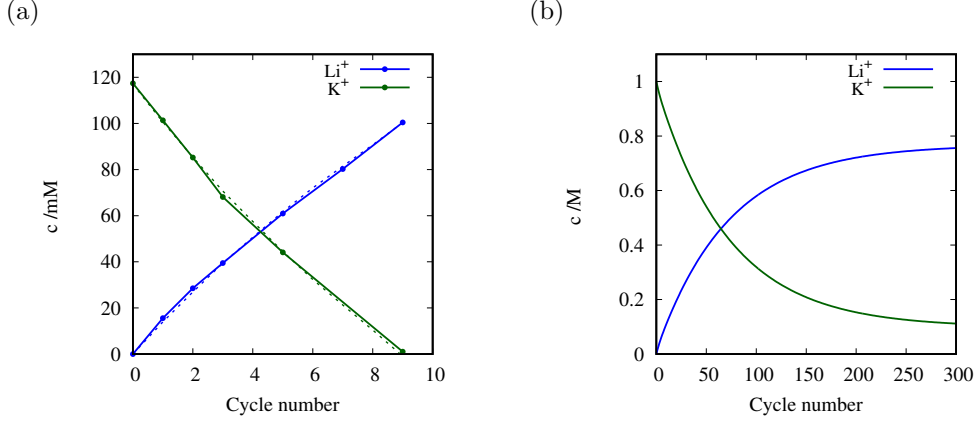


Figure 6.4: Panel (a): experimental concentrations upon cycles (pointed line) and calculated concentrations (dotted line) with $V_r=70 \mu\text{l}$ and Coulombic efficiencies values of 0.8 and 0.94 for Li^+ and K^+ (de)intercalation respectively. Panel (b): calculated concentrations up to 300 cycles starting from an initial K^+ concentration of 1 M.

6.2 Electrical power estimation

As already mentioned, energy consumption of the process can be estimated by the area between the charge and discharge curves of Fig. 6.1. It can be calculated as follows:

$$W = \int_1^2 \Delta E(Q) dQ + \int_3^4 \Delta E(Q) dQ \quad (6.6)$$

where ΔE is the voltage cell, Q is the charge. The numbers refer to various process steps, indicated in Fig 6.1. The first term of Eq. 6.6 is the energy required for capture, the second for release. Their sum is the net required energy for the total process.

The electrical energy can be divided in two contributions, the thermodynamic and the kinetic energies:

$$W = W_{th} + W_k \quad (6.7)$$

The thermodynamic contribution is the energy required to move the ions from a solution to the other and it includes the free energy differences between end and start of the cycle of the two solutions. It can be calculated by the Nernst equation of the reactions occurring during the first and third step, as previously reported [42].

The Nernst equations of the reactions occurring from point 1 to 2 (capture) and from point 3 to 4 (release) of Fig. 6.1 are:

$$\Delta E(Q) = \Delta E_1^0 + \Delta E_1'(Q) + \frac{RT}{F} \ln \left[\frac{C_{Li,1} + \frac{Q}{FV_1}}{C_{Na,1}} \right] (1-2) \quad (6.8)$$

$$\Delta E(Q) = \Delta E_2^0 + \Delta E_2'(Q) + \frac{RT}{F} \ln \left[\frac{C_{Li,3} + \frac{Q-Q_f}{FV_3}}{C_{K,3} - \frac{Q-Q_f}{FV_3}} \right] (3-4) \quad (6.9)$$

where Q is a negative number (as in Fig. 6.1) and Q_f is the maximum reduction charge for each cycle, so that $Q - Q_f$ is the net charge passed during the release step. During the capturing step, change of $C_{Li,1}$ has to be considered, while $C_{Na,1}$ is approximatively constant. Both $C_{Li,3}$ and $C_{K,3}$ change during the release step. ΔE_1^0 and ΔE_2^0 are constant terms depending on the standard potentials of the occurring reactions. Specifically:

$$\Delta E_1^0 = E_{Li}^{0,LMO} - E_{Na}^{0,NiHCF} \quad (6.10)$$

$$\Delta E_2^0 = E_{Li}^{0,LMO} - E_K^{0,NiHCF} \quad (6.11)$$

where $E_{Li}^{0,LMO}$ is the standard potential of intercalation of Li^+ in LMO, $E_{Na}^{0,NiHCF}$ and $E_K^{0,NiHCF}$ are the standard potentials of intercalation in NiHCF of Na^+ and K^+ respectively. $\Delta E'(q)$ is the potential contribution dependent on state of charge, which includes the excess potential of intercalation:

$$\Delta E_1' = E_{Li}^{LMO} - E_{Na}^{NiHCF} \quad (6.12)$$

$$\Delta E_2' = E_{Li}^{LMO} - E_K^{NiHCF} \quad (6.13)$$

Substituting Eqs. 6.8 and 6.9 in Eq. 6.6, one obtains:

$$W_{th} = \int_0^{Q_c} (\Delta E^0 + \Delta E') dQ + \frac{RT}{F} \ln \left[\frac{\left(C_{Li,3} + \frac{Q-Q_f}{FV_3} \right) C_{Na,1}}{\left(C_{Li,1} + \frac{Q}{FV_1} \right) \left(C_{K,3} - \frac{Q-Q_f}{FV_3} \right)} \right] dQ \quad (6.14)$$

where the first two terms can be approximated as follows:

$$\Delta E = \int_0^{Q_c} (\Delta E^0 + \Delta E') dQ = (\bar{E}_{Na} - \bar{E}_K) Q_c \quad (6.15)$$

The extreme of the integral Q_c is the charge of each cycle. Since charges passed during reduction and oxidation are different due to Coulombic efficiency, it can be approximated to the average value.

\bar{E}_{Na} and \bar{E}_K are the average potentials of intercalation of Na^+ and K^+ in NiHCF as defined in Eq. 4.17 in Section 4.2. This expression is an approximation because the average potential \bar{E} was defined as the integral of potential over the fraction of charge between 0 and 1, while in this case fraction of charge does not necessary arrive to the extreme values. The approximation is anyway reasonable, as ΔE^0 is a constant term, and it does not depend on the extremes, and $\Delta E'$ is negligible compared to the total

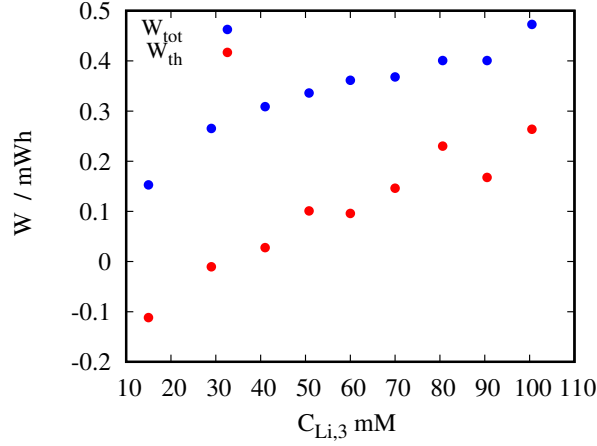


Figure 6.5: Thermodynamic energy evaluated by Eq. 6.14 and total energy evaluated from the galvanostatic curves.

potential, as it was verified in Section 4.2. As shown in Sect. 4.2, $\bar{E}_K > \bar{E}_{Na}$, hence this term reduces W_{th} of the system.

In Fig. 6.5, W_{th} values for each cycle calculated by Eq 6.14 are reported. They are estimated using experimental concentrations (extrapolated by Fig. 6.2) and the charges of each cycle. In the same graph the total energy required by the system evaluated from the integrals of the curves of Fig. 6.1 are shown.

The two curves have similar shape, logarithmically increasing with $C_{Li,3}$. This behavior was already reported in literature [42]. W_{th} is negative until ≈ 30 mM, namely the process is thermodynamically favored up to this concentration.

In Fig. 6.6, W_{tot} , W_{th} and W_k (the latter evaluated by Eq. 6.7) are reported, this time normalized by lithium number moles transferred in each cycle.

During the first two cycles, the W_{tot} is lower than the W_k , because it is compensated by the energy thermodynamically produced by the system. After that, the increase in total energy is almost totally due to the increase of W_{th} , while W_k keeps almost constant.

The total energy required for the process can be calculated as:

$$W_T = \sum_j \frac{W_{tot,j} N_j}{N_{tot}} \quad (6.16)$$

where j is the cycle number, N_j are the lithium moles transferred at each cycle, and N_{tot} are the total transferred moles. W_T for this experiment is equal to 6.1 Wh/mol.

The term ΔE of Eq. 6.15 (in this case equal to 130 mV) has a significant effect on the amount of energy required by the process. Considering the total charge flown into

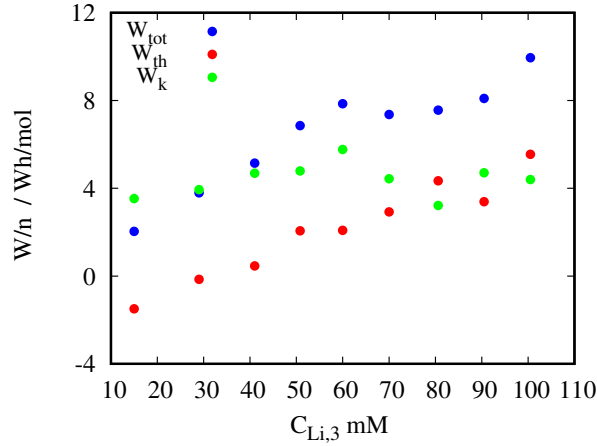


Figure 6.6: Total energy evaluated from the galvanostatic curves, thermodynamic energy evaluated by Eq. 6.14 and kinetic energy evaluated as difference, per unit of transferred lithium moles.

the system (circa 20 mAh) and the total lithium moles transferred (0.5 mmols), one can estimate that the energy due to this contribution is circa 5.2 Wh/mol. Hence by using KCl instead of NaCl in recovery solution, 85% of energy is spared. As already mentioned in Section 4.2, the choice of the second cation in recovery solution can be an important factor for decreasing the required electrical energy of the process.

6.3 Final pumping energy

Total pumping energy is calculated as reported in Sect. 5.6, using R_h of the cell, measured experimentally. Pressures of cell and single electrodes vs. the flow rates are reported in Fig. 6.7. The pressures of empty cell are reported in panel (a), line (a). R_h extrapolated by the line slope is 10.3 mbar min/ml, namely 2 times more than in the previous cell. This may be attributed to the higher compactness of this cell, in which the flow is forced to pass through the channels, without possibility to flow in other parts. Line (b) represents the pressure measurements of the cell with one LMO electrode (20 mg/cm²). Subtracting the cell resistance, R_h of LMO is equal to 7.1 mbar min/ml \approx 5 times higher than the 30% lower mass loaded LMO electrode used in the previous cell.

Line (c) shows the pressure of the cell with a NiHCF electrode. Subtracting the cell resistance, R_h of NiHCF is equal to 3.4 mbar min/ml, hence 2 times lower than R_h of LMO, thanks to the lower mass loading (14 mg/cm²) and to the higher porosity of the

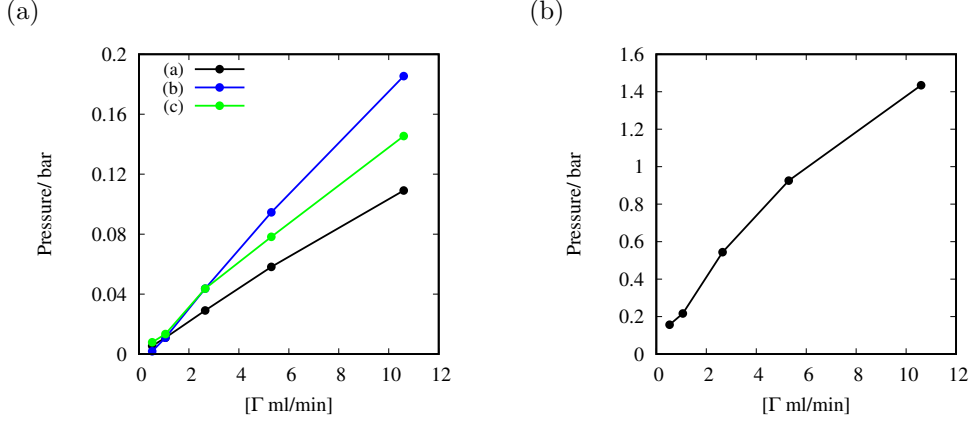


Figure 6.7: Panel (a): pressures vs. volumetric flow rate for the empty cell (a), for the cell with one LMO electrode (b) and with one NiHCF electrode (c). Panel (b): pressures vs. flow rate of the cell with the total electrodes stack.

electrode, obtained adding a lower NMP volume during the preparation of the slurry, as described in Section 3.1.

The pressure in the total stack is reported in Fig. 6.7, panel (b). Total stack includes 2 LMO electrodes, 6 NiHCF electrodes and 2 titanium frits. The total R_h is 130 mbar min/ml.

Using the total R_h of the total process, E_h is calculated from Eq. 5.47 and it is equal to 2.5 and 0.14 kWh/mol for the capturing and release step respectively. E_h required during capturing step is 18 times higher than the one for release step, due to the 3 times higher applied flow rate and the 2 times lower current.

The highest required energy of the process for extraction of lithium from 1 mM brine is the pumping energy, since the required electric energy (6.1 Wh/mol) is negligible with respect to it.

Finally, an estimation of total energy required by the process and its cost was performed for various lithium concentration brine at 1 mA. The results are shown in Fig. 6.8. The required energies are the electric energy to perform the process (W_{tot}) and the one to pump the electrolyte (E_h). E_h is estimated using Eq. 5.47, with R_h of the total cell (130 mbar/ml min) and Γ_s at the various concentrations at 1 mA extrapolated from Fig. 5.23 (a). W_{th} is evaluated from Eq. 6.14 at various $C_{Li,1}$, using the charge evaluated from the Q_f/Q_r curves of Fig. 5.23 (a). W_k evaluated in the last Section at 1 mM LiCl was rescaled proportionally to $\bar{\eta}$ of Fig. 5.23 (b), to get a rough value for all the concentrations. W_{tot} is then evaluated by Eq. 6.7.

W_{th} decreases logarithmically with brine concentration, as expected by Eq. 6.14. At 5

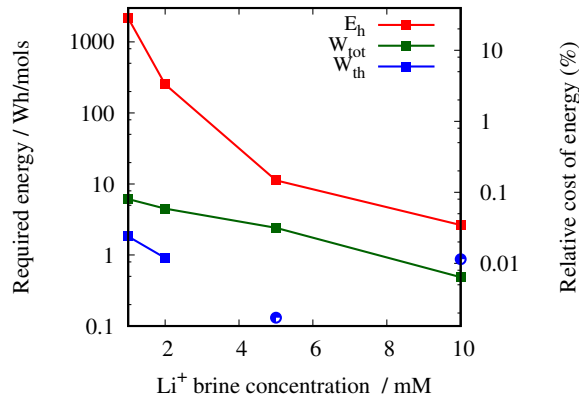


Figure 6.8: Energy per mole required for the total process vs. the lithium concentration in the source solution. In the secondary axis the energy cost is reported, in percentage with respect to the process income. The blue dots represent the absolute value of the thermodynamic energy, which is negative at 5 and 10 mM of LiCl.

and 10 mM W_{th} is negative, namely energy is produced during the process. W_k decreases as well, due to the decrease of mass transport overpotential by increasing the concentration. Pumping energy decreases quadratically with concentration as it was observed in Section 5.6.

At 1 and 2 mM W_{tot} is negligible compared to E_h . By increasing the brine concentration they become comparable. Increasing further lithium brine concentration, pumping energy continues to decrease and the W_{tot} becomes the prevalent energy.

The energy cost related to lithium price is reported in the secondary axis. The process is economically sustainable for all the concentration range. Relative energy costs increase by decreasing the brine concentration due to the enhancement of E_h , up to 28% at 1 mM.

The hydraulic energy can be further reduced applying lower current. Further optimizations of porous distribution of the electrodes may be carried out to decrease hydraulic resistances. Bigger active pores size would further improve lithium transport and decrease pressure drops.

Chapter 7

Conclusions and Outlook

The expected expansion of the lithium market in the coming years suggests the necessity to find faster and more sustainable ways to extract lithium than those currently used. The main amount of lithium distributed in the market at the moment is recovered from brine sources, located mostly in South America, with relatively high lithium concentrations that make possible its extraction. The diversification of the lithium sources and of the production sites is fundamental to make the lithium based technologies more competitive in the market. Hence the worldwide research is beginning to focus on the exploitation of other less concentrated sources of lithium.

In this PhD thesis, a reactor prototype for the lithium extraction from diluted brine has been presented. The electrochemical ion pumping technique by means of ion-exchange in solution has been successfully implemented in a flow through-electrode reactor, designed to extract lithium from low concentrated solutions at high efficiencies.

The development of the technology began with a prior study of the materials used in the process. In particular, the analysis of the intercalation mechanism in the lithium capturing electrode (LiMn_2O_4) has led to the development of a simple mathematical model that simulates the equilibrium curve. This model can be implemented in general in the electrochemical modelling of those systems where LiMn_2O_4 is used.

The thermodynamic behavior of the lithium excluding electrode (NiHCF) has been studied in mixed cationic species solutions, finding a correlation between the intercalation potential and the species concentrations in solution. Beside, the amount of the intercalated cations in the solid structure can be estimated. The results are relevant for future applications of the NiHCF in electrochemical ion pumping techniques in mixed cationic species solutions.

Two kinds of cells have been designed to perform the extraction process. The first cell was meant to investigate the capturing process from diluted brines (1-10 mM lithium

concentration), the second has been designed to perform both capturing and release steps.

The capturing step is the most challenging part of the process, due to the overpotential coming from transport of lithium in the liquid phase. Firstly, the influence of the electrolyte flow rate and brine concentrations on the solid filling of the active material has been investigated. By increasing the flow rate, the captured lithium amount increases, up to a maximum value of filling, which varies with lithium concentration in solution. This behavior is attributed to the porous structure of the electrode, which is made by various pore sizes and it has an irregular solid distribution. The flow passes mainly in the big inactive pores of the substrate, while it barely influences the small irregular pores created by the active material. This limits the maximum filling of the active material at low concentrations.

This results interpretation was proved by means of a mathematical model, that was developed to describe the system behavior during the capture. The model assumes a simplified electrode structure, composed by a pore distribution having a specific direction in the space, crossed by the flow at various velocities, considering lithium transport occurring along the cell thickness. Assuming an arbitrary distribution with pores of four different sizes, the model describes the capture efficiency trend with the flow rate for concentration higher than 5 mM. For lower concentrations, the model predicts much higher efficiencies than the experimental ones. This discrepancy has been attributed to the ideal electrode structure assumed in the model, that is described as a very compact solid layer with well defined pores evenly distributed.

On this grounds, in order to improve the capture efficiencies, a more compact solid layer was formed, by increasing the active material amount on LMO electrode, shifting the pore size distribution towards more active macropores. This leads to an improvement of the solid filling, that passes from 20% to 70% at the lowest investigated concentration (1 mM). On the other side, the pressure drop on the electrode increases, due to the lower permeability of the porous medium. The validity of the model has been further tested by adjusting the pore distribution parameters and the pressure drop to reproduce the experimental results obtained with the higher mass loaded electrode. It was shown that the model qualitatively describes the response of the system to a different permeability of the electrode.

After having investigating the maximum solid filling achieved, the process yield was optimized by changing the applied current. It was shown that, by decreasing the current, a higher process yield is obtained at lower flow rate, sparing hydraulic energy. In the optimal conditions, more than 90% of lithium in brine is captured. The reactor behavior at various currents is well described by the model. The model results show improvements in the capture efficiencies and lowering of the required hydraulic energy by decreasing the current, as occurs experimentally.

Despite its simplicity, the developed mathematical model qualitatively describes the reactor behavior at various operating parameters (flow rate, lithium concentration, mass loading, pressure drop, current), and it can be used to investigate the optimal working conditions of the process. Further improvements of the model can be carried out by describing other transport effects occurring in the porous electrodes, such as radial diffusion in the pores and inter-porous transport. This can be achieved by a more detailed description of the electrode structure.

Finally, the total process (both capturing and release steps) has been performed in the final cell. 1.35 l of brine containing 1 mM LiCl and 100 mM NaCl was treated in 9 cycles, obtaining 5 ml solution with 100 times higher lithium concentration than brine and 94% purity. The final lithium rich solution volume has been enlarged 15 times with respect to previous works. According to the experimental results, it can be predicted that, given a good stability of the electrodes upon time, the reactor could perform up to 200 cycles, reaching a final 0.8 M LiCl concentration in the recovery solution.

An economic analysis of the process run at 1 mA/cm², based on the estimation of pumping and electric energies, has shown that this technology is economically sustainable in the investigated concentration range. For extractions from sources at concentration lower than 5 mM, pumping energy is the main cost of the operation. For higher concentrations, pumping and electric energy become comparable and the process profit becomes higher than 95%. Pumping energy can be further reduced working at lower current.

The development of the technology reported in this PhD thesis opens the way to the industrial application of the reactor for extraction of lithium from diluted brines and thus to diversification of lithium global resources. Various sources of lithium that have so far remained unused, such as geothermal waters, brine produced in salt-works, waste waters from the gas and oil extraction wells could be exploited. The technology has the credentials to respond to the growth in lithium demand expected in the coming years.

Additional studies on the technology that may be relevant for the application could concern investigations on other factors, such as process temperature or presence of various impurities in brine. Further improvements on the porous distribution of the lithium capturing electrode could also be carried out, finding the trade-off structure between high capture efficiency and low hydraulic resistance. The reactor scale-up, aimed to the further increase of the final obtained volume, could be an additional step towards the use of the technology at an industrial level.

Bibliography

- [1] O. Groger, H. A. Gasteiger, and J.P. Suchsland. Review—electromobility: Batteries or fuel cells? *J. Electrochem. Soc.*, 162(14):A2605–A2622, 2015.
- [2] B. Dunn, H. Kamath, and J.M. Tarascon. Electrical energy storage for the grid: A battery of choices. *Science*, 334(6058):928–935, 2011.
- [3] M. Pasta, A. Battistel, and F. La Mantia. Batteries for lithium recovery from brines. *Energy Environ. Sci.*, 5:9487, 2012.
- [4] M. Pasta, C. D. Wessells, Y. Cui, and F. La Mantia. A desalination battery. *Nano Lett.*, 12:839–843, 2012.
- [5] R. Trócoli, A. Battistel, and F. La Mantia. Selectivity of a lithium-recovery process based on LiFePO_4 . *Chem. Eur. J.*, 20:1810–1813, 2014.
- [6] R. Trócoli, C. Erinwingbovo, and F. La Mantia. Optimized lithium recovery from brines by using an electrochemical ion-pumping process based on $\lambda\text{-MnO}_2$ and nickel hexacyanoferrate. *Chem. Electro Chem.*, 4:143–149, 2017.
- [7] R. Trócoli, A. Battistel, and F. La Mantia. Nickel hexacyanoferrate as suitable alternative to Ag for electrochemical lithium recovery. *ChemSusChem*, 8:2514–9, 2015.
- [8] F. Marchini, D. Rubi, M. del Pozo, F. J. Williams, and E. J. Calvo. Surface chemistry and lithium-ion exchange in LiMn_2O_4 for the electrochemical selective extraction of LiCl from natural salt lake brines. *J. Phys. Chem. C*, 120(29):15875–15883, 2016.
- [9] L.L. Missoni, F. Marchini, M. del Pozo, and E. J. Calvo. A LiMn_2O_4 -polypyrrole system for the extraction of LiCl from natural brine. *J. Electrochem. Soc.*, 163(9):A1898–A1902, 2016.
- [10] Deutsche Bank. Welcome to the lithium-ion age. <http://www.slideshare.net/Tehama/welcome-to-the-lithium-ion-age-lithium-101-deutsche-bank-may-9-2016>, Mai 2016.
- [11] An increasingly precious metal. <http://www.economist.com/business/2016/01/14/an-increasingly-precious-metal>, Gen 2016.
- [12] Website of a european lithium, a company that extracts lithium from mining. <http://europeanlithium.com/lithium/lithium-in-europe>, 2018.
- [13] Vikström, H., Davidsson, S., and M. Höök. Lithium availability and future production outlooks. *Appl. Energy*, 110:252–266, 2013.

- [14] D. Kushnir and B. A. Sandén. The time dimension and lithium resource constraints for electric vehicles. *Resources Policy*, 37(10):93–103, 2012.
- [15] V. Flexer, C. F. Baspineiro, and C. I. Galli. Lithium recovery from brines: A vital raw material for green energies with a potential environmental impact in its mining and processing. *Science of The Total Environment*, 639:1188–1204, 2018.
- [16] C. Grosjean, P. Miranda, M. Perrin, and P. Poggi. Assessment of world lithium resources and consequences of their geographic distribution on the expected development of the electric vehicle industry. *Renew. Sust. Energy. Rev.*, 16:1735–1744, 2012.
- [17] B. Swain. Recovery and recycling of lithium: A review. *Separat. and Purif. Tech.*, 172:388–403, 2017.
- [18] L. T. Peiró, G. V. Méndez, and R.U. Ayres. Lithium: Sources, production, uses, and recovery outlook. *JOM*, 65:986–996, 2013.
- [19] D. Kaplan. Process for the extraction of lithium from dead sea solutions. *Israel Journ. of Chem.*, 1(2):115–120, 1963.
- [20] J.A. Epstein, E.M. Feist, J. Zmora, and Y. Marcus. Extraction of lithium from the dead sea. *J. Appl. Chem. Biotech.*, 6(3-4):269–275, 1981.
- [21] I. Pelly. Recovery of lithium from dead sea brines. *J. Appl. Chem. Biotech.*, 28(7):469–474, 1978.
- [22] Zandevakili S., Ranjbar M., and Ehteshamzadehc M. Recovery of lithium from urmia lake by a nanostructure MnO_2 ion sieve. *Hydrometallurgy*, 149:148–152, 2014.
- [23] R. Chitrakar, Y. Makita, K. Ooi, and A. Sonoda. Synthesis of iron-doped manganese oxides with an ion-sieve property: Lithium adsorption from bolivian brine. *Ind. Eng. Chem. Res.*, 53(9):3682–3688, 2014.
- [24] J.-L. Xiao, S.-Y. Sun, J. Wang, P. Li, and J.-G. Yu. Synthesis and adsorption properties of $\text{Li}_1 \cdot 6\text{Mn}_1 \cdot 6\text{O}_4$ spinel. *Ind. Eng. Chem.*, 52:11967–73, 2013.
- [25] R. Chitrakar, Y. Makita, K. Ooib, and A. Sonoda. Lithium recovery from salt lake brine by H_2TiO_3 . *Dalton Trans.*, 43:8933–8939, 2014.
- [26] Z. Hui. Property of H_2TiO_3 type ion-exchangers and extraction of lithium from brine of natural gas wells. *Chin. J. Appl. Chem.*, 17(9):307–309, 2000.
- [27] M.J. Park, G. M. Nisola, A. B. Beltran, R.Eliseo, C. Torrejos, J. G. Seo, S-P. Lee, H. Kim, and W-J. Chung. Recyclable composite nanofiber adsorbent for Li^+ recovery from seawater desalination retentate. *Chem. Engin. Journ.*, 254:73–81, 2014.
- [28] Z. Zhou, W. Qin, and W. Fei. Extraction equilibria of lithium with tributyl phosphate in three diluents. *J. Chem. Eng. Data*, 56(9):3518–3522, 2011.
- [29] H. Bukowsky and E. Uhlemann. Selective extraction of lithium chloride from brines. *Sep. Sci. Technol.*, 28:1357–1360, 1993.
- [30] G.G. Gabra and A.E. Torma. Lithium chloride extraction by n-butanol. *Hydrometallurgy*, 3:23–33, 1978.

- [31] A.Somrani, A.H. Hamzaoui, and M.Pontie. Study on lithium separation from salt lake brines by nanofiltration (nf) and low pressure reverse osmosis (lpro). *Desalination*, 317:184–192, 2013.
- [32] S. Sun, L. Cai, X. Nie, and X. Song J. Yiu. Separation of magnesium and lithium from brine using a desal nanofiltration membrane. *Jour. Water Process Eng.*, 7:210–217, 2015.
- [33] Z. Ji, Q. Chen, J. Yuan, J. Liu, Y. Zhao, and W. Feng. Preliminary study on recovering lithium from high ceMg²⁺/Li⁺ ratio brines by electrodialysis. *Separ. Purif. Techn.*, 172:168–177, 2016.
- [34] H. Kanoh, K. Ooi, Y. Miyai, and S. Katoh. Selective electroinsertion of lithium ions into a platinum/lambda-manganese dioxide electrode in the aqueous phase. *Langmuir*, 7:1841–1842, 1991.
- [35] H. Kanoh, K. Ooi, Y. Miyai, and S. Katoh. Electrochemical recovery of lithium ions in the aqueous phase. *Sep. Sci. Technol.*, 28:643–651, 1991.
- [36] F. La Mantia, M. Pasta, H. D. Deshazer, B. E. Logan, and Y.Cui. Batteries for efficient energy extraction from a water salinity difference. *Nano Lett.*, 11:839–843, 2011.
- [37] A. Cipollina and G. Micale. *Sustainable Energy from Salinity Gradients*. Woodhead Publishing, 2016.
- [38] C. D. Wessells, S.V. Peddada, R. A. Huggins, and Y. Cui. Nickel hexacyanoferrate nanoparticle electrodes for aqueous sodium and potassium ion batteries. *Nano Lett.*, 11(12):5421–5425, 2011.
- [39] R. Trocoli and F. La Mantia. An aqueous zinc-ion battery based on copper hexacyanoferrate. *ChemSusChem*, 8(3):481–485, 2015.
- [40] C. D. Wessells, S. V. Peddada, M. T. McDowell, R. A. Huggins, and Y. Cui. The effect of insertion species on nanostructured open framework hexacyanoferrate battery electrodes. *Jour. of The Electr. Soc.*, 159(2):A98–A103, 2012.
- [41] Donald E. Garrett. *Handbook of Lithium and Natural Calcium Chloride*. Elsevier Science, 2004.
- [42] Trócoli R., G. Kasiri Bidhendi, and LaMantia F. Lithium recovery by means of electrochemical ion pumping: a comparison between salt capturing and selective exchange. *J. Phys. Condens. Matter*, 28(11), 2016.
- [43] W. J. Repsher and Kirby T. Rapstein. Recovery of lithium from brine.
- [44] Y. Kenjiro, Y. Tetsutaro, K. Kentaro, and M. Toshikazu. The recovery of lithium from geothermal water in the hatchobaru area of kyushu, japan. *CSJ Journals*, 56(8):2490–2498, 1983.
- [45] Y. Tetsutaro, K. Kentaro, and I. Hirotsugu. Basic study on lithium recovery from lithium containing solution. *CSJ Journals*, 59(4):1207–1213, 1986.
- [46] J. Koryta and J. Dvor/ák. *Principles of Electrochemistry*. John Wiley and Sons, 1987.
- [47] Q. Feng, Y. Miyai, H. Kanoh, and K. Ooi. Li⁺ extraction/insertion with spinel-type lithium manganese oxides. characterization of redox-type and ion-exchange-type sites. *Langmuir*, 8:1861–1876, 1992.
- [48] C. Erinmwingbovo, M. S. Palagonia, D. Brogioli, and F.La Mantia. Intercalation into a prussian blue derivative from solutions containing two species of cations. *ChemPhysChem*, 18:917–925, 2016.

- [49] J. W. McCargar and V. D. Neff. Thermodynamics of mixed-valence intercalation reactions: the electrochemical reduction of prussian blue. *J. Phys. Chem.*, 92:3598–3604, 1988.
- [50] D. K Kim, P. Muralidharan, H. W. Lee, R. Ruffo, Y. Yang, C. K. Chan, H. Peng, R. A. Huggins, and Y. Cui. Spinel LiMn_2O_4 nanorods as lithium ion battery cathodes. *Nano Lett.*, 145:3948–3952, 2008.
- [51] M. Doyle P. Arora, R.E. White. Capacity fade mechanisms and side reactions in lithium-ion batteries. *Jour. of Electrochem. Soc.*, 145:3647–3667, 1998.
- [52] J. Koryta and J. Dvorák.
- [53] E.N. Guyes, A. N. Shocron, A. Simanovski, P.M. Biesheuvel, and M.E. Suss. A one-dimensional model for water desalination by flow-through electrode capacitive deionization. *Desalination*, 415:8–13, 2017.
- [54] A. Trainham and J. Newman. A flow-through porous electrode model: Application to metal-ion removal from dilute streams. *Jour. Elec. Soc.*, 124(10):1528–1540, 1977.
- [55] A. Trainham and J. Newman. A comparison between flow-through and flow-by porous electrodes for redox energy storage. *Electrochimica Acta*, 26(4):455–469, 1981.
- [56] D. N. Bennion and J. Newman. Electrochemical removal of copper ions from very dilute solutions. *J. of Applied Electrochem.*, 2(2):113–122, 1972.
- [57] A. T. Kuhn and R. W. Houghton. Comparison of the performance of electrochemical reactor designs in the treatment of dilute solutions. *Electrochimica Acta*, 19:733–737, 1974.
- [58] J. Van Zee and J. Newman. Electrochemical removal of silver ions from photographic fixing solutions using a porous flow-through electrode. *Jour. Electr. Soc.*, 124:706–708, 1977.
- [59] J. M. Williams and K. B. Keating. Extended-surface electrolysis removes heavy metals from waste streams. *Du Pont Innovation*, 6:6–10, 1975.
- [60] A. K. P. Chu, M. Fleischmann, and G. J. Hills. Packed bed electrodes. i. the electrochemical extraction of copper ions from dilute aqueous solutions. *Jour. app. Electrochemistry*, 4:323–330, 1974.
- [61] I. Cohen, E. Avraham, M. Noked, A. Soffer, and D. Aurbach. Enhanced charge efficiency in capacitive deionization achieved by surface-treated electrodes and by means of a third electrode. *J. Phys. Chem., C* 115(40):19856–19863, 2011.
- [62] M. E. Suss, T.F. Baumann, W. L. Bourcier, C. M. Spadaccini, K. A. Rose, and J.G. Santiago M. Stadermann. Capacitive desalination with flow-through electrodes. *Energy Environ*, 5:9511–9519, 2012.
- [63] A.M. Johnson and J. Newman. Desalting by means of porous carbon electrodes. *Electrochem. Soc.*, 118(3):510–517, 1971.
- [64] M.S. Palagonia, D. Brogioli, and F. La Mantia. Influence of hydrodynamics on the lithium recovery efficiency in an electrochemical ion pumping separation process. *J. Electr. Soc.*
- [65] William M. Haynes. *CRC Handbook of Chemistry and Physics*. Editor-in-Chief, 2012.

- [66] W. Liu, G. C. Farrington, F. Chaput, and B. Dunn. Synthesis and electrochemical studies of spinel phase LiMn_2O_4 cathode materials prepared by the pechini process. *The Electrochemical Society*, 143(3):879–884, 1996.
- [67] R. J. Gummow and M. M. Thackeray. An investigation of spinel related and orthorhombic LiMnO_2 cathodes for rechargeable lithium batteries. *J. Electrochem. Soc.*, 141:1178–1182, 1994.
- [68] J.B. Goodenough. Design considerations. *Solid State Ionics*, 69:184–198, 1993.
- [69] W. Liu, K. Kowal, and G. C. Farrington. Mechanism of the electrochemical insertion of lithium into LiMn_2O_4 spinels. *J. Electrochem. Soc.*, 145(2), 1998.
- [70] Y. Lu, L. Wang, J. Cheng, and J. B. Goodenough. Prussian blue: a new framework of electrode materials for sodium batteries. *Chemical Comm.*, 48:6544–6546, 2012.
- [71] P. Nie, L. Shen, H. Luo, B. Ding, G. Xu, J. Wang, and X. Zhang. Prussian blue analogues: a new class of anode materials for lithium ion batteries. *J. Mater. Chem.*, 2:5852–5857, 2014.
- [72] G. Małecki and A. Ratuszna. Crystal structure of cyanometallates $\text{Me}_3[\text{Co}(\text{CN})_6]_2$ and $\text{KMe}[\text{Fe}(\text{CN})_6]$ with $\text{Me}=\text{Mn}_2^+$, Ni_2^+ , Cu_2^+ . *Powder Diff.*, 14(01):25–30, 1999.
- [73] A. Ludi and H. U. Güdel. Structural chemistry of polynuclear transition metal cyanides. In *Struct. Bond.*, volume 14, pages 1–21. Springer, 1973.
- [74] H. J. Buser, D. Schwarzenbach, W. Petter, and A. Ludi. The crystal structure of prussian blue: $\text{Fe}_4[\text{Fe}(\text{CN})_6]_3 \cdot x\text{H}_2\text{O}$. *Inorg. Chem.*, 16:2704–2710, 1977.
- [75] F. Herren, P. Fischer, A. Ludi, and W. Halg. Neutron diffraction study of prussian blue, $\text{Fe}_4[\text{Fe}(\text{CN})_6]_3 \cdot x\text{H}_2\text{O}$. location of water molecules and long-range magnetic order. *Inorg. Chem.*, 19:956–959, 1980.
- [76] V. D. Neff. Electrochemical oxidation and reduction of thin films of prussian blue. *J. Electrochem. Soc.*, 125:886–887, 1978.
- [77] C. D. Wessells, R. A. Huggins, and Y. Cui. Copper hexacyanoferrate battery electrodes with long cycle life and high power. *Nature Comm.*, 2:550, 2011.
- [78] M. Pasta, C. D. Wessells, R. A. Huggins, and Y. Cui. A high-rate and long cycle life aqueous electrolyte battery for grid-scale energy storage. *Nature Comm.*, 3:1149, 2012.
- [79] S. Porada, A. Shrivastava, P. Bukowska, P.M. Biesheuvel, and K. C. Smith. Nickel hexacyanoferrate electrodes for continuous cation intercalation desalination of brackish water. *Electrochimica Acta*, 255:369–378, 2017.
- [80] Z. Jia, B. Wang, S. Song, and Y. Fan. A membrane-less Na ion battery-based capmix cell for energy extraction using water salinity gradients. *RSC Adv.*, 3:26205–26209, 2013.
- [81] H. M. H. Tehrani, S. A. Seyedsadjadi, and A. Ghaffarinejad. Application of electrodeposited cobalt hexacyanoferrate film to extract energy from water salinity gradients. *RSC Adv.*, 5:30032–30037, 2015.
- [82] T. Kim, M. Rahimi, B. E. Logan, and C. A. Gorski. Harvesting energy from salinity differences using battery electrodes in a concentration flow cell. *Environ. Sci. Technol.*, pages 9791–9797, 2016.

- [83] Y. Yang, C. Brownell, and N. Sadrieh. Quantitative measurement of cyanide released from prussian blue. *Clin. Toxicol.*, 45:776–781, 2007.
- [84] K. Lu, Z. Hu, Z. Xiang, J. Ma, B. Song, J. Zhang, and H. Ma. Cation intercalation in manganese oxide nanosheets: Effects on lithium and sodium storage. *Angew. Chem. Int. Ed.*, 55:10448–10452, 2016.
- [85] Y. Cui, X. Zhao, and R. Guo. High rate electrochemical performances of nanosized ZnO and carbon co-coated LiFePO₄ cathode. *Materials Research Bulletin*, 45(7):844–849, 2010.
- [86] Hyun-Wook Lee, Mauro Pasta, R. Y. Wang, R. Ruffo, and Y. Cui. Effect of the alkali insertion ion on the electrochemical properties of nickel hexacyanoferrate electrodes. *Faraday Discuss.*, 176:69–81, 2014.
- [87] J. J. García-Jareño, A. Sanmatías, D. Benito, J. Navarro-Laboulais, and F. Vicente. The role of inner counterions within pb films during electrochemical processes. *Intern. J. Inorg. Mater.*, 1:343–349, 1999.
- [88] Joel H. Hildebrand. Solubility. xii. regular solutions. *J. Am. Chem. Soc.*, 51:66, 1929.
- [89] Thermae di Salsomaggiore. Salsomaggiore water analysis, February 2012.
- [90] W. Tiedemann and J. Newman. Porous-electrode theory with battery applications. *J. Electrochem. Soc.*, 21(1):25–41, 1993.
- [91] T. F. Fuller and J. Newman. Water and thermal management in solid-polymer-electrolyte fuel cells. *J. Electrochem. Soc.*, 140(5):1218–1225, 1993.
- [92] M. Doyle, T. F. Fuller, and J. Newman. A modeling of galvanostatic charge and discharge of the lithium/polymer/insertion cell. *J. Electrochem. Soc.*, 140(6):1526–1533, 1993.
- [93] M. Doyle, J. Newman, A. S. Gozdz, C.N. Schmutzm, and J.M. Tarascon. Comparison of modeling predictions with experimental data from plastic lithium ion cell. *J. Electrochem. Soc.*, 143(6):1890–1903, 1996.
- [94] R. A. Rica, D.Broglioli, R. Ziano, D. Salerno, and F. Mantegazza. Ions transport and adsorption mechanisms in porous electrodes during capacitive-mixing double layer expansion (cdle). *J. Phys. Chem.*, C116(32):16934–16938, 2012.
- [95] M. Yaniv and A. Soffer. The transient behavior of an ideally polarized porous carbon electrode at constant charging current. *J. Electrochem. Soc.*, 123(4):506–511, 1976.
- [96] P. M. Biesheuvel, Y. Fu, and M. Z. Bazant. Diffuse charge and faradaic reactions in porous electrodes. *Phys. Rev.*, E8(6):061507, 2011.
- [97] J. T. Fredrich, A. A. DiGiovanni, and D. R. Noble. Predicting macroscopic transport properties using microscopic image data. *J. Geophys. Res.*, B03201(111):1–14, 2006.
- [98] J.C. Santamarina, M.A. Fam, and K.A. Klein. *Soils and waves*. Chichester: Wiley, 2001.
- [99] T. Aste, M. Saadatfar, and T. J. Senden. Geometrical structure of disordered sphere packings. *Phys. Rev.*, 71(6):061302, 2005.
- [100] J. Perret, S Prasher, A. Kantzas, and C. H. Langford. Three-dimensional quantification of macropore networks in undisturbed soil cores. *Soil Sci. Soc. America Jour.*, 63(6):1530–43, 1999.

- [101] L. B. Wang, J. D. Frost, and J. S. Lai. Three-dimensional digital representation of granular material microstructure from x-ray tomography imaging. *J. Comput. Civil Eng.*, 18(1):28–35, 2004.
- [102] M.H.G. Amin, L.D. Hall, R.J. Chorley, T.A. Carpenter, K.S. Richards, and B.W. Bache. Magnetic resonance imaging of soil-water phenomena. *Magnetic Resonance Imaging*, 2:319–321, 1994.
- [103] M. Deurer, I. Vogeler, A. Khrapichev, and D. Scotter. Imaging of water flow in porous media by magnetic resonance imaging microscopy. *J. Environ. Qual.*, 31(2):487–93, 2002.
- [104] W. Fourie, R. Said, P. Young, D.L. Barnes, and D.L. Barnes. The simulation of pore scale fluid flow with real world geometries obtained from x-ray computed tomography. *Excerpt from the Proceedings of the COMSOL Conference, Boston*, 2007.
- [105] G. A. Narsilio, O. Buzzi, S. Fityus, T.S. Yun, and D.W. Smith. Upscaling of navier–stokes equations in porous media: Theoretical, numerical and experimental approach. *Computers and Geotechnics*, 36(7):1200–06, 2009.
- [106] M. Matyka, A. Khalili, and Z. Koza. Tortuosity-porosity relation in porous media flow. *Phys. Rev.*, E78:026306, 2008.
- [107] M. R. Palacín. Recent advances in rechargeable battery materials: a chemist’s perspective. *Chem. Soc. Rev.*, 38(9):2565–2575, 2009.
- [108] J. Paul M. Oswal and R. Zhao. A comparative study of lithium ion batteries. *AME 578 project*, 2010.
- [109] M. Doyle, T. F. Fuller, and J. Newman. Modeling of galvanostatic charge and discharge of the lithium/polymer/insertion cell. *J. Electrochem. Soc.*, 140(6):1526–1533, 1993.
- [110] S. T. Taleghani, B. Marcos, K. Zaghbi, and G. Lantagne. A study on the effect of porosity and particles size distribution on Li-ion battery performance. *J. Electrochem. Soc.*, 164(11):E3179–E3189, 2017.
- [111] A. Hatzikioseyan, M. Tsezos, and F Mavituna. Application of simplified rapid equilibrium models in simulating experimental breakthrough curves from fixed bed biosorption reactors. *Hydrometallurgy*, 59(2-3):395–406, 2001.
- [112] I. Nuic, M. Trgo, and N. V. Medvidovič. The application of the packed bed reactor theory to Pb and Zn uptake from the binary solution onto the fixed bed of natural zeolite. *Chem. Eng. J.*, 295:347–357, 2016.
- [113] D. Hendricks. *Water Treatment Unit Processes: Physical and Chemical*, pages 93–117. Press Taylor & Francis Group, 2006.
- [114] D. Koster, G. D. Guoqing, A. Battistel, and F. La Mantia. Dynamic impedance spectroscopy using dynamic multi-frequency analysis: A theoretical and experimental investigation. *Electrochimica Acta*, 2017.
- [115] D. M. Ruthven. *Principles of Adsorption and Adsorption Processes*. Wiley, 1984.
- [116] Don W. Green and R. H. Perry. *Perry’s chemical engineers’ handbook*. McGraw-Hill, 2007.
- [117] F. Civan. Scale effect on porosity and permeability: Kinetics, model, and correlation. *AIChE Journal*, 47:271–287, 2001.

- [118] Industrial electricity prices in selected countries in europe 2017, by amount consumed. <https://www.statista.com/statistics/267068/industrial-electricity-prices-in-europe>, 2017.
- [119] F. Marchini, F. J. Williams, and E.J.Calvo. Electrochemical impedance spectroscopy study of the $\text{Li}_x\text{Mn}_2\text{O}_4$ interface with natural brine. *Jour. Electroanalyt. Chem.*, 819:428–434, 2018.
- [120] P.G. Bruce and M.Y. Saidi. The mechanism of electrointercalation. *Jour. Electroanalyt. Chem.*, 322(1-2):93–105, 2018.

List of Abbreviations

CDL	Compact Double Layer
CE	Counter Electrode
CSTR	Continuous Stirred Tank Reactor
CV	Cyclic Voltammetry
DDL	Diffuse Double Layer
FBE	Flow-By Electrodes
FTE	Flow-Through Electrodes
GCPL	Galvanostatic Cycling with Potential Limitations
IHP	Inner Helmotz Plane
ICP-OES	Inductively Coupled Plasma Emission Spectroscopy
LFP	Lithium Ion Phosphate
LMO	Lithium Manganese Oxide
NiHCF	Nickel Hexacyanoferrate
NMP	N-Methyl-Pyrrolidone
OCV	Open Circuit Voltage
OHP	Outer Helmotz Plane
PFR	Plug Flow Reactor
RE	Reference Electrode
SEM	Scanning Electron Microscope
WE	Working Electrode

List of Symbols

a_i	activity coefficient of the species i	-
a_{int}	area per unit volume	[m ⁻¹]
A_e	area of the electrode	[cm ²]
A_m	area of fluid passage	[cm ²]
A_s	solid and liquid exchange area	[cm ²]
C_{cdl}	capacitance of the compact double layer	[μ F cm ⁻²]
C_i	concentration in the liquid	[mol dm ⁻³]
C_i^b	bulk concentration	[mol dm ⁻³]
$C_{i,in}$	starting concentration in solution	[mol dm ⁻³]
$C_{i,f}$	final concentration in solution	[mol dm ⁻³]
$C_{j,i}$	concentration in solution of the species i at the cycle j	[mol dm ⁻³]
C_m	concentration in the stirred tank	[mol dm ⁻³]
$C_{s,i}$	concentration of the cations in the solid	[mol dm ⁻³]
C_T	maximum concentration of cations in the solid	[mol dm ⁻³]
$C_{1,i}$	starting concentration in the source solution	[mol dm ⁻³]
$C_{3,i}$	starting concentration in the recovery solution	[mol dm ⁻³]
d	diameter of cell tube	[mm]
dC	normalized differential capacitance of a battery material	-
d_i	thickness of the inner Helmotz layer	[nm]
d_H	thickness of the outer Helmotz layer	[nm]
D_i	diffusivity of the species i	[cm ² s ⁻¹]
E	electrode potential	[V]
\bar{E}	averaged potential on the molar fraction of the solid	[V]
E_h	hydraulic energy required by lithium recovery process	[Wh mol ⁻¹]
E_{id}	ideal potential	[V]
E_{eq}	equilibrium potential	[V]
E_{exc}	excess potential	[V]
E_{red}	potential of the reduction branch	[V]

E_t	average between the reduction and oxidation potential branches	[V]
E^0	standard potential of the reaction	[V]
E'	electrode potential contribution dependend on the state of charge	[V]
f_{CC}	fraction of carbon cloth of the electrode	-
f_l	porosity of the electrode	-
$f_{l,k}$	fraction of porosity of the pore group k	-
f_s	fraction of solid of the electrode	-
$f_{s,k}$	fraction of solid of the pore group k	-
$f_{q,k}$	fraction of flow rate of the pore group k	-
F	Faraday constant	[C mol ⁻¹]
G_{ex}	excess Gibbs free energy of the intercalation reaction	[J mol ⁻¹]
H_{ex}	excess enthalpy of the intercalation reaction	[J mol ⁻¹]
i	current density	[mA cm ⁻²]
i_0	exchange current density	[mA cm ⁻²]
I	current	[mA]
I_l	diffusion limiting current	[mA]
I_k	circulating current in the pore group k	[mA]
I_{tot}	total current of the electrode	[mA]
J_i	flux of the species i	[mol s ⁻¹ cm ⁻²]
k_0	rate constant of the reaction	[m s ⁻¹]
K_{Li}	purity coefficient of lithium in solution	-
K_s	conductivity of the solution	[mS cm ⁻¹]
K_Γ	permeability of the porous electrode	[cm ²]
L_e	thickness of the electrode	[μ m]
L_p	pore length	[μ m]
M_f	molar flow rate	[μ mol s ⁻¹]
M_p	solid fraction filled by the cations	-
M_s	saturation molar flow rate	[μ mol s ⁻¹]
n	number of electrons involved in the reaction	-
N_j	lithium moles transferred during the cycle j	-
N_k	number of pores for the pore group k	-
N_{tot}	lithium moles transferred during the process	-
Q	circulating charge	[mAh]
Q_f	maximum reduction charge	[mAh]

Q_{max}	ideal maximum charge of the electrode	[mAh]
Q_r	reference charge of the electrode measured in “simil-Atacama” solution	[mAh]
r_i	intercalation reaction rate of the cation species i	[mol m ⁻³ s ⁻¹]
R	constant of gas	[J mol ⁻¹ K ⁻¹]
Re	Reynolds number	-
R_e	radius of the electrode	[μ m]
R_h	hydraulic resistance of electrode	[mbar min ml ⁻¹]
R_l	resistance of the solution	[Ohm]
$R_{p,k}$	pore radius of the pore group k	[μ m]
S	scan rate of the cyclic voltammetry	[mV s ⁻¹]
t	time	[s]
T	absolute temperature	[K]
V	volume of the solution	[ml]
V_e	electrode volume	[μ l]
v_m	mean velocity of the electrolyte in the pore	[mm s ⁻¹]
V_{mix}	volume of the stirred tank	[ml]
V_p	pore volume	[μ l]
v_p	velocity of the electrolyte in the pore	[mm s ⁻¹]
V_r	volume of solution retained in the cell	[μ l]
V_s	volume of solid on the electrode	[μ l]
V_1	volume of the source solution	[ml]
V_3	volume of the recovery solution	[ml]
w_{ij}	interaction term in the lattice between i and j species	[J mol ⁻¹]
W_k	kinetic energy required by lithium recovery process	[Wh mol ⁻¹]
W_{th}	thermodynamic energy required by lithium recovery process	[Wh mol ⁻¹]
W_{tot}	electric energy required by lithium recovery process	[Wh mol ⁻¹]
x_i	molar fraction of the cation species i in the solid	-
z_i	valence of the ion	-
α	barrier coefficient of the electrochemical reaction	-
γ_i	activity coefficient of the species i	-
Γ	volumetric flow rate	[ml min ⁻¹]
Γ_k	volumetric flow rate of the pore group k	[ml min ⁻¹]
Γ_s	saturation volumetric flow rate	[ml min ⁻¹]
δ	Nernst diffusion layer	[μ m]
ΔG	Gibbs free energy of an intercalation reaction	[J mol ⁻¹]
ΔG_{id}	ideal Gibbs free energy of an intercalation reaction	[J mol ⁻¹]

ΔG_m	mixing Gibbs free energy of an intercalation reaction	[J mol ⁻¹]
ΔG^0	standard Gibbs free energy of an intercalation reaction	[J mol ⁻¹]
ΔH_m	mixing enthalpy of an intercalation reaction	[J mol ⁻¹]
ΔP	pressure drop on the electrode	[mbar]
ΔS_m	mixing entropy of an intercalation reaction	[J mol ⁻¹]
ΔV	potential difference of the cell	[V]
$\Delta\phi_H$	Galvani potential difference at the solid and liquid interface	[V]
$\Delta\phi_H^0$	Standard potential difference	[V]
ϵ_r	relative permittivity of a medium	-
ϵ_0	dielectric constant of the vacuum	[F m ⁻¹]
$\bar{\eta}$	mean overpotential of the capturing reaction	[V]
η_A	overpotential of the oxidation semi-reaction	[V]
η_c	Coulombic efficiency of the intercalation reaction	-
η_{ct}	overpotential due to the charge transport at the interface	[V]
η_C	overpotential of the reduction semi-reaction	[V]
η_{mt}	overpotential due to the mass transport	[V]
η_r	Coulombic efficiency of the deintercalation reaction	-
η_Ω	overpotential due to the ohmic drops	[V]
μ	viscosity of the solution	[cP]
μ_i	chemical potential of the species i	[J mol ⁻¹]
μ_e^α	chemical potential of the electron in the phase α	[J mol ⁻¹]
$\tilde{\mu}_i$	electrochemical potential of the species i	[J mol ⁻¹]
ρ	density of the solution	[g dm ⁻³]
ϕ_k	Galvani potential of the liquid of the pore group k	[V]
ϕ_s	Galvani potential of the solid	[V]

Publications

1. *Influence of Hydrodynamics on the Lithium Recovery Efficiency in an Electrochemical Ion Pumping Separation Process.* Palagonia M.S., Brogioli D., La Mantia F. J. *Electrochem. Soc.* 164(14):E586-E595, 2017. doi: 10.1149/2.1531714jes.
2. *Intercalation into a Prussian Blue Derivative from Solutions Containing Two Species of Cations.* Erinwmingbovo C., Palagonia M.S. Brogioli D., La Mantia F. *ChemPhysChem* 18(8), 2017. doi: 10.1002/cphc.201700020
3. *Impedance Spectroscopy Analysis of the Lithium Ion Transport through the $Li_7La_3Zr_2O_{12}/P(EO)_{20}Li$ Interface.* Langer F., Palagonia M.S., Bardenhagen I., Glenneberg J., La Mantia F., Kun R. J. *Electrochem. Soc.* 2017 164(12):A2298-A2303. doi: 10.1149/2.0381712jes.
4. *Behavior of Alloying Elements during Anodizing of Mg-Cu and Mg-W Alloys in a Fluoride/Glycerol Electrolyte.* Palagonia M.S., A. Němcová, I. Kuběna, M. Šmíd, S. Gao, H. Liu, X. L. Zhong, S. J. Haigh, M. Santamaria, F. Di Quarto, H. Habazaki, P. Skeldon, and G. E. Thompson. *J. Electrochem. Soc.* 162(9):C487-C494, 2015. doi: 10.1149/2.0761509jes